AD NUMBER
AD525863
CLASSIFICATION CHANGES
TO: **UNCLASSIFIED**
FROM: **SECRET**
LIMITATION CHANGES
TO: **Approved for public release; distribution is unlimited.**
FROM: **Distribution authorized to U.S. Gov't. agencies and their contractors; Administrative/Operational Use; NOV 1972. Other requests shall be referred to Rome Air Development Center, Griffiss AFB, NY 13441-5700.**
AUTHORITY
RADC ltr dtd 16 Jul 1974; RADC ltr dtd 16 Jul 1974

SECURITY MARKING

The classified or limited status of this report applies to each page, unless otherwise marked.
Separate page printouts MUST be marked accordingly.

THIS DOCUMENT CONTAINS INFORMATION AFFECTING THE NATIONAL DEFENSE OF THE UNITED STATES WITHIN THE MEANING OF THE ESPIONAGE LAWS, TITLE 18, U.S.C., SECTIONS 793 AND 794. THE TRANSMISSION OR THE REVELATION OF ITS CONTENTS IN ANY MANNER TO AN UNAUTHORIZED PERSON IS PROHIBITED BY LAW.

NOTICE: When government or other drawings, specifications or other data are used for any purpose other than in connection with a definitely related government procurement operation, the U. S. Government thereby incurs no responsibility, nor any obligation whatsoever; and the fact that the Government may have formulated, furnished, or in any way supplied the said drawings, specifications, or other data is not to be regarded by implication or otherwise as in any manner licensing the holder or any other person or corporation, or conveying any rights or permission to manufacture, use or sell any patented invention that may in any way be related thereto.

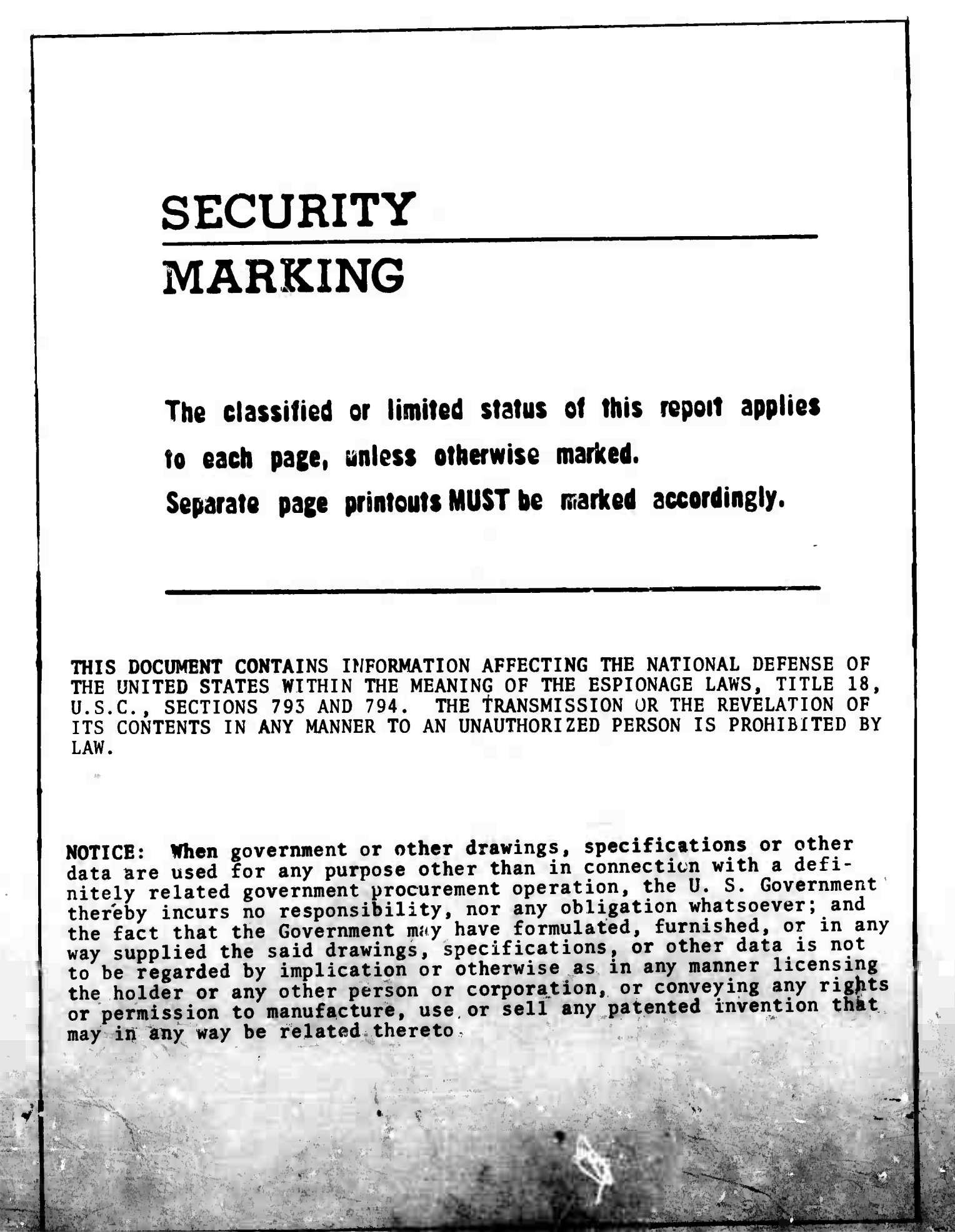

RADC-TR-73-94
Technical Report
November 1972

EXPERIMENTS AND MODELS FOR PRAIRIE SMOKE (U)

Aeronomy Corporation

Sponsored by
Defense Advanced Research Projects Agency
ARPA Order No. 1423

The views and conclusions contained in this document are those of the authors and should not be interpreted as necessarily representing the official policies, either expressed or implied, of the Defense Advanced Research Projects Agency or the U. S. Government.

Rome Air Development Center
Air Force Systems Command
Griffiss Air Force Base, New York

Do not return this copy. When not needed, destroy in accordance with pertinent security regulations.

EXPERIMENTS AND MODELS FOR PRAIRIE SMOKE (U)

S. A. Bowhill
E. E. Mendenhall

Contractor: Aeronomy Corporation
Contract Number: F30602-72-C-0214
Effective Date of Contract: 1 September 1971
Contract Expiration Date: 1 October 1973
Amount of Contract: $216,000.00
Program Code Number: 1E20

Principal Investigator: Dr. S. A. Bowhill
Phone: 217 359-8007

Project Engineer: Vincent J. Coyne
Phone: 315 330-3141

Contract Engineer: Richard W. Carman
Phone: 315 330-3144

This research was supported by the Defense Advanced Research Projects Agency of the Department of Defense and was monitored by Richard W. Carman RADC (OCSE), GAFB, NY 13441 under Contract F30602-72-C-0214.

PUBLICATION REVIEW

This technical report has been reviewed and is approved.

RADC Project Engineer

RADC Contract Engineer

ABSTRACT (U)

This report describes satellite transmission experiments carried out in Prairie Smoke Ib and II to investigate the horizontal extent, altitude distribution, intensity and frequency dependence of field-aligned artificial spread F (ASF) irregularities. Using these data, a quantitative morphological model is described in which the irregularities are contained within a tilted cylinder, with axis parallel to the magnetic field direction, and a radius of 50 km, centered 30 km north of the heater at an altitude of 300 km. The fractional fluctuation of electron density was found to be about 0.7 percent at full power, and the correlation distance normal to the field was about 100 m. The irregularities were found to extend through the entire F region between 200 and 400 km altitude. The depth was found to vary inversely with frequency, in accordance with theory. Also presented in this report is a model for the small-scale structure, including an analytic technique to determine the thickness of the disturbed region from the change in echo return range with elevation of a monostatic radar; semi-thicknesses of about 25 km are found.

TABLE OF CONTENTS (U)

1. INTRODUCTION (U)

(S) Initial experiments on satellite signals transmitted through a disturbed ionospheric region over the heater at Platteville, Colorado, were described in a previous report (Bowhill and Mendenhall, 1972). The present report describes the continued program of measurements and interpretation, primarily in Prairie Smoke Ib (February 1972) and II (May 1972). These results are presented and discussed in Sections 2 through 6.

(S) During the summer of 1972, a scattering model for the artificial spread F (ASF) irregularities was developed, and is presented in Sections 7 and 11. In addition, a simple model for on-frequency scatter (OFS) has been developed and is presented and evaluated in Sections 8 through 10.

(S) In preparation for possible applications studies, some considerations for bistatic OFS modeling are given in Section 12.

2. OBJECTIVES OF PRAIRIE SMOKE Ib AND II (U)

(S) Two types of satellite transmission experiments have been carried out by Aeronomy Corporation in connection with the Prairie Smoke activities; a geostationary satellite and an orbital satellite experiment. The two experiments provide a means for determining a morphological model (and hence, a radar scattering model) and for ultimately determining a yield model of artificial spread-F (ASF) irregularities and on-frequency scatter (OFS) produced by the ionospheric heating.

(S) A detailed list of objectives for the satellite experiments was presented by Bowhill and Mendenhall (1972). Table 2.1 illustrates the applicability of the results of experiments conducted during Prairie Smoke Ib and II for satisfying these objectives. Sections 2.1 and 2.2 describe the specific objectives of Prairie Smoke Ib and II experiments.

2.1 Objectives of Prairie Smoke Ib (U)

(S) Due to the relatively short time available to mount a field experiment for Prairie Smoke I, attention was concentrated on implementing a mobile geostationary satellite receiving station. An orbital experiment was conducted on December 6, 1971 when a single pass was recorded from a fixed site in Pine Bluffs, Wyoming. Prairie Smoke Ib, which was scheduled for February 14-17, 1972, however, offered the first opportunity to deploy a mobile facility for recording appropriate orbital passes. Because of the remoteness of the site location for the geostationary experiment and the potentially inclement weather, attention was concentrated on the orbital experiment.

(S) The purposes for going into the field at this time were to test hard-

Table 2.1

Potential (P) or demonstrated (D) applicability of the satellite transmission experiment to the various objectives using amplitude measurements from 1-3 antennas, or an interoferometric pair (I).

Objective	Geostationary				Orbital			
	1	2	3	I	1	2	3	I
1. Field alignment			D				D	
2. Size and orientation			D			D	D	
3. Altitude distribution						D	D	
4. Horizontal extent	D				D			
5. Onset and decay	D	D	D					
6. Drift velocity		D	D					
7. Fading with frequency	P				D			
8. Angle flutter with frequency			P					
9. Multipath effects	P				D			
10. Off-frequency scatter	P				P			
11. Modulation degradation	P				P			
12. Heater parameters	P				P			
13. Off-vertical heating	P				P			
14. New antenna concepts	P				P			

ware planned for future orbital experiments, to demonstrate the usefulness of orbital measurements in satisfying the objectives listed in Table 2.1, and to determine the consistency of orbital measurements with the geostationary data taken in Prairie Smoke 1 (and therefore determine if changes should be made in the configuration used for future geostationary experiments).

2.2 Objectives of Prairie Smoke II (U)

(S) Prairie Smoke II represented the first opportunity to mount both experiments (geostationary and orbital) simultaneously. The objectives of the Prairie Smoke II test series were primarily to obtain sufficient quality and quantity of measurements for confirming Prairie Smoke I and Ib results, to provide additional information concerning the horizontal extent and altitude distribution of the ASF irregularities, and to demonstrate the fading dependence on frequency by taking data at 400 MHz during the orbital experiment. The major improvement in data quality planned for Prairie Smoke II includes the capability of real-time digital data-logging for the geostationary experiment and the capability of A/D conversion of the orbital data, as well as data collected during Prairie Smoke I and Ib.

3. EXPERIMENTAL CONFIGURATIONS (U)

(S) During Prairie Smoke Ib on February 14-17, 1972, observations were made of the scintillations of signals radiated from US Navy navigational satellites transmitted at about 150 MHz and moving in a nearly polar orbit. Since the periods of observation of these satellites was limited by observational considerations, it was not possible to use a single receiving site for all four days. It was then assumed that the greatest intensity of fluctuations would be found when the satellite LOS passes through a point at 300-km altitude directly over Platteville. For the passes nearest to overhead, the satellite LOS was traced through the 300-km point to the surface of the earth. During the satellite pass, the intersection with the earth sweeps in a general N-S direction. The points for each day at which it intersects Interstate Route 80 were determined, and established as the observation point for each day. A map showing these site locations with respect to the transmitter near Platteville is provided in Figure 3.1. Subsequent analysis of the satellite passes for each location (Table 3.1) showed that the LOS passes over Platteville at altitudes of 284 to 316 km, in good agreement with the predictions. The availability of spaced antenna data for each pass is provided in Table 3.2.

(S) Since the highly mobile receiving station for the orbital experiment (subsequently used for Prairie Smoke II) was not yet available at the time of Prairie Smoke Ib, a station was equipped by rack-mounting the receivers and chart recorder used in the geostationary experiment of Prairie Smoke I in a utility van. Additional equipment included a Sony Type 366-4 4-channel tape deck for recording the product detector BFO output of the receivers. Dual circularly-polarized turnstile antennas and battery-operated Vanguard dual-

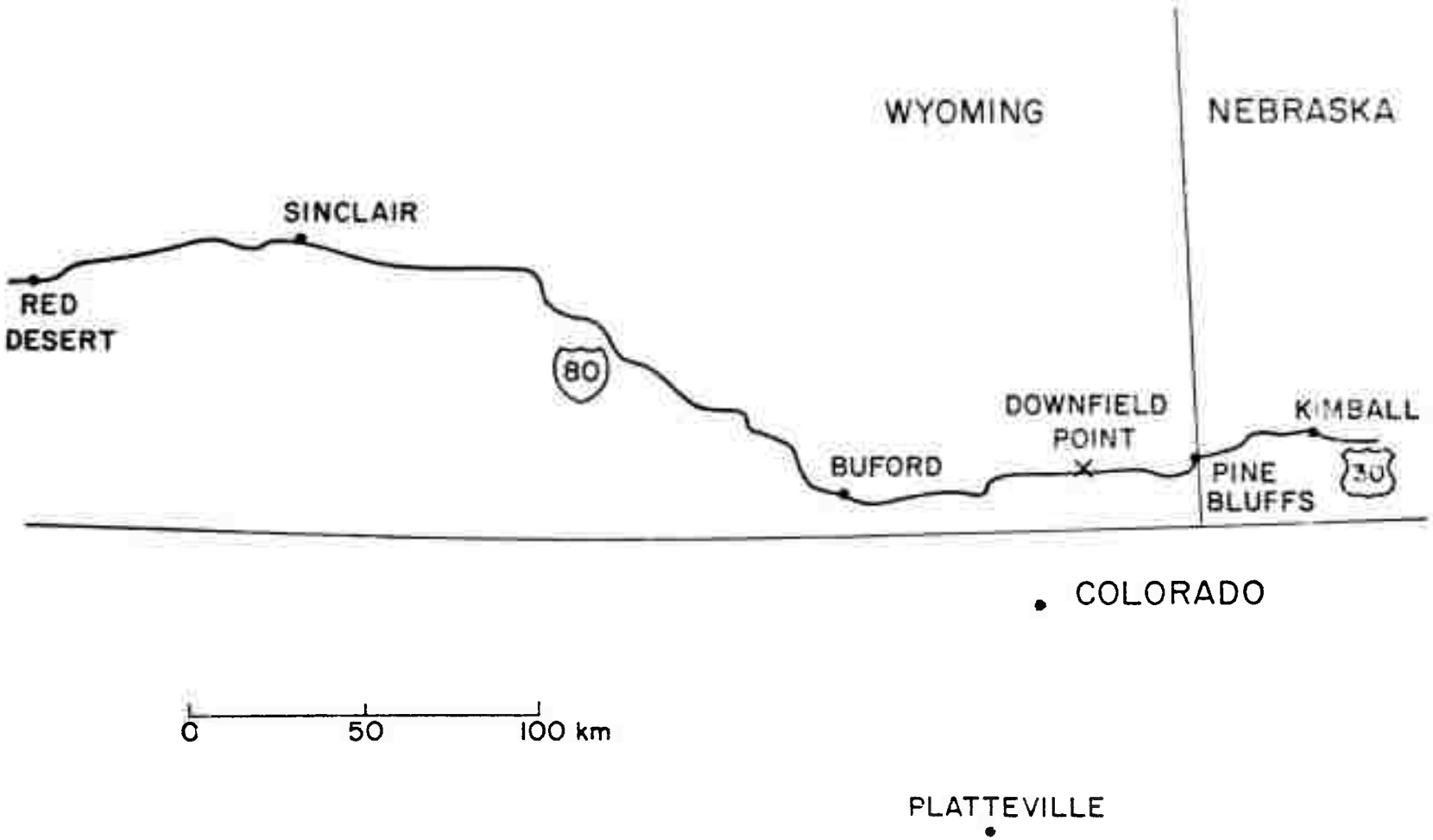

Figure 3.1

Map showing site locations chosen for Prairie Smoke Ib. (U)

Table 3.1

LOS over transmitter for orbital passes during Prairie Smoke Ib (U)

SITE	RANGE TO TRANSMITTER km	LOS OVER TRANSMITTER		
		AZIMUTH	ELEVATION	HEIGHT
KIMBALL, NEB.	151.3	219.0	60.8	284.0
BUFORD, WYO.	109.4	158.2	70.0	316.1
SINCLAIR, WYO.	265.5	130.8	46.9	302.8
RED DESERT, WYO.	318.7	119.5	40.2	289.9

SECRET

Table 3.2

Availability of data for orbital passes during Prairie Smoke Ib (U)

DATE 1972	RRI OBSERVATION MST	OBSERVATION LOCATION	LOS OVER TRANSMITTER TIME MST	RANGE km	NUMBER OF ANTENNAS
14 FEB.	0830-1300	SINCLAIR, WYO.	1337:00	1360	2
15 FEB.	1500-1942	KIMBALL, NEB.	1449:57	1215	2
16 FEB.	1500-1947	BUFORD, WYO.	1901:40	1185	3
17 FEB.	1500-2000	RED DESERT, WYO.	1745:50	1365	2

gate MOSFET RF converters were used for receiving the signals from the orbiting satellites. Data was subsequently analyzed by playing the signals back through a Hewlett-Packard 310A wave analyzer, acting as a tracking filter with a 200-Hz bandwidth, and recorded on a thermal-writing recorder.

(S) During Prairie Smoke II on April 24 - May 12, 1972, both a geostationary and orbital experiment were conducted. The geostationary mobile station was deployed near Lance Creek, Wyo., the more southerly site location used during Prairie Smoke I. Since this facility required at least one full day for changing site locations, a single site was used for each day even though the height of reflection of the heater changed during the experiment.

(S) The same equipment was used for the geostationary experiment as was used during Prairie Smoke I. Additionally, the product detector BFO output of the receivers, including one monitoring WWV, was continuously recorded with a 4-channel tape deck. Simultaneously, the receiver detector output was recorded on a Metrodata model 616 digital data-logging system sampling at 2-$^{1}/_{2}$ samples per second on each of three channels. Use of a Metrodata 622 S digital tape reader interfaced with a PDP-8e digital computer offers the potential of compact storage and prompt analysis of large quantities of data. Development of the software to implement this digital data-recovery system is nearly complete. Real-time records were also obtained by recording the detector output on a dual-channel chart recorder. The availability of the geostationary records is given in Table 3.3.

(S) The mobile orbital satellite receiving station for Prairie Smoke II consisted of a 23-ft Winnebago vehicle shell with a 5-kW gasoline generator as a power supply, providing a mobile facility capable of traveling between widely separated site locations. The data was recorded on magnetic tape in the manner described for Prairie Smoke Ib. An A/D converter with an 8-channel

Table 3.3

Availability of geostationary data during Prairie Smoke II (U)

GEOSTATIONARY DATA AVAILABLE		
DATE (1972)	TIMES OF RECORD (MST)	E-W SPACING (m) *
24 APRIL	1247 - 1705	90
25 APRIL	0559 - 1200	90
04 MAY	0859 - 1945, 2015 - 2206	90
05 MAY	1055 - 1701	90
08 MAY	0800 - 1149 **	90
09 MAY	0554 - 1118, 1130 - 1501	90
10 MAY	1620 - 2202	90
11 MAY	1552 - 2200	122
12 MAY	1102 - 1511	122

* N-S SPACING ALWAYS 305 m

** TRANSMITTER OFF

multiplexer is presently available for use with the PDP-8e computer to perform more rapid data reduction from the tape recordings using Fourier and correlation techniques than is possible by visual reduction of chart recordings. (S) Site locations for the orbital experiment were chosen so that the LOS passed near the 300-km point over the transmitter within the constraints of time to change site locations, transmitter schedules for the Platteville facility, and difficulty in crossing the continental divide in the months of April and May. It was also desired to record as many passes as possible (even the more oblique passes), in order to place limits on the size of the volume comprising the modified region by detecting the reduced effect at the edge of the region. The site locations for the passes recorded during Prairie Smoke II are given in Table 3.4. The distance of closest approach of the LOS of these passes from the 300-km point over Platteville is presented in Table 3.5. A map showing the location of these sites with respect to the transmitter near Platteville is provided in Figure 3.2. The availability of spaced-antenna data for the orbital passes is presented in Table 3.6.

Table 3.4

Site locations for orbital experiment during Prairie Smoke II (U)

DATE (1972)	TIME (MST)	SITE LOCATION AND COORDINATES
24 APRIL	1336	ESTES PARK, COLO. (40.38°N, 105.52°W)
24 APRIL	1409	
25 APRIL	0856	
04 MAY	0930	BRUSH, COLO. (40.19° N, 103.38° W)
04 MAY	1606	
05 MAY	1336	WIGGENS, COLO. (40.09° N, 104.07° W)
08 MAY	1300	
09 MAY	0832*	HILLSDALE, WYO. (41.17°N, 104.47°W)
09 MAY	0900	
10 MAY	2032	KIMBALL, NEB. (41.23° N, 103.72° W)
10 MAY	2110	
11 MAY	2021	ESTES PARK, COLO. (40.38°N, 105.52°W)
12 MAY	1257	
12 MAY	1454*	

*TRANSMITTER OFF

Table 3.5

LOS for orbital passes during Prairie Smoke II (U)

ORBITAL DATA AVAILABLE

DATE (1972)	PASS TIME (MST)	DISTANCE OF LOS FROM TRANSMITTER AT 300 km HEIGHT (km)		HEIGHT OF LOS OVER TRANSMITTER (km)
24 APRIL	1336	15	E	251
24 APRIL	1409	11	E	255
25 APRIL	0856	124	E	87
04 MAY	0930	1	E	302
04 MAY	1606	94	W	159
05 MAY	1336	7	W	267
08 MAY	1300 *	12	W	242
09 MAY	0832	12	W	200
09 MAY	0900	4	E	356
10 MAY	2032	13	W	250
10 MAY	2110	86	W	124
11 MAY	2021	112	E	104
12 MAY	1257	20	W	440
12 MAY	1454 *	66	E	145

* TRANSMITTER OFF

SECRET

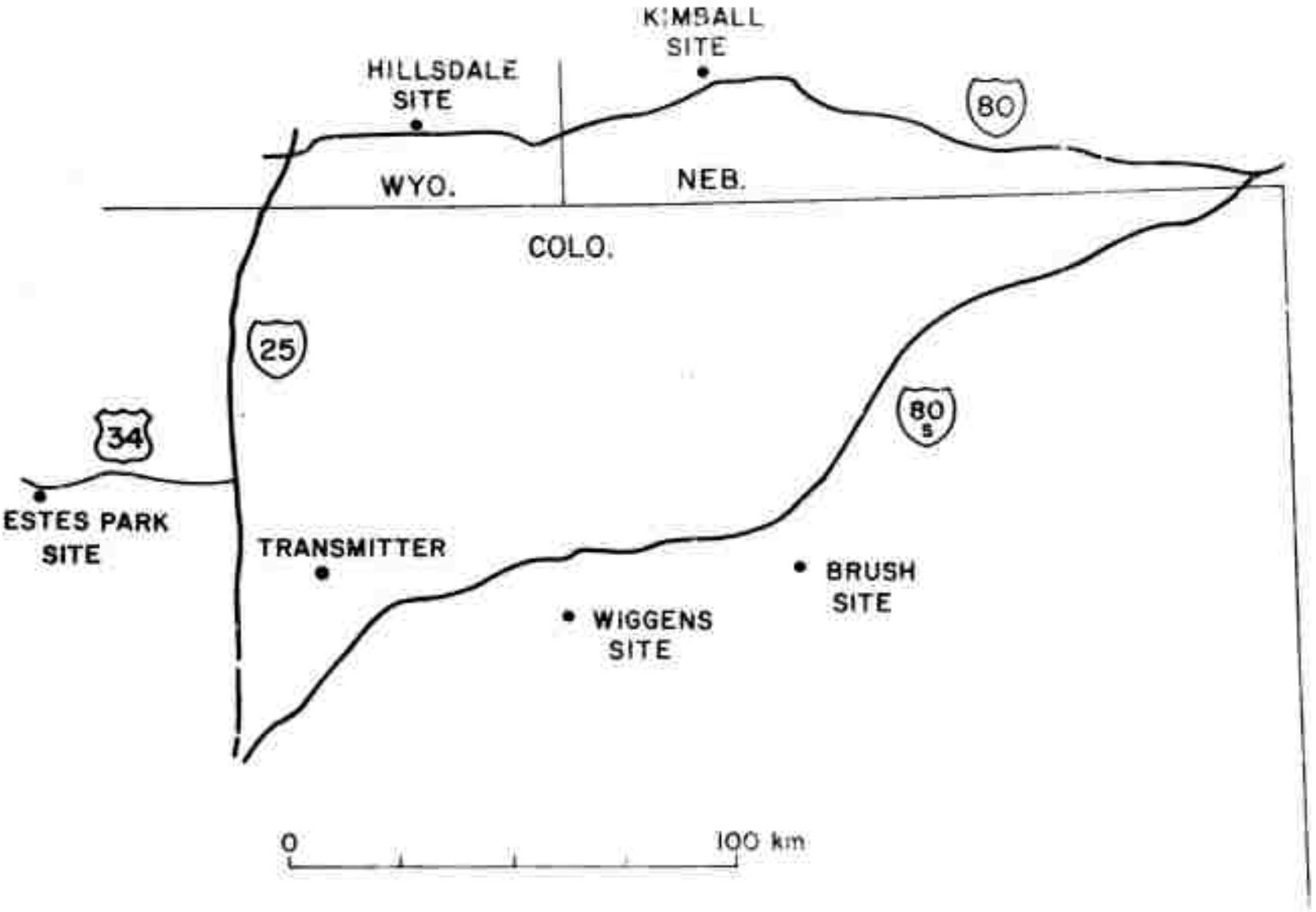

Figure 3.2

Map showing site locations for orbital experiment during Prairie Smoke II. (U)

SECRET

Table 3.6

Availability of orbital data during Prairie Smoke II (U)

DATE (1972)	OBSERVATION LOCATION	NUMBER OF ANTENNAS 150 MHz	400 MHz
24 APRIL	ESTES PARK, COLO.	4	1
25 APRIL		4	1
04 MAY	BRUSH, COLO.	4	1
05 MAY	WIGGENS, COLO.	4	1
08 MAY*		3	0
09 MAY	HILLSDALE, WYO.	3	1
10 MAY	KIMBALL, NEB.	2	2
11 MAY	ESTES PARK, COLO.	3	2
12 MAY		3	2

*TRANSMITTER OFF

4. RESULTS OF PRAIRIE SMOKE Ib (U)

(S) The satellites of the US Navy Satellite Navigation System are all in approximately circular polar orbits at heights of about 1025 km above the earth's surface. Since their times of passage are distributed (though somewhat irregularly) throughout the day, they are particularly suitable for transmission studies of specific regions of the ionosphere such as that over Platteville. Unfortunately, only one or two a day pass sufficiently nearly overhead Platteville to permit their use as a consistent diagnostic for a given site location, and these may not be at suitable times on a given day. However, between February 14-17, 1972 the four passes described in Tables 3.1 and 3.2 were recorded.

(S) Figures 4.1 and 4.2 show spaced receiver signals recorded during a portion of two of these passes. Subsequent to Prairie Smoke Ib it has become possible to play the tape recordings back through the wave analyzer and an A/D converter interfaced with a PDP-8e computer as described in Section 2 to provide values of the scintillation index over 4-second intervals. The expression for the scintillation index (S) is given by

$$S^2 = \left(\frac{1}{N} \sum_{1}^{N} A_n^2 \right) - \left(\frac{1}{N} \sum_{1}^{N} A_n \right)^2 \Big/ \left(\frac{1}{N} \sum_{1}^{N} A_n \right)^2 \qquad (4.1)$$

where A_n is the received signal amplitude for the n^{th} sample and N is the total number of samples taken over the given time interval. The results of that analysis is presented for the Kimball and Buford passes in Figures 4.3 and 4.4. These two passes are analyzed in detail here since they represent

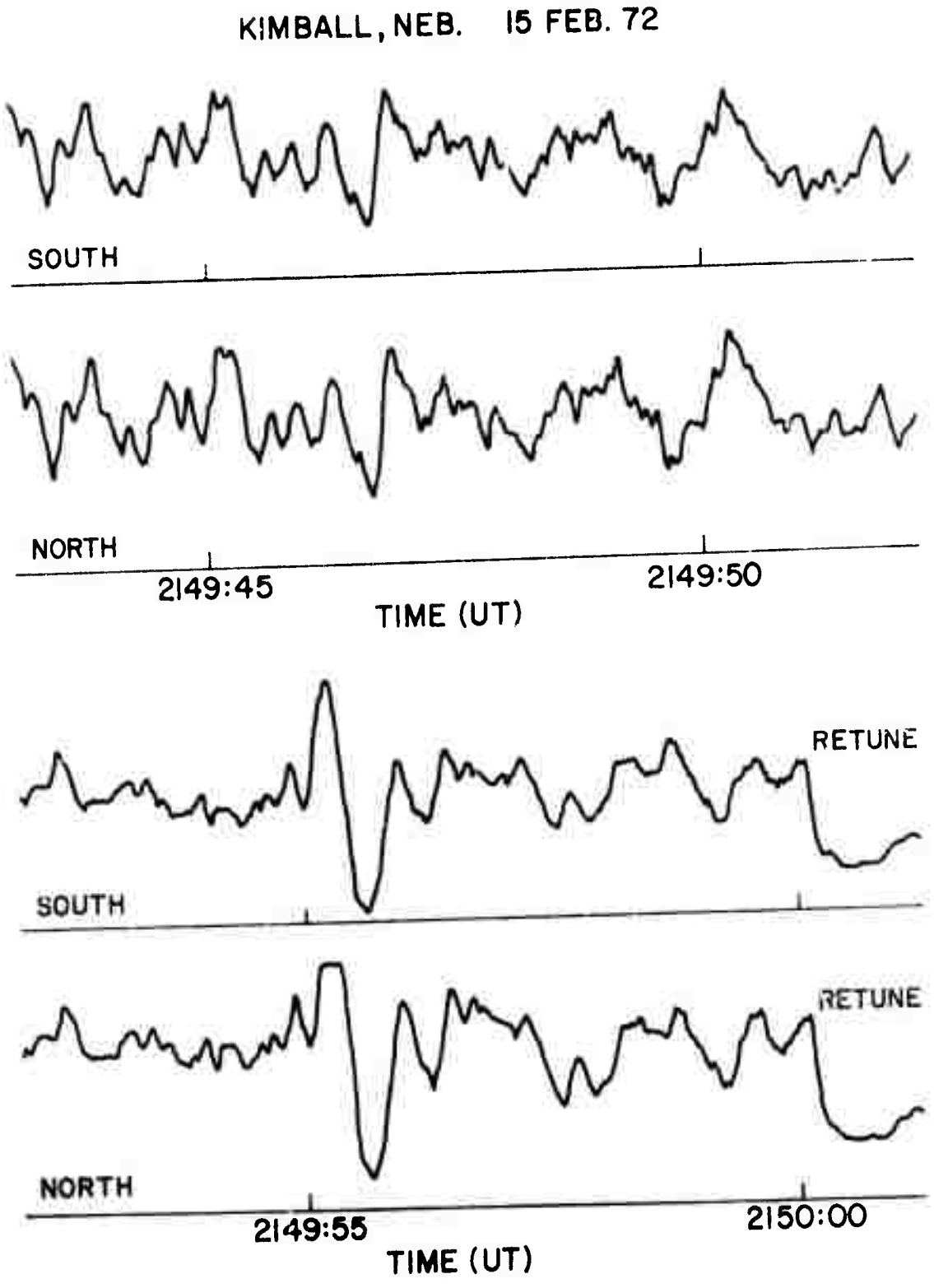

Figure 4.1

Chart records showing sample of orbital data (U)

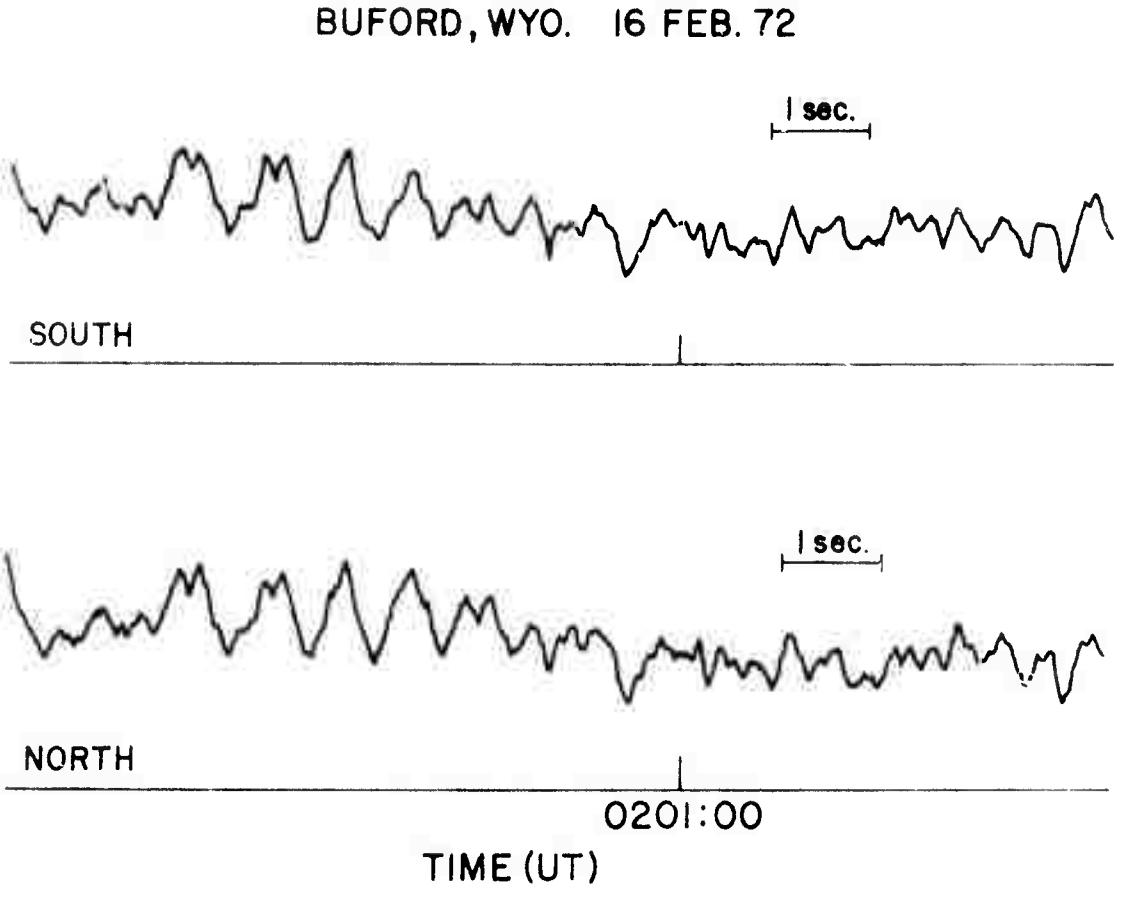

Figure 4.2

Chart records showing sample of orbital data (U)

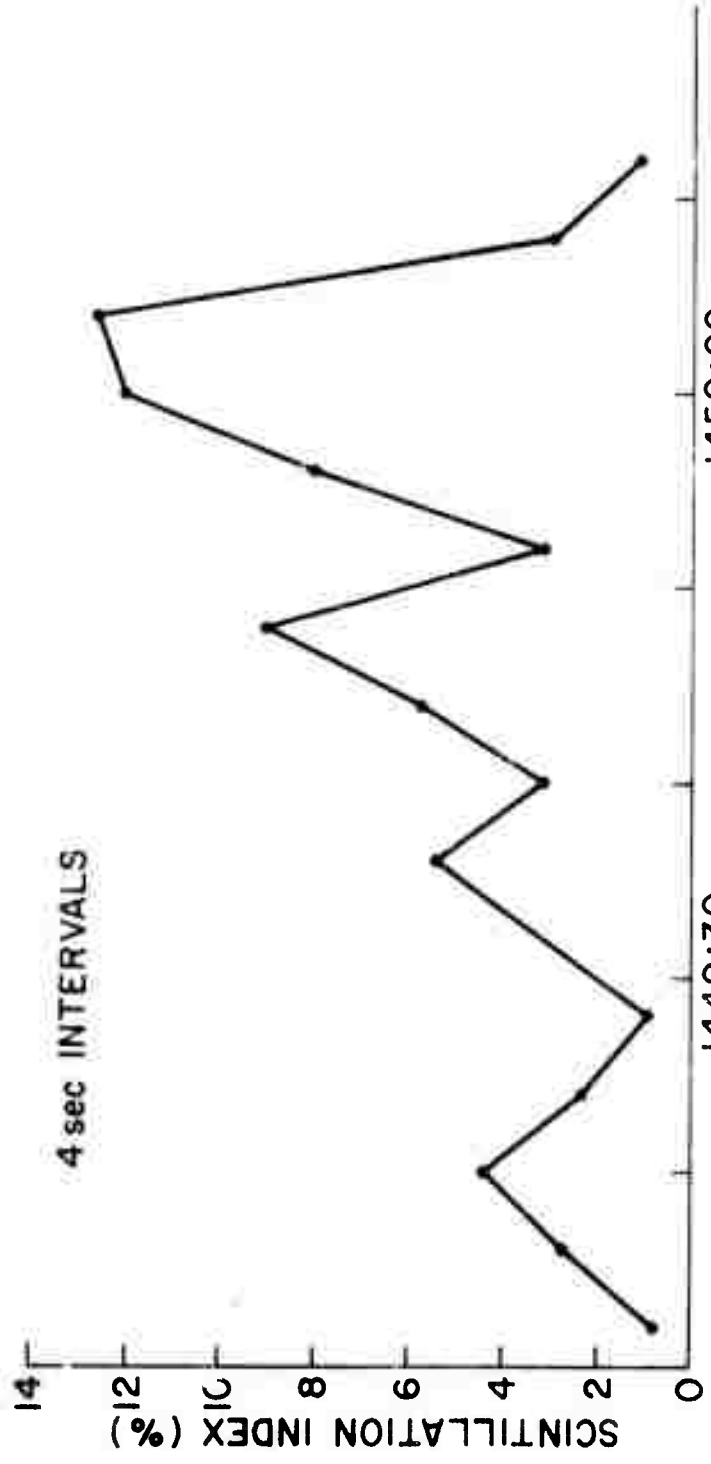

Figure 4.3
Fading intensity for an orbital pass. (U)

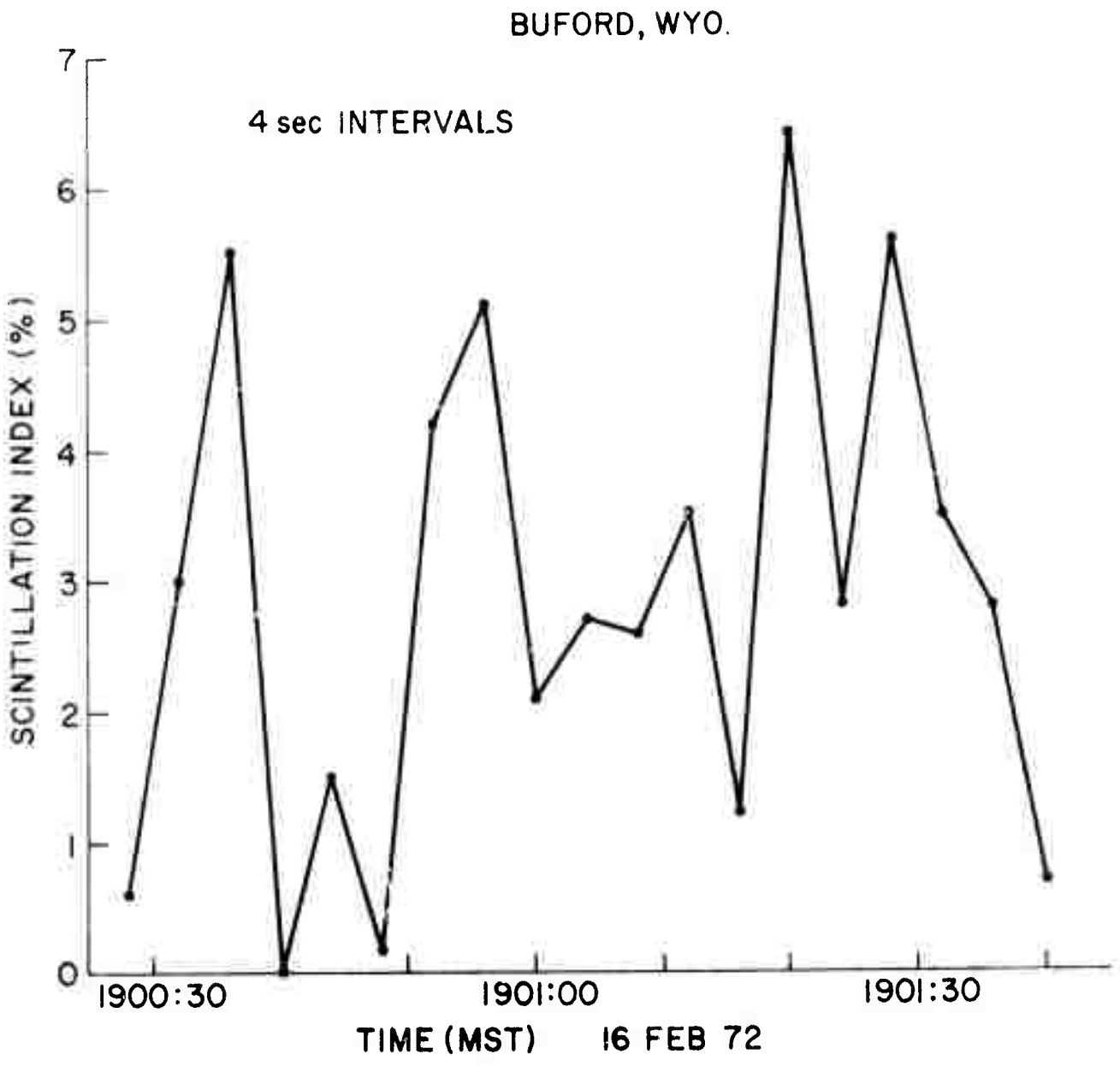

Figure 4.4

Fading intensity for an orbital pass (U)

the two passes when the deepest fading was observed and the LOS was nearest to being parallel to the magnetic field. The scintillation indices for each of the four passes when the deepest fading was observed are presented in Table 4.1 with an estimate of the angle between the LOS and magnetic field. The chart recordings at these times are shown in Figure 4.5. The transmitter mode during each pass is provided in Table 4.2. It is planned to perform a complete correlation analysis on these data to provide size, orientation, and height distribution of the ASF irregularities. However, for the antenna spacings used (76 m at Buford and 122 m at Kimball) along a N-S baseline the time shift for maximum cross correlation can be measured by comparing chart recordings run at faster speeds than those presented in the following figures. This procedure was used for determining the height of the irregularities, which for a plane earth is given by

$$z_i = R \sin(\varepsilon)/(1 - \frac{V_s t}{d}) \qquad (4.2)$$

where

R = Range to satellite from observer

ε = Elevation of satellite from observer

V_s = Satellite velocity parallel to baseline

t = Time shift on N-S baseline

d = N-S antenna spacing

z_i = Height of irregularities above tangent plane.

z_i is converted to heights above the earth's surface by

$$h = (z_r + z_i)/\cos \gamma_c - z_r \qquad (4.3)$$

Table 4.1

Maximum fading observed for data taken during Prairie Smoke 1b (U)

DATE (1972)	OBSERVATION LOCATION	MAXIMUM SCINTILLATION INDEX (%)	ANGLE OF LOS TO MAGNETIC FIELD (deg)
14 FEB	SINCLAIR, WYO.	3.0	35.0
15 FEB	KIMBALL, NEB.	12.6	12.5
16 FEB	BUFORD, WYO.	6.8	11.5
17 FEB	RED DESERT, WYO.	3.5	44.5

SECRET

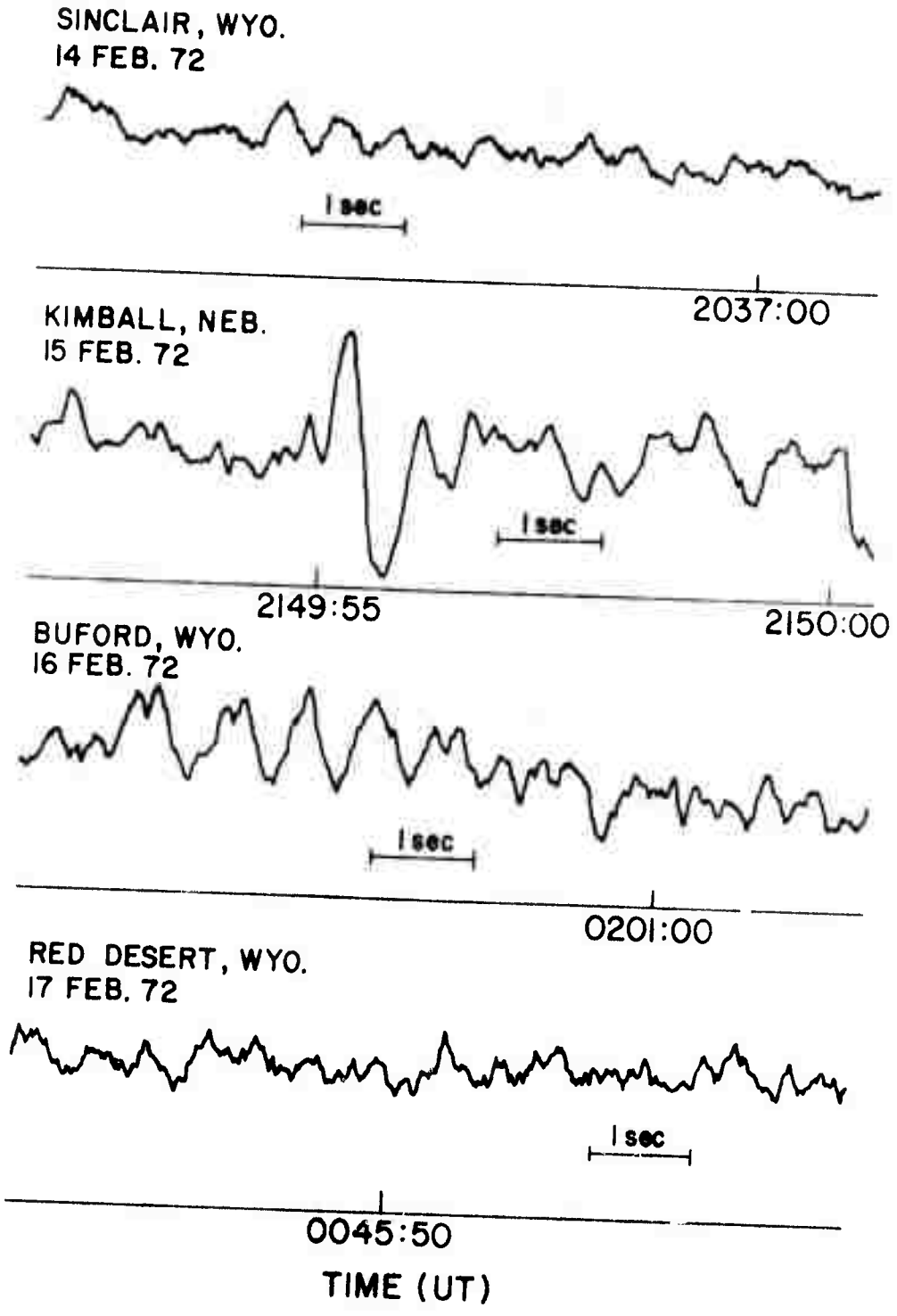

Figure 4.5

Chart records showing maximum fading observed during Prairie Smoke Ib (U)

Table 4.2

Transmitter modes during orbital passes during Prairie Smoke Ib (U)

DATE (1972)	TIME OF LOS OVER TRANSMITTER (MST)	TRANSMITTER MODE	f_0F_2/f_H
14 FEB	1337:00	OFF	<1 *
15 FEB	1449:57	CW	1.02
16 FEB	1901:40	CW	.95
17 FEB	1745:50	10 Hz SQUARE WAVE	1.03

* PRIOR TO 1337:00 MST

where

h = the geocentric height,

z_r = the radius of the earth

γ_c = the angle at the earth's center subtended by the satellite and the point of observation and where it has been assumed that the earth is spherical.

(S) When the records for the Kimball and Bufford passes were examined and the time shifts for individual fades measured, it was found that the heights calculated were distributed through a height range of approximately 100 km. For both passes a height of 225 km was most frequently measured with heights extending up to the F layer and down to somewhat less than 200 km. These height distributions are shown in Figures 4.6 and 4.7.

(S) For the Kimball pass the heights observed were subdivided into those observed in two-second intervals. Figure 4.8 shows these height ranges on the LOS from the observation site. The mean heights observed for each of these intervals are located nearly directly over the transmitter for the deepest fading observed, that part of the pass shown in Figure 4.5.

(S) The average spatial quasi-period, α, has been calculated using

$$\alpha = (1 - z_i/R \sin \varepsilon)V_s\tau \qquad (4.4)$$

where z_i, R, ε, and V_s have been previously defined and τ is the fade period at the observation site. Figure 4.9 shows the frequency distribution of the quasi-periods measured at Kimball. For a Gaussian auto-correlation function (ρ) of the form

$$\rho(x) = e^{-x^2/d^2} \qquad (4.5)$$

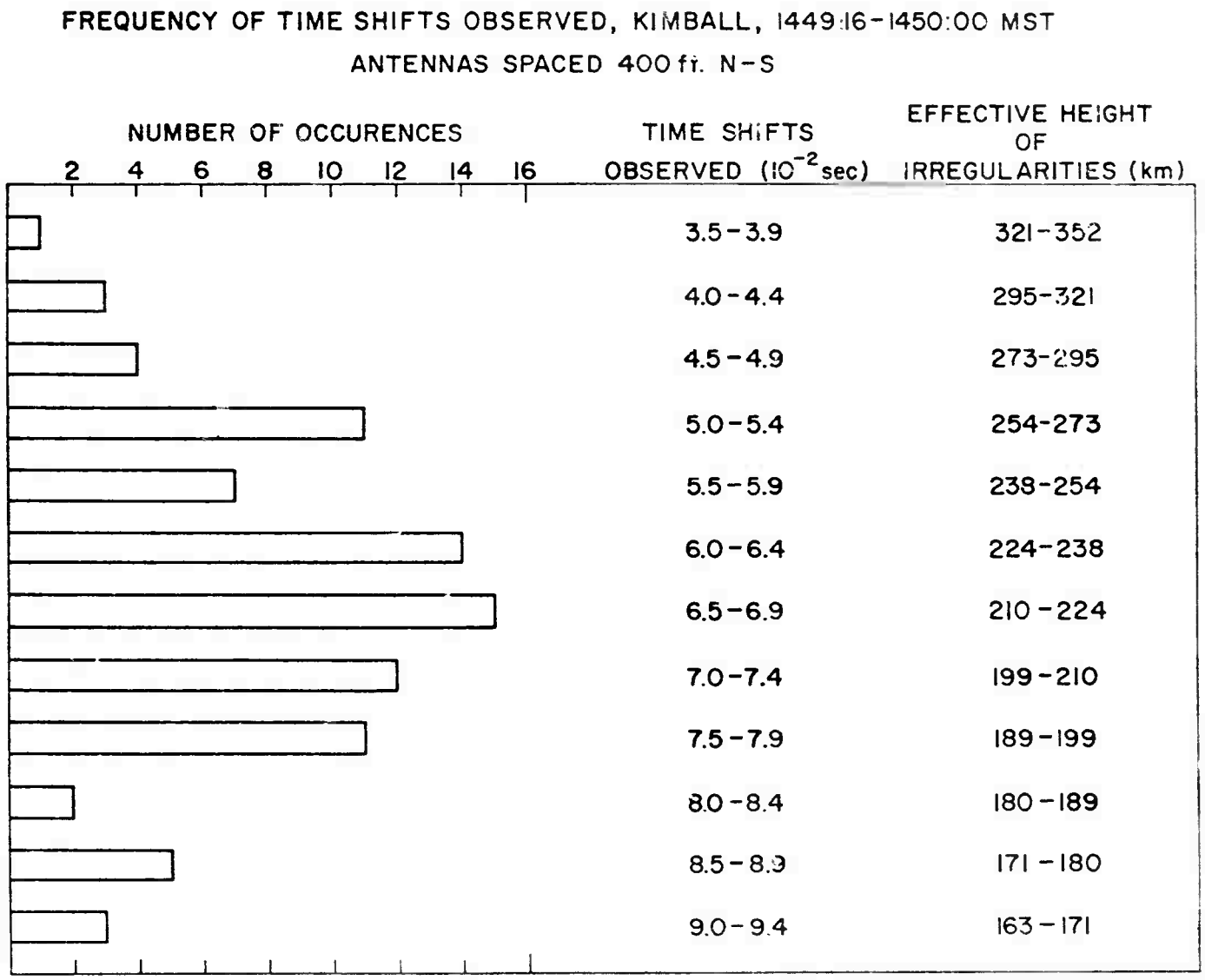

Figure 4.6

Frequency distribution of h for an orbital pass (U)

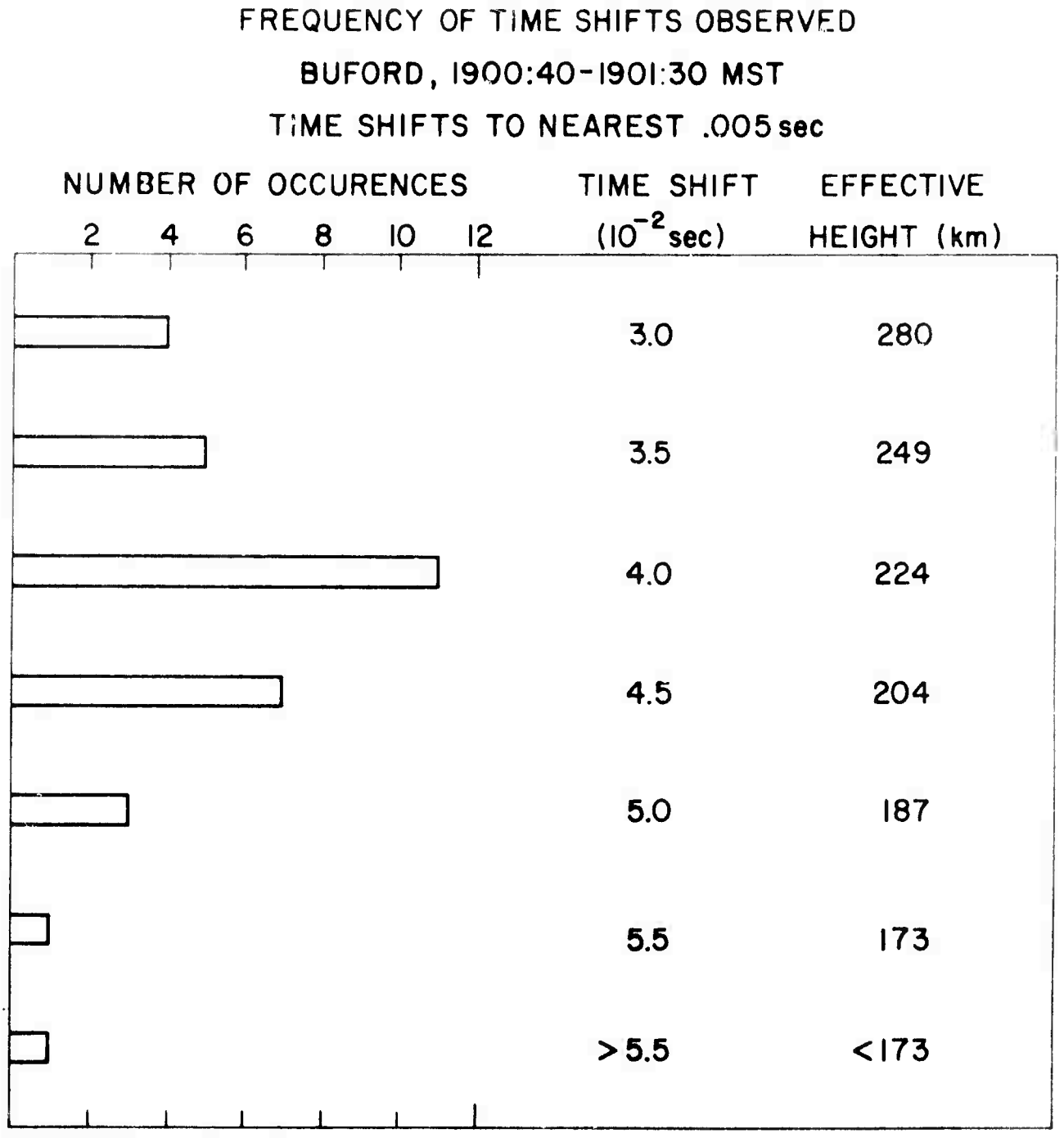

Figure 4.7
Frequency distribution of h for an orbital pass (U)

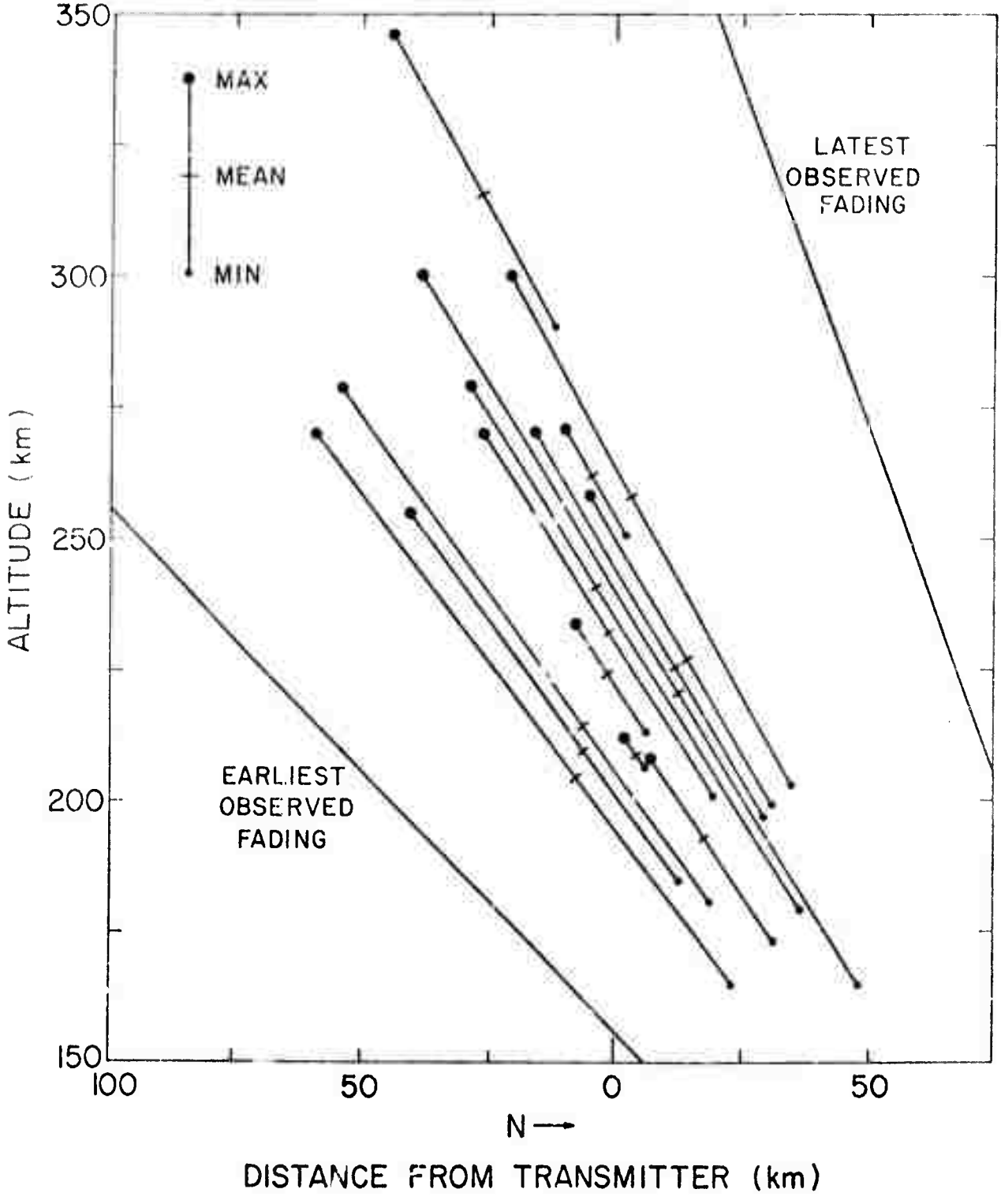

Figure 4.8

Distribution of h shown on LOS of an orbital pass (U)

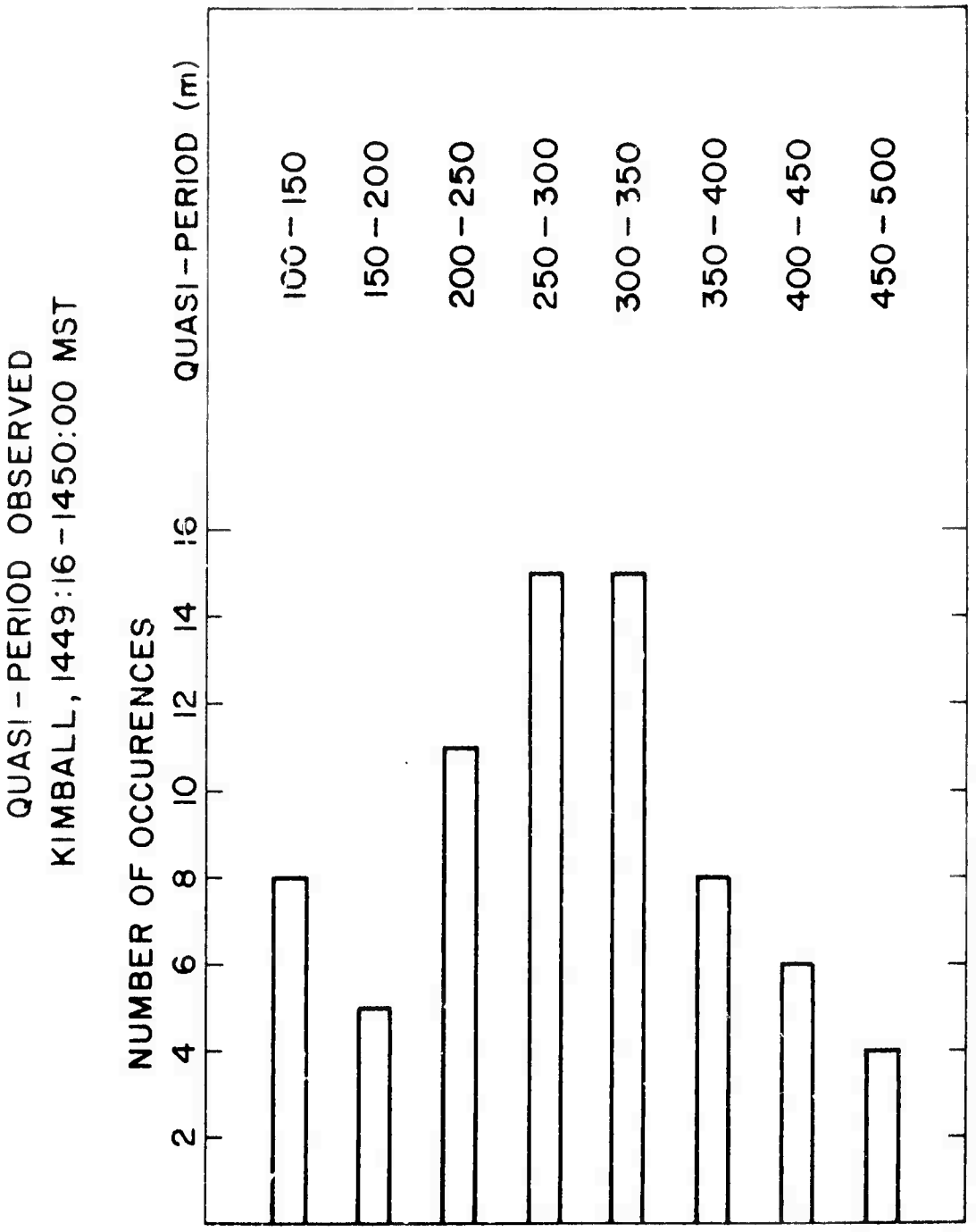

Figure 4.9
Frequency distribution of α for an orbital pass (U)

the structure size (d) is given by

$$d = \alpha/2.56 \qquad (4.6)$$

The data analysis presently planned will determine the validity of (5) in describing the observed fading.

(S) It is interesting to compare the orbital quasi-periods of Figure 4.9 with the corresponding structure sizes found in Prairie Smoke I by the geostationary technique (Bowhill and Mendenhall, 1972, pp. 32-33). The latter experiment showed spatial quasi-periods between 200 and 600 m, with an average of about 300 m, in good agreement with the orbital data of Figure 4.9.

(S) At Buford three antennas spaced in a right triangle were recorded (N-S spacing of 250 ft and N, W-E spacing of 235 ft). Since the time correlation observed at the three antennas was almost perfect, the pattern on the ground appears to be highly elongated. The locus of points of maximum cross correlation form a straight line known as the line of maxima, and the orientation of the line of maxima is entirely dependent on the satellite look angles as demonstrated earlier by Bowhill and Mendenhall (1972).

(S) The geometry for the Buford site location and a pass which is east of overhead is given by the following relations:

$$\theta = \psi + \arctan\left(\sin\delta/(\tan G \cot\varepsilon - \cos\delta)\right) \qquad (4.7)$$

where

$\psi = (180 - \beta)$ where β is the satellite azimuth from the observation site

$\delta = (D + \psi)$ where D is the magnetic dip in the region of the irregularities

G = Dip of the magnetic field in the region of the irregularities

ϵ = Elevation of the satellite from the observation site.

For the antenna configuration used at Buford the observed orientation is given by the following relations:

$$\theta = \arctan\ (d_l t/dt_l) \tag{4.8}$$

where

d_l = N, W-E spacing

t_l = Time shift for maximum cross correlation between the N, W and I antennas

d = N, W-S spacing

t = Time shift for maximum cross correlation between the N, W and S antennas.

A few samples of data were analyzed by measuring the time shifts for maximum cross correlation from chart recordings. The results are shown in Table 4.3, where the magnetic dip was taken to be 14 deg for the calculated values based on the geometry of the satellite pass.

(S) The agreement between the measured orientation in Table 4.3 and the orientation calculated on the basis of field-alignment of the irregularities confirms that the assumption of field-alignment is well justified.

Table 4.3

Orientation of line of maximas observed during orbital pass (U)

TIME MST 16 FEB. 72	SATELLITE		DELAY, msec		DEGREES WEST OF NORTH	
	ELEV.	AZIM.	N-S	E-W	MEAS.	CALC.
1900:58	56.8	166.6	35.0	30.0	47.6	46.0
1900:58	56.8	166.6	42.5	30.0	53.0	46.0
1901:01	58.8	166.3	40.0	22.5	59.1	49.1
1901:05	59.1	165.8	30.0	20.0	54.6	51.9
1901:10	60.5	165.0	35.0	17.5	58 2	57.0
1901:18	62.8	164.0	37.5	15.0	67.0	66.4

SECRET

5. RESULTS OF PRAIRIE SMOKE II (U)

(S) In Prairie Smoke II for the first time, orbital and geostationary data were available simultaneously.

5.1 Results of the Geostationary Experiment (U)

(S) Based on the geostationary data listed in Table 3.3, the scintillation index S has been calculated using the formula (1) of Section 3.3. It was found to vary greatly during the experiment. To facilitate comparison with other data, it has been calculated for a 2-minute interval fifteen minutes after each hour when the transmitter was operating. These results are given in Table 5.1. Comparison of these data with parameters such as the data from the phased array, the spread observed on the ionosonde, the heater reflection height and the heater frequency relative to the critical, will give insight into a yield model of the disturbed region.

(S) An example of the deep fading frequently observed is shown in Figure 5.1. In this case, the autocorrelation function was found to have an e-folding time of about 11 seconds (Figure 5.2). Its shape generally supports the Gaussian form assumed for the autocorrelation function in Equation 4.6.

(S) A survey of the real-time chart recordings indicates that the fading was generally deeper after 1800 MST. Typical values of S during the morning and afternoon hours were 1-5%, while deep fading (S $\sim$ 5-25%) was frequently observed during the evening hours. The results of the orbital experiments have not shown the same dependence on time of day, suggesting that at least part of the day/night variation is an effect of the change in height of the ionosphere from day to night. Apparently, the disturbed region was closer to the satel-

Table 5.1

Scintillation Index

Calculated From Geostationary Satellite Data (U)

DATE 1972	TIME (MST)	SCINTILLATION INDEX (%)
24 April	11:15	< 1.0
	12:15	< 1.0
	13:15	4.3
	14:15	2.7
	15:15	2.2
	16:15	< 1.0
25 April	6:15	< 1.0
	7:15	3.3
	8.15	4.5
	9:15	5.6
	10:15	< 1.0
	11:15	< 1.0
4 May	9:15	3.3
	10:15	2.2
	11:15	3.6
	12:15	< 1.0
	13:15	1.7
	14:15	2.5
	15:15	< 1.0
	16:15	2.8
	17:15	4.8
	18:15	9.6
	19:15	5.7
	20:15	12.0
	21:15	10.0

Table 5.1 cont.

DATE	TIME (MST)	SCINTILLATION INDEX (%)
5 May	11:15	< 1.0
	12:15	3.4
	13:15	< 1.0
	14:15	3.3
	15:15	2.9
	16:15	7.5
9 May	6:15	2.4
	7:15	1.2
	8:15	3.2
	9:15	2.5
	10:15	4.0
	11:15	2.6
	12:15	3.1
	13:15	3.9
	14:15	< 1.0
10 May	17:15	< 1.0
	18:15	4.1
	19:15	4.4
	20:15	5.3
	21:15	25:5
11 May	16:15	3.5
	17:15	2.9
	18:15	4.9
	19:15	< 1.0
	20:15	5.7
	21:15	13.7
12 May	11:15	< 1.0
	12:15	< 1.0
	13:15	< 1.0
	14:15	< 1.0

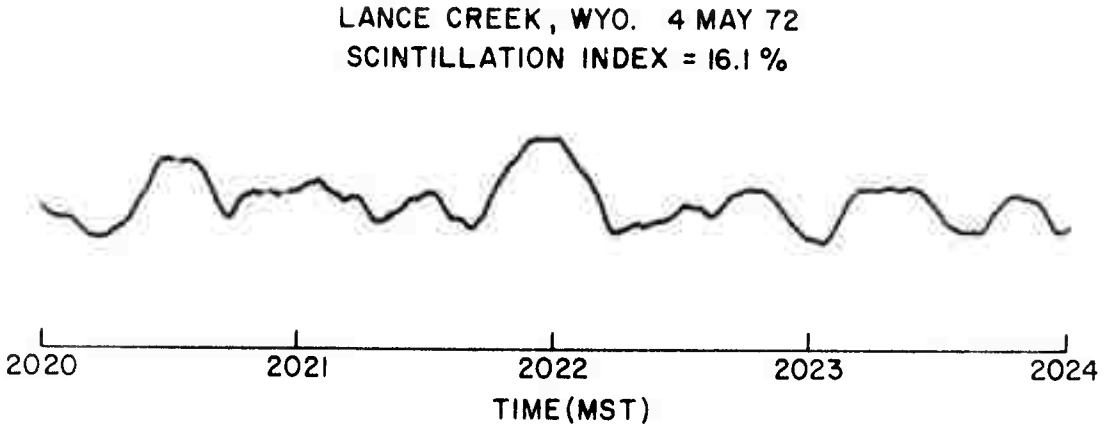

Figure 5.1
A sample of the geostationary data (U)

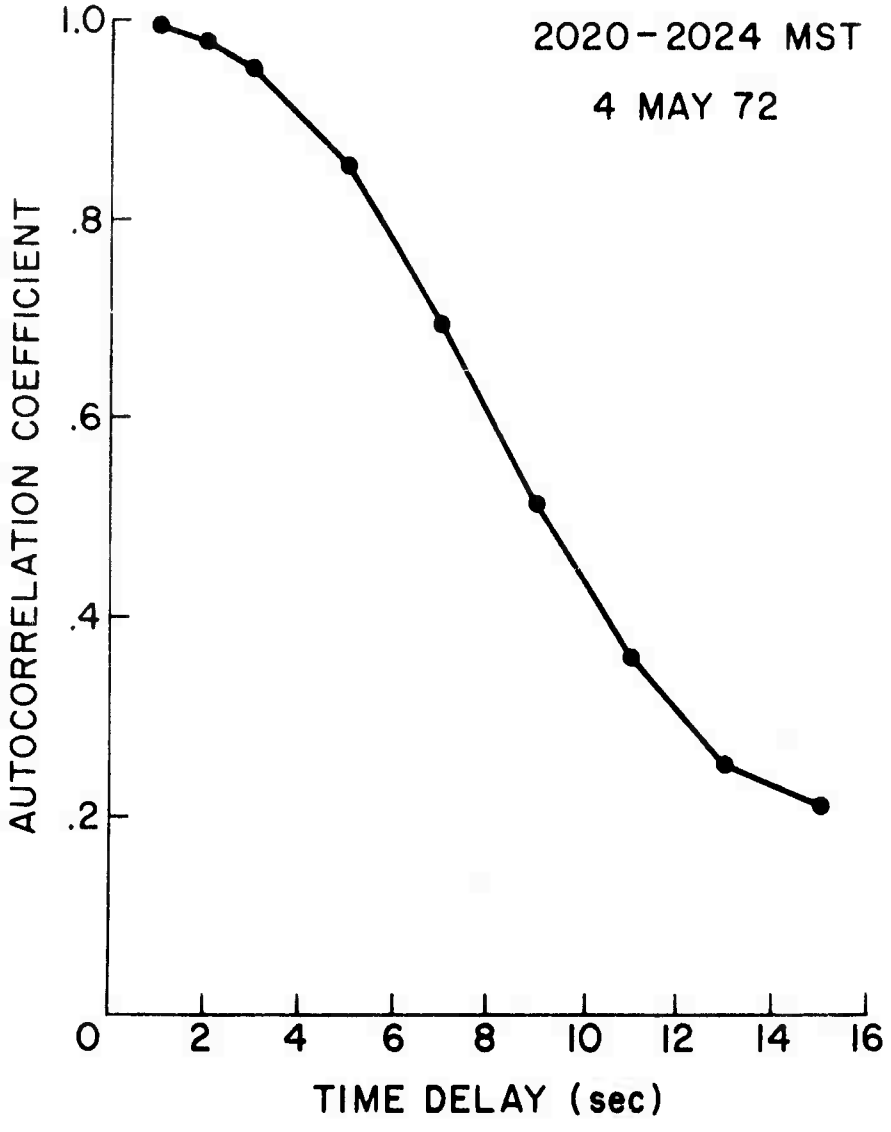

Figure 5.2

Autocorrelation coefficient for a sample of the geostationary data. (U)

lite LOS during the night hours. In fact, orbital data seemed to show little dependence of yield on time of day. The maximum value of S for a 4-second interval was found to be 12.9% at Pine Bluffs, Wyo. on Dec. 6, 1971 and 12.6% at Kimball, Neb. on Feb. 15, 1972. These were two afternoon passes. In Section 5.2 an evening pass on May 10, 1972 is described showing a similar value of 13.3%.

(S) The frequency distribution of the spatial quasi-period observed at the geostationary site is shown in Figure 5.3 for a sample of the data collected on May 10, 1972. It shows general agreement with the results of the orbital experiment and with the previous geostationary data from Prairie Smoke I.

(S) A survey of the real-time chart records was made to determine onset and decay times and any dependence with transmitter power and $fof2/f_H$. The scatter plots in Figure 5.4 show the results for the onset times. The decay times were observed to vary from a few minutes to in excess of a half-hour and were gererally longer at night. No very pronounced correlation is found with heater frequency or input power.

(S) Examination of the geostationary records show that the drift velocity was typically 30-60 m/sec and moving toward either the east or west. On May 11, 1972 at 2000 MST the direction of the structure motion was observed to gradually shift from being easterly to westward, as found in Prairie Smoke 1.

(S) The geostationary data is being further analyzed to provide information concerning the axial ratio, orientation, and drift velocity based on the cross-correlation functions of spaced-antenna records.

5.2 Results of the Orbital Experiment (U)

(S) Only a limited amount of the orbital data has been fully analyzed at this time, but reported in this section are the results of a pass observed from Kimball, Neb. with spaced-antenna records were of good quality for both the

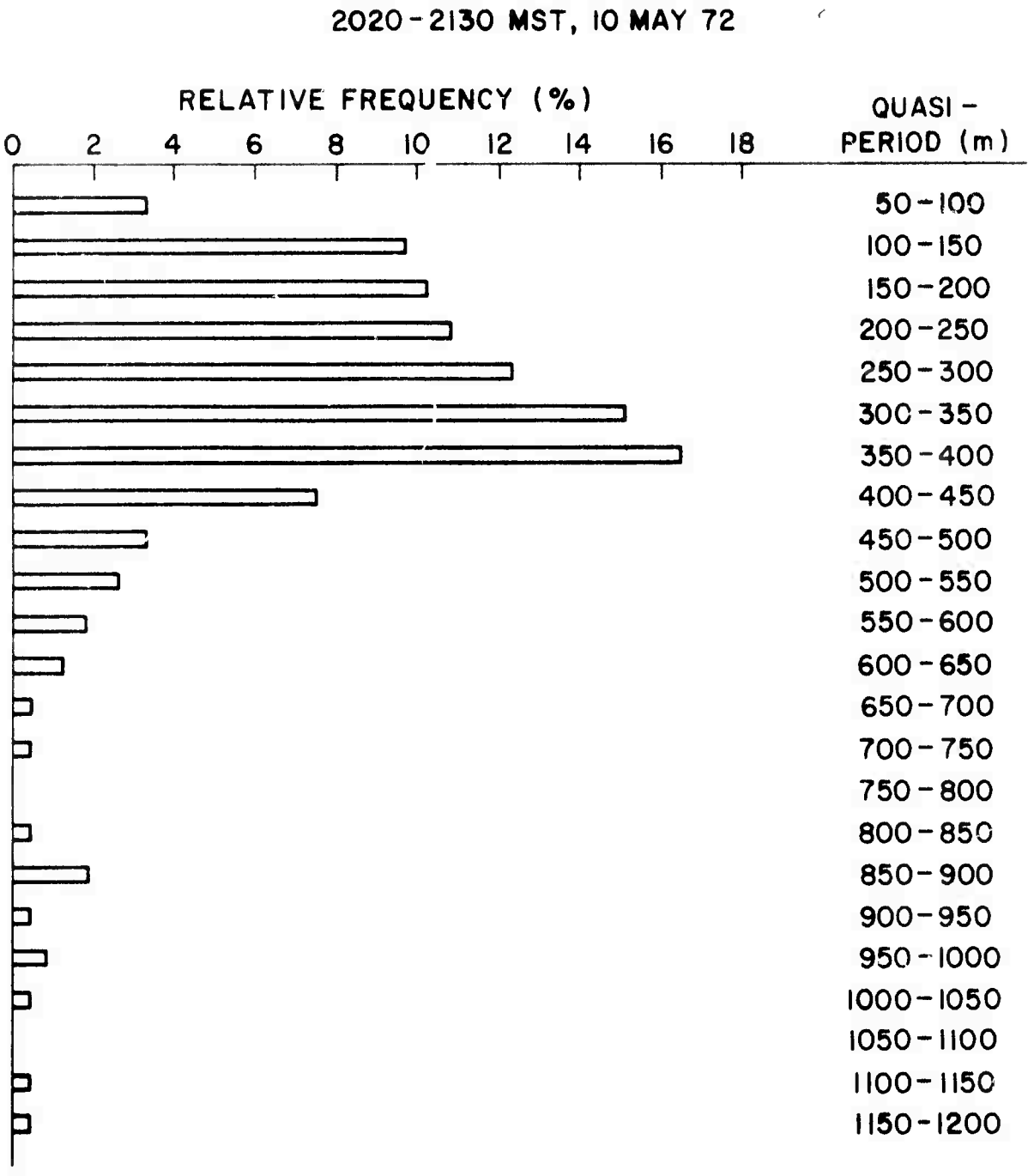

Figure 5.3

Spatial quasi-periods observed at the geostationary site. (U)

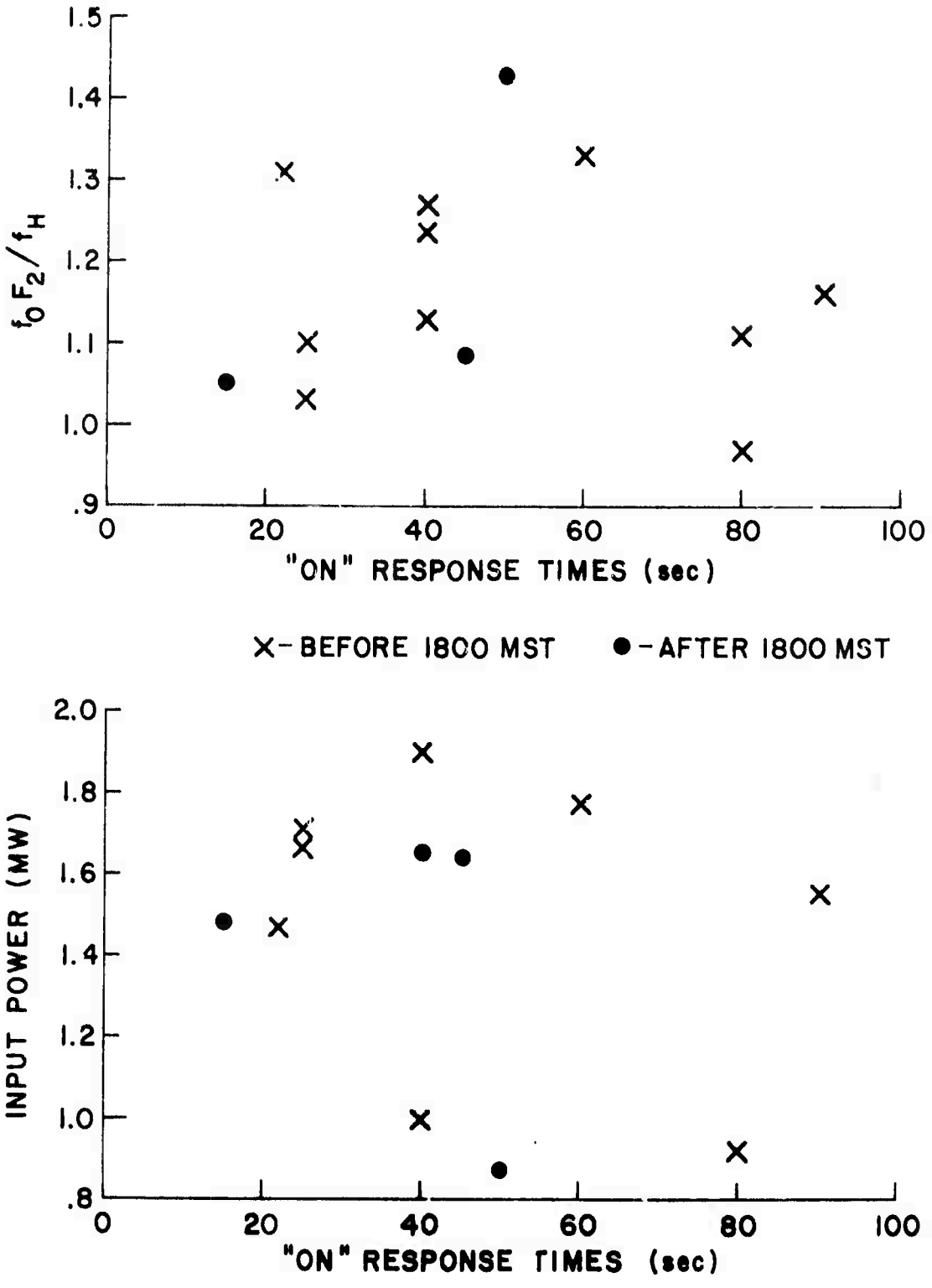

Figure 5.4

Onset times observed at the [illegible]stationary site. (U)

150 and 400 MHz signals. The index S has been calculated at 4-second intervals and is shown in Figure 5.5. A portion of the spaced-antenna chart recording for the 400-MHz signal is shown in Figure 5.6.

(S) When the data of Figure 5.5 are used to form a scatter plot (Figure 5.7) it is evident that the ratio of the fading depth (while showing considerable variability) corresponds approximately to an inverse frequency dependence for the scintillation index. This result agrees with the diffraction theory of Briggs and Parkin (1963) for irregularities located in the far-field or Fraunhofer region. The conditions for this result are that the RMS phase deviation be less than unity and that

$$\lambda z/D^2 > \pi\sqrt{3} \qquad (5.1)$$

where

z is the effective distance from the scatterers, given by $z_1 z_2/(z_1 + z_2)$

z_1, z_2 are the distances from the irregularities to the observer and source, respectively

λ is the wavelength of the source signal

D is the e-folding distance for the transverse correlation function of the irregularities.

(S) The height distribution of the irregularities has been calculated in a manner similar to that described in Section 4 and is shown in Figure 5.8 for both frequencies. The most striking feature of this variation of height with time is the rapid increase at 2032:10 MST and the corresponding abrupt decrease at 2032:55. It is easy to explain this variation if one considers the geometry of the satellite pass.

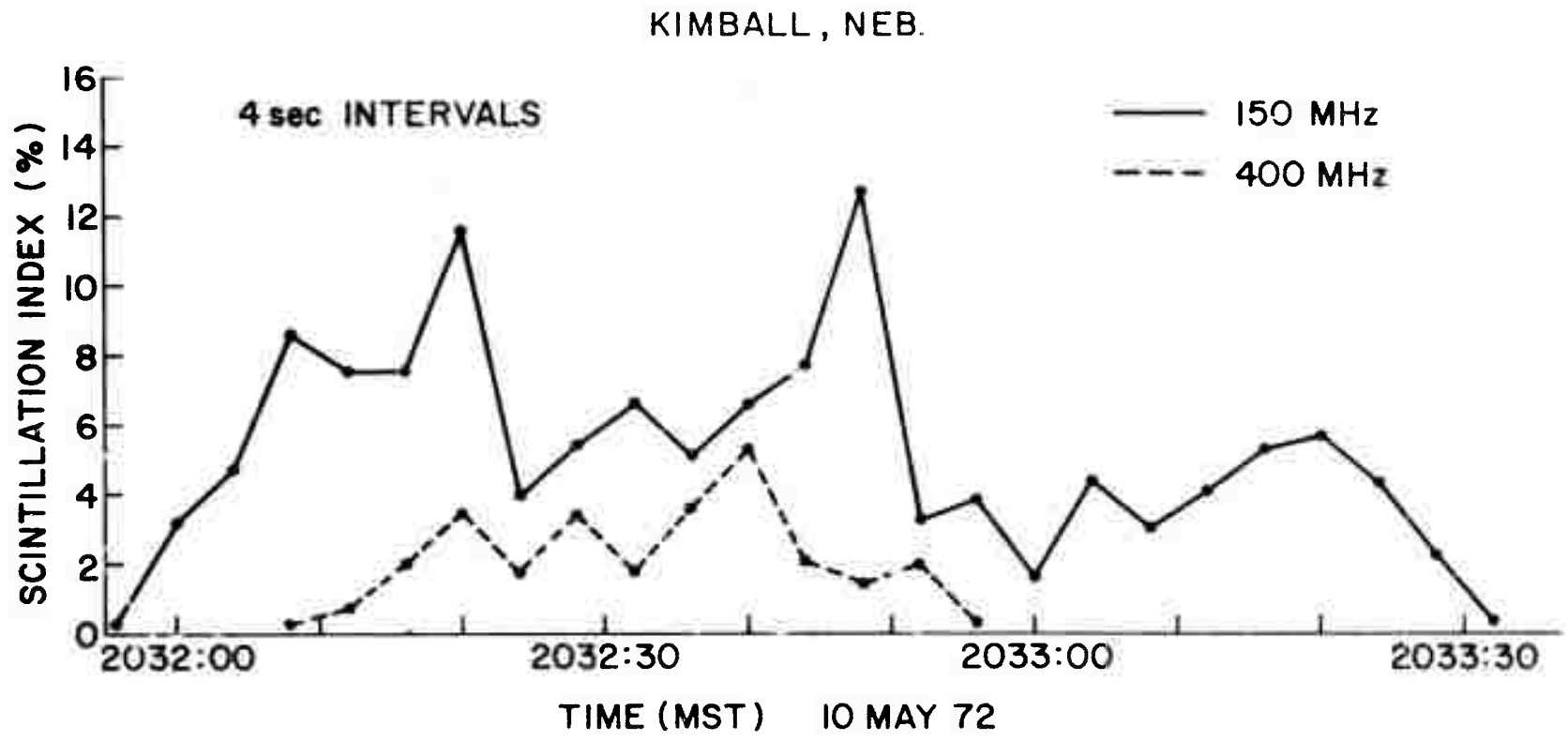

Figure 5.5
Scintillation index observed for an orbital pass. (U)

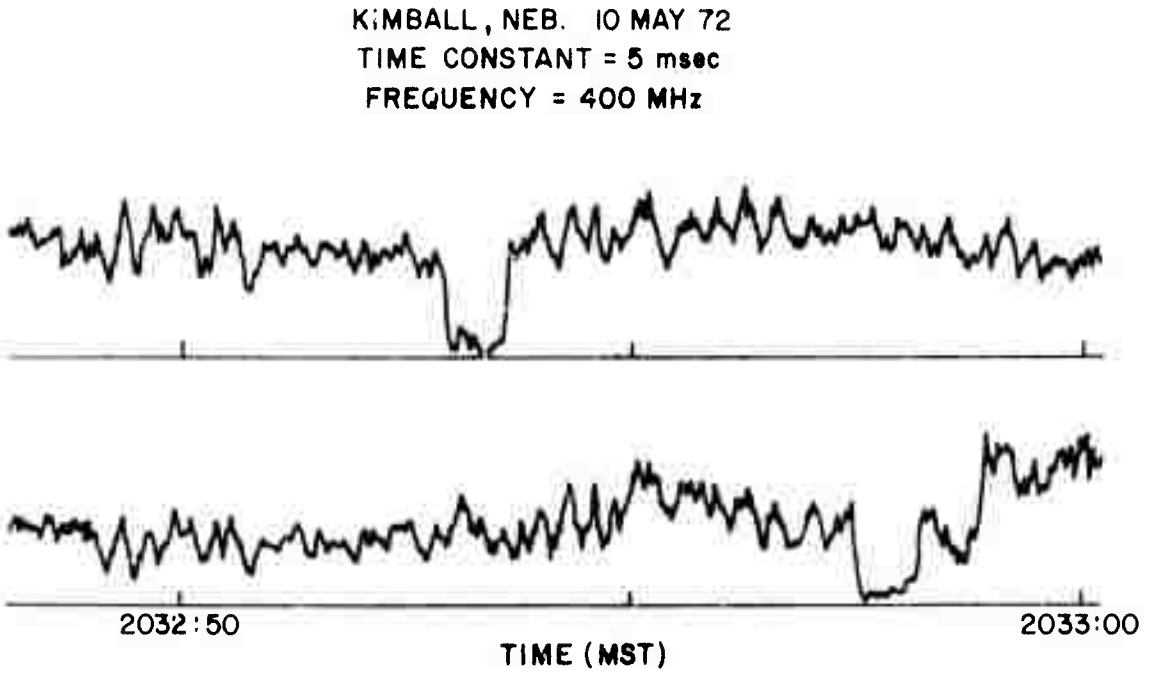

Figure 5.6

Sample of spaced antenna records for an orbital pass (U)

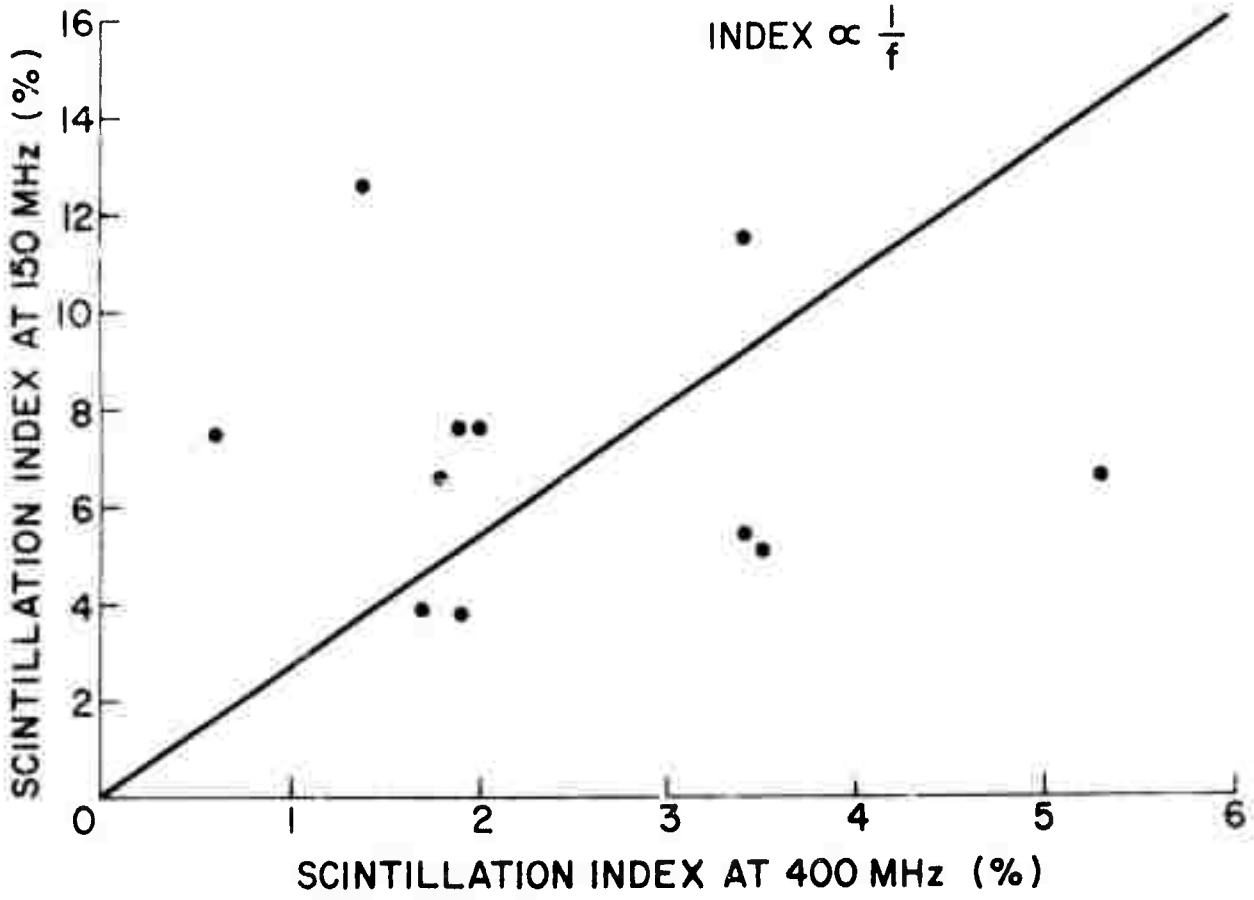

Figure 5.7

Scintillation index observed at two frequencies (U)

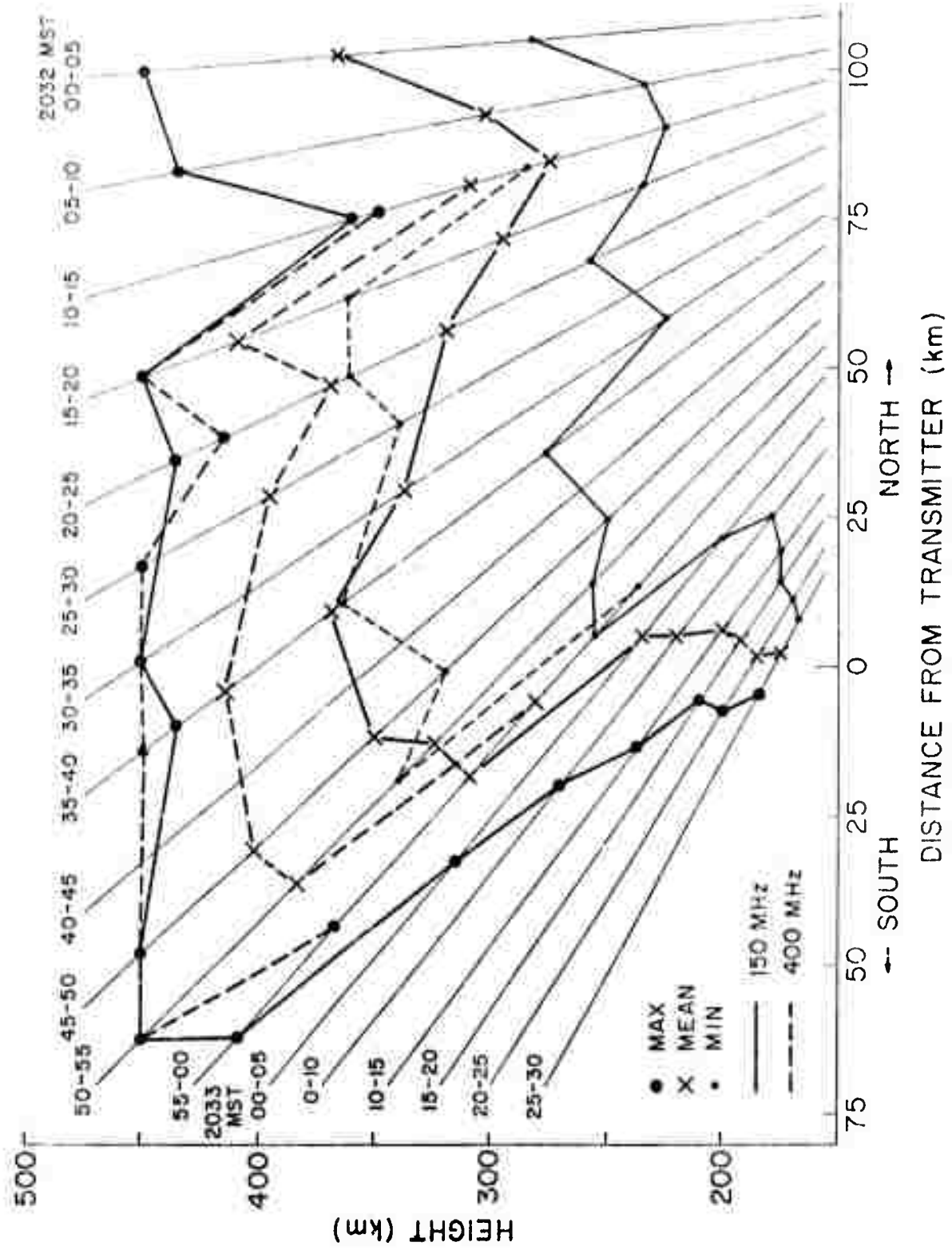

Figure 5.8

Range of heights observed for an orbital pass (U)

(S) Imagine that the disturbed region is confined within a cylinder parallel to the lines of the earth's magnetic field, with its projection on a 300-km-altitude plane a circle with radius X. Let the center of this circle be a distance x_0 to the magnetic north of Platteville. Then, for various assumptions about X and x_0, heights can be calculated for the entry and emergence of the satellite LOS from the cylinder containing the disturbed region. Figure 5.9 shows these curves for three cases of interest. The area contained by these curves represents the height range over which scintillations may be expected, as a function of time during the satellite pass.

(S) Of course, a particular height will only give scintillations as long as substantial ionization is present. Assume, therefore, that 200 km is the lower limit for the disturbed region. It is evident that the model for x_0 = 300 km, X = 50 km gives a height for the scintillation region that increases from 200 km at 2032:00 to 200-450 km at 2032:40; decreasing again to 200 at 2033:10. This is exactly the height variation shown in Figure 5.8. Further, since the depth of the scintillation increases as the thickness of the disturbed region increases, the scintillations should have started around 2032:00, passed through a maximum at 2032:40 and disappeared at 2033:10. Comparison with Figure 5.5 confirms this model. The additional scintillation seen between 2033:10 and 2033:30 must arise, according to Figure 5.8, from irregularities below 200 km altitude at the southern edge of the region.

(S) The quite different behavior of the height shown in Figure 4.8 is easily explained in terms of the different geometry involved. Figure 5.10 is a plot similar to Figure 5.9 for the satellite pass of Figure 4.8 and Figure 4.3. Comparison with Figure 4.3 suggests that in this case x_0 = -30 km, X = 50 km; and because of the different shape of the contour on Figure 5.10, the effective height increases continuously through the satellite pass.

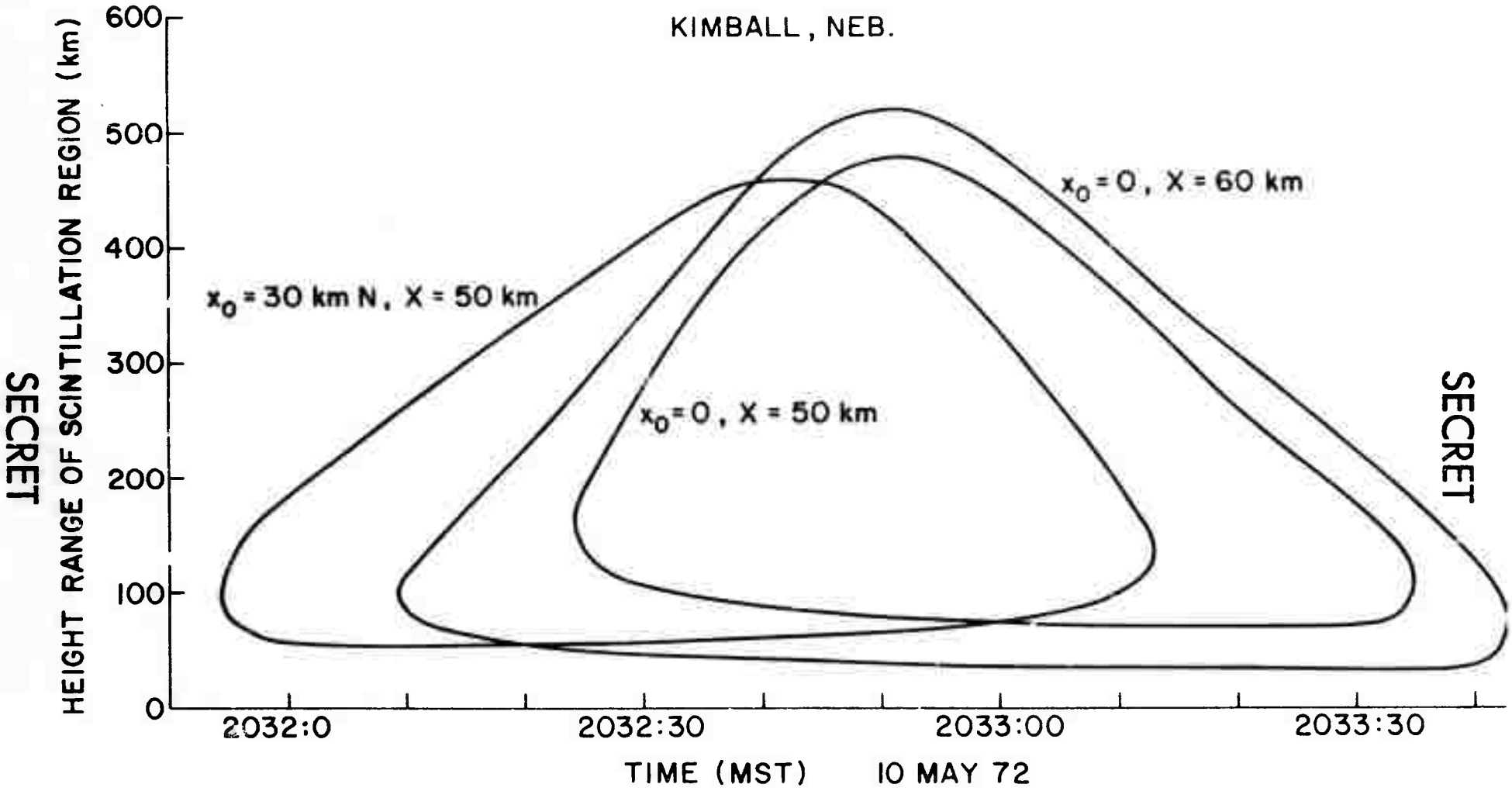

Figure 5.9

Height ranges calculated for an orbital pass (U)

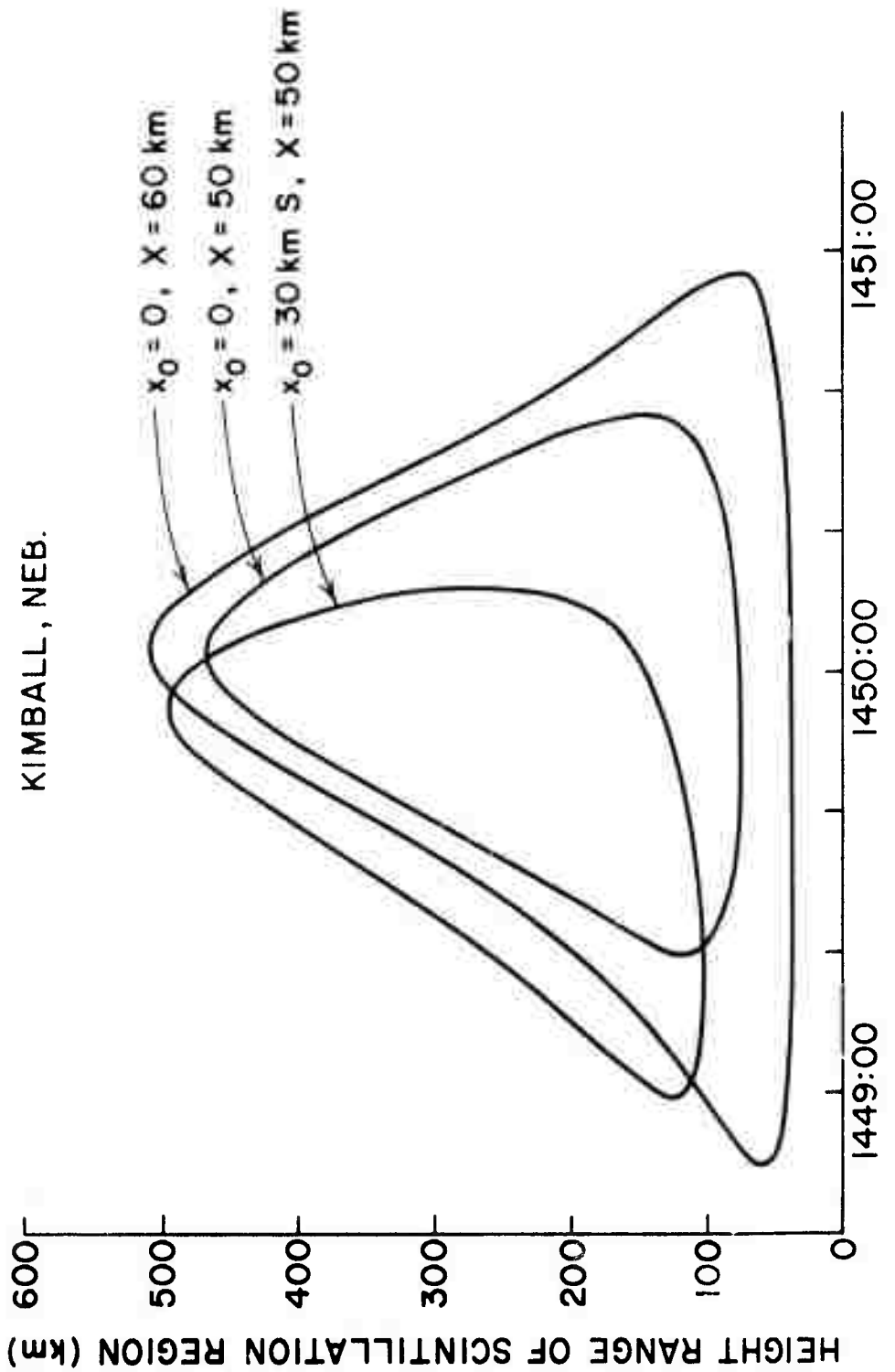

Figure 5.10

Height ranges calculated for an orbital pass (U)

(S) The RMS phase fluctuation λ for a wave propagated through a thickness Δh of a random medium has been given by Briggs and Parkin (1963) as

$$\gamma^2 = \left(\frac{\pi D^2 E^2}{E^2 \sin^2 \psi + D^2 \cos^2 \psi}\right)^{1/2} r_e^2 \lambda^2 \overline{\Delta N^2} \Delta h \sec i \qquad (5.2)$$

where D and E are the e-folding correlation distances perpendicular and parallel to the magnetic field, respectively; ψ is the angle between the wave normal and the magnetic field; r_e is the classical electron radius; $\overline{\Delta N^2}$ is the mean square electron-density fluctuation; and i is the angle between the wave normal and the vertical.

(S) Since E >> D it may be rewritten in more familiar notation as

$$\gamma^2 = \frac{\pi^{5/2}}{\lambda^2} \left(\frac{f_N}{f}\right)^4 \left(\frac{\Delta N}{N}\right)^2 \Delta h \; D \sec i \operatorname{cosec} \psi \qquad (5.3)$$

where f_N is the plasma frequency and f the wave frequency. Since f_N varies with altitude, this may be rewritten in the following way:

$$\gamma^2 = \frac{\pi^{5/2}}{\lambda^2} \left(\frac{foF2}{f}\right)^4 \left(\frac{\Delta N}{N}\right)^2 D \sec i \operatorname{cosec} \psi \int (N/N_m)^2 \, dh \qquad (5.4)$$

on the assumption that the fractional RMS electron-density fluctuation is independent of altitude. The integral is typically about 120 km.

(S) For the scale of irregularities corresponding to D = 150 m, far-field conditions prevail, and the RMS amplitude fluctuation ε is therefore given by

$$\varepsilon = \gamma/\sqrt{2} \; . \qquad (5.5)$$

Figure 5.5 illustrates an orbital pass and shows that ε goes inversely as frequency, confirming the far-field condition. The following values of the parameters apply to this pass:

γ = 0.075

τ = 0.052

f = 400 MHz

foF2 = 6.0 MHz

i = 26.6 deg

ψ = 13.1 deg

D = 120 m

$\int (N/N_m)^2 dh$ = 120 km

Solving equation (5.5) with these values, the RMS fractional fluctuation in electron density is found as 6.9×10^{-3}.

6. DISCUSSION OF RESULTS OF PRAIRIE SMOKE Ib and II (U)

(S) The orbital data from Prairie Smoke Ib and II generally confirmed the conclusions from the geostationary data of Prairie Smoke I and the orbital data of Prairie Smoke Ia. Simultaneous observations at 150 and 400 MHz showed an inverse frequency variation of scintillation depth, and confirmed the Briggs-Parkin diffraction theory. The structures of ASF were confirmed to be field-aligned. The observations indicated a scattering model with striations contained in a field-aligned cylinder, radius 50 km, with its lower face at 200-km altitude, and centered approximately over the heater at 300-km altitude. The electron-density fluctuation was about 0.1 percent RMS at the center of the region.

(S) Continuous geostationary scintillations showed marked fluctuations in scintillation index which may be correlated with changes in height of the F2 layer.

(S) Based on these data, a scattering model has been prepared for preliminary applications evaluation and is described in Sections 7 and 11.

7. PURPOSE AND SCOPE OF MODEL (U)

(S) In order to evaluate the possible applications of irregularities produced by heating of the ionospheric F region, it is necessary to describe the irregularities by a simple scattering model. In determining the scope of such a model, it is useful to consider two boundary conditions that circumscribe its degree of elaboration:

(i) It should not be simply a compilation of cross sections observed between pairs of transmitting and receiving stations in different locations at different frequencies, but should be a self-consistent description of the scattering medium itself; albeit in simplified terms.

(ii) It need not be devised to be in agreement with any particular aspect of plasma instability theory, unless that agreement has been fully verified empirically.

(S) Evidently, this approach will lead to an empirical description of the scattering irregularities which could be aptly described as an "engineering model" rather than a "physical model". Nevertheless, given the present uncertainties in the physical mechanisms involved, it seems to be the only approach that can lead to a description of the disturbed region with a relatively small number of parameters.

(S) The model should be capable of estimating numerically the following quantities:

(a) The total power scattered in a given direction by the disturbed region when illuminated by a given frequency from a transmitting antenna with any prescribed polar diagram and pointing direction relative to

the center of the disturbed region.

(b) The distribution in range of the scattered power (for multipath considerations).

(c) The amplitude and phase fluctuation to be expected in a signal of specific frequency transmitted through the irregular region from the ground to space (or vice versa).

(S) Because of the variability of the phenomenon, it seems clear that some limitations must be imposed on this model these are described in the next section.

7.1 Limitations of the Model (U)

(S) This first scattering model is limited to the following conditions:

(i) Heating from the Platteville transmitter, with full power, the antenna pointed directly overhead.

(ii) Ordinary-mode heating.

(iii) Heater frequency less than foF2.

(iv) Daytime conditions typical of the larger cross sections and scintillations observed.

(v) On-frequency scatter only (rather than plasma line).

(S) It is possible that optimum conditions may later be discovered giving much greater yields than are indicated by the present model. Nevertheless, it gives a basis on which to build a later model.

(S) The model is treated in three parts, each in a separate section: the magnetic field; the on-frequency scatter (OFS); and the artificial spread F (ASF).

8. MAGNETIC FIELD MODEL (U)

(S) Both OFS and ASF have been established as critically dependent on the magnetic field direction. Thome (1972) has used a 99-term magnetic field model to predict the properties of the magnetic field over Platteville. A simpler approach is suggested here which apparently gives adequate accuracy for most purposes.

(U) The magnetic dip δ_0 around a magnetic dipole is given by the equation

$$\tan \delta_0 = 2 \tan \lambda_{m0} \tag{8.1}$$

and is constant with altitude over a point P with magnetic latitude, λ_{m0}. Therefore, the actual magnetic dip over another point Q in the neighborhood of P and on the same magnetic meridian can be conveniently represented by the equation

$$\tan \delta = 2 \tan \lambda_m \ . \tag{8.2}$$

The magnetic latitude λ_m of the point Q is given to a close approximation by the equation

$$\lambda_m = \lambda_{m0} + (\lambda - \lambda_0)\sec \alpha \tag{8.3}$$

where λ_0 and λ are the geographic latitude of P and Q, respectively, and α is the magnetic declination.

(S) Using these equations, the altitude h_Q of the specular reflection point may be calculated for any bistatic radar pair. In addition, the magnetic dip δ_0 at the point P may be adjusted so as to fit the observed altitudes of field-aligned scatter. Figure 8.1 shows a comparison of h_Q for White Sands with the Raytheon calculation of Thome (1972) and magnetic dips δ_0 of 67.7 and 68.2 deg over Platteville. The effect of small changes in magnetic dip by far outweighs the small differences between the dip-latitude model and the 99-coefficient model. Accordingly, the dip latitude model is adopted in the succeeding sections.

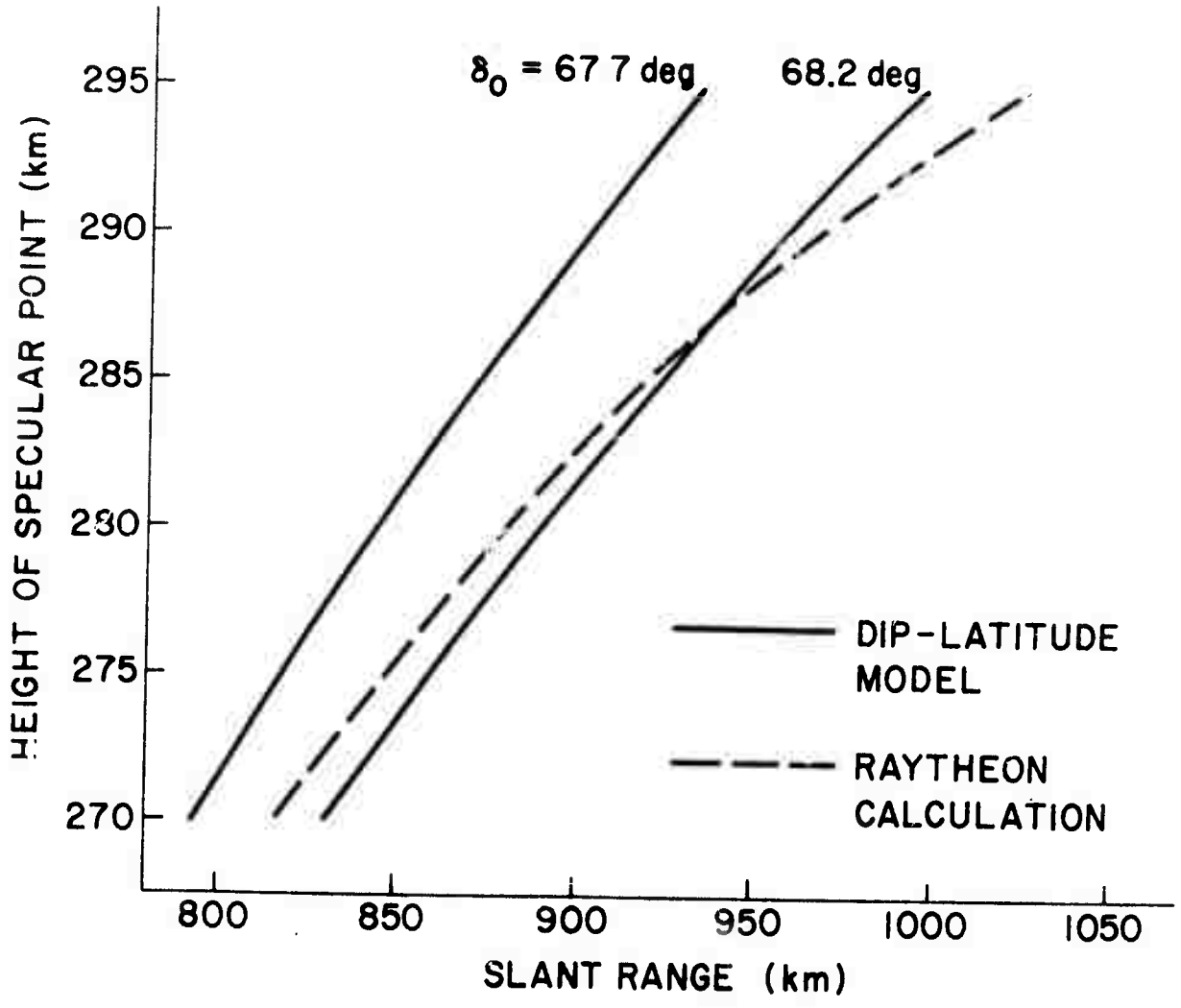

Figure 8.1

Height of specular point vs slant range for a dipole model and the 99-term model provided by Raytheon. (U)

9. SMALL-IRREGULARITY MODEL (U)

(S) In treating on-frequency scatter (OFS), there are several questions that need to be resolved:

(1) How can the aspect dependence of the scattering irregularities be distinguished from the effects of thickness of the scattering layer?

(2) How can the scattering cross section best be characterized when the scattering medium is comparable with the size of the antenna beam?

(3) To what extent is the range spread of the irregularities determined by the combination of aspect sensitivity and disturbed-region thickness, compared with the effects of the latitude extent of the heated region?

These three questions will be addressed in turn.

9.1 Thickness and Aspect (U)

(S) Imagine that the scatter irregularities are field-aligned, and are distributed with altitude h according to a function of I(h) given by

$$I(h) = \exp[-h - h_r)^2/A^2] \qquad (9.1)$$

where h_r is the altitude of reflection of the heater, defined as where the maximum of the Airy function occurs; and A is the e-folding semithickness of the disturbed region. The center of monostatic scatter from the irregularities will be at the height of h_Q of Section 8. Let the scattering polar diagram of the irregularities in the elevation plane have an e-folding semiwidth β, shown by Booker (1956) to be given by

$$\beta = \lambda/\sqrt{2}\,\pi\,L \qquad (9.2)$$

Where λ is the wavelength and L is the $\sqrt{e}$ -folding correlation distance along the magnetic field. Scatter from a height h rather than h_Q will have a scattering angle

$$\theta = 2(h - h_Q)/R \sin \delta \qquad (9.3)$$

where R is the slant range. The fraction of the total scattered energy which appears in the angle range θ to $\theta + d\theta$ is given by

$$J(\theta)d\theta = (1/\sqrt{\pi}\,\beta)\exp(-\theta^2/\beta^2)d\theta\ . \qquad (9.4)$$

Therefore, the fraction J(h)dh of the total scatter which appears to come from height h is given by

$$J(h)dh = (2/\sqrt{\pi}\,\beta R \sin \delta)\exp[-(h - h_Q)^2/(R\beta \sin \delta/2)^2]\ . \qquad (9.5)$$

The combined effects of aspect and thickness are therefore obtained, at a given slant range, by the integral

$$K = \int I(h)J(h)dh\ , \qquad (9.6)$$

assuming that the illuminating antenna gain is nearly constant over the height interval involved.

(S) Now it is certain that the effects of l(h) play a dominant part in determining the effective cross section; so that term cannot be neglected. Therefore, until further experimental evidence is available, it seems most appropriate to make the assumption that

$$A << R\beta \sin \delta/2 \ . \tag{9.7}$$

Under these circumstances, J(h) reduces to a δ-function

$$J(h)dh = \delta(h - h_Q)dh \tag{9.8}$$

and

$$K = I(h_Q) = \exp[-(h_Q - h_r)^2/A^2] \ . \tag{9.9}$$

Justification for this position can be presented as follows: Imagine that the irregularities extend all the way through the disturbed region, so that L = A. What would the value of A need to be so that the inequality (9.7) became an equality? Inserting Equation (9.2) into (9.7) the equality becomes

$$A^2 = R\lambda \sin \delta/2\sqrt{2}\pi \ . \tag{9.10}$$

Using R = 1000 km and λ = 2m, A = .5 km, approximately. It therefore follows that if the irregularities extend through the entire region, and are longer than 1 km, the replacement of (9.5) by (9.8) is fully justified. The Booker scattering formula then gives a cross section per unit area, the height dependence having been integrated out of (9.6) to give

$$K(h) = \exp[-(h_Q - h_r)^2/A^2] \quad . \tag{9.11}$$

(S) At a given range, therefore, the scattering is essentially from an east-west line at height h_Q. The range of elevation angles of the radar over which the scatter is observed will be determined by the convolution of the antenna beam with (9.1); the latter being equivalent to a Gaussian distribution with e-folding semiangle A/R sinδ. Typically, this elevation spread is determined by the antenna polar diagram, so the only information available at a given range is the scattering cross section and the altitude h_Q.

9.2 Cross Section Rationale (U)

(S) As indicated in Section 9.1, scattering at a given range comes from an arc at altitude h_Q. As a function of range, therefore, the returns must come from a surface determined by the variation h_Q with range. This surface is depicted in Figure 8.1, and its altitude depends on the magnetic dip. Therefore, it is meaningless to speak of a cross section per unit volume, in that the thickness in scatter of volume is much smaller than the antenna beam, and probably less than 1 km. Therefore, it is best to speak of a scattering cross section per unit area of the h_Q surface. Integrating the standard Booker expression with altitude at a given slant range gives the following expression for cross section σ_a per unit area

$$\sigma_a = (\pi^3 \lambda R T^2/\lambda_N^4) \exp(-8\pi^2 T^2/\lambda^2) \tag{9.12}$$

where ΔN/N is the fractional fluctuation in electron density, and T is the $\sqrt{e}$-folding correlation distance of the ionization irregularities transverse

to the magnetic field. The model proposed here suggests that the variation of electron-density fluctuation with latitude and height is given by

$$\overline{(\Delta N/N)^2} = \overline{(\Delta N/N)^2}_0 \exp[-(\lambda - \lambda_0)^2/(X^2/R_0^2) - (h - h_r)^2/A^2] \quad (9.13)$$

where $\overline{(\Delta N/N)^2}_0$ is the electron-density fluctuation across the magnetic field at the height of reflection h_r of the heater frequency, at the latitude λ_0 where the greatest energy is deposited; X is the e-folding distance of the heating effect in the north-south direction, and R_0 is the radius of the earth. The exponential factor in this latter equation will be used (with $h = h_Q$) in the next subsection to illustrate the way in which aspect reacts on to this problem.

9.3 Range Spread (U)

(S) The question arises as to how the parameters A, X, and δ_0 can be deduced from the experimental data. Figures 9.1 through 9.4 illustrate an appropriate procedure. They show the relative cross section as a function of slant range for a heated region centered 30 km north of Platteville, the magnetic dip of 86.2 deg, reflection height h_r of 275 and 300 km, heating radii X of 50 and 100 km, and thicknesses 2A of 10 through 200 km. Comparison of Figures 9.1 and 9.2 illustrate how the range extent of the return is governed at small thicknesses entirely by aspect, but at larger thicknesses by the heated region extent. Figures 9.3 and 9.4 show that the effect is even more striking with X = 50 km.

(S) This information may be presented another way, shown on Figure 9.5. For X = 100 km, this diagram shows the importance of the height of reflection in determining the highest apparent cross section (as a function of range). For

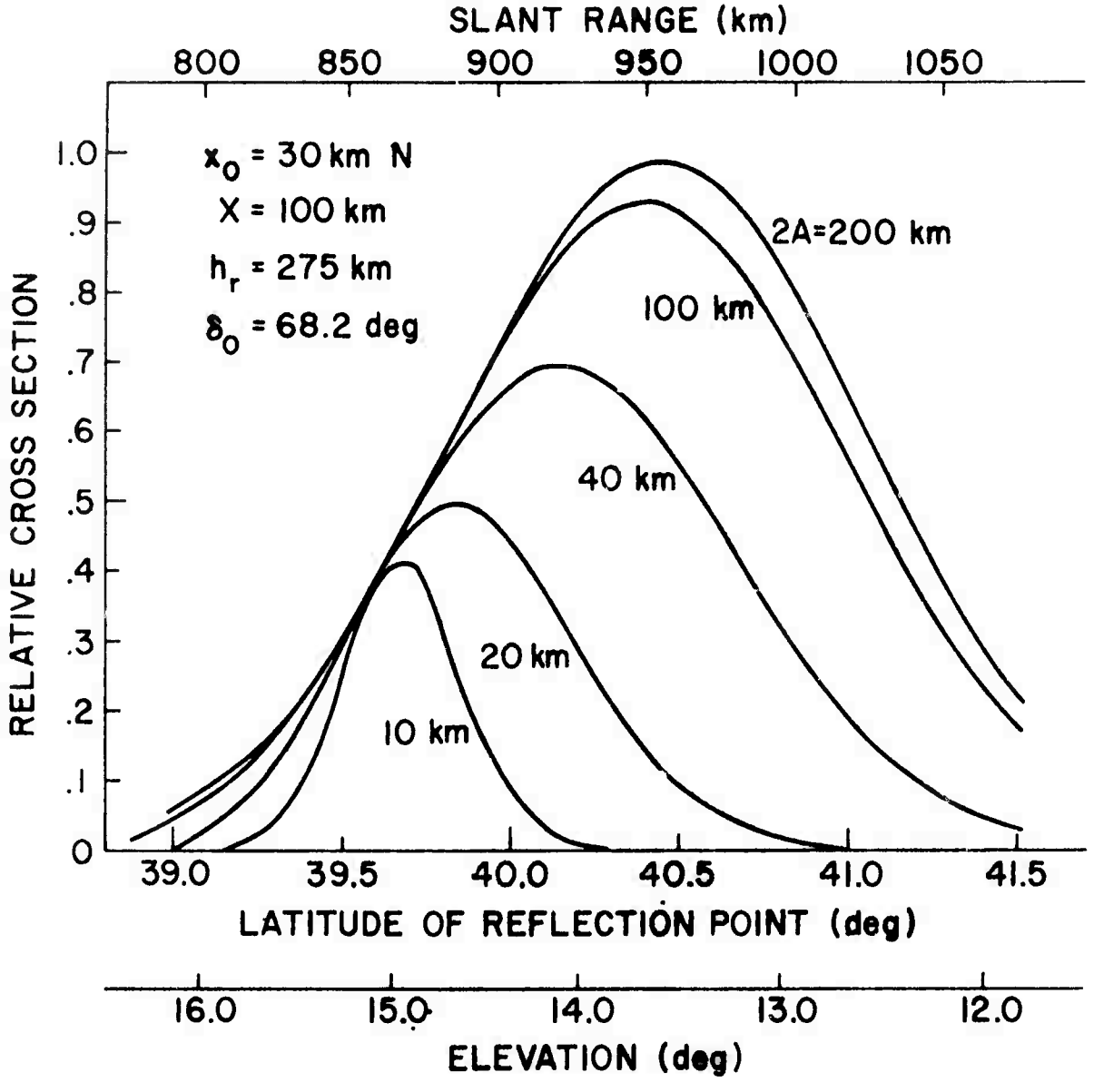

Figure 9.1

Relative cross section vs slant range and elevation for various values of 2A with X = 100 and h_r = 275 (U)

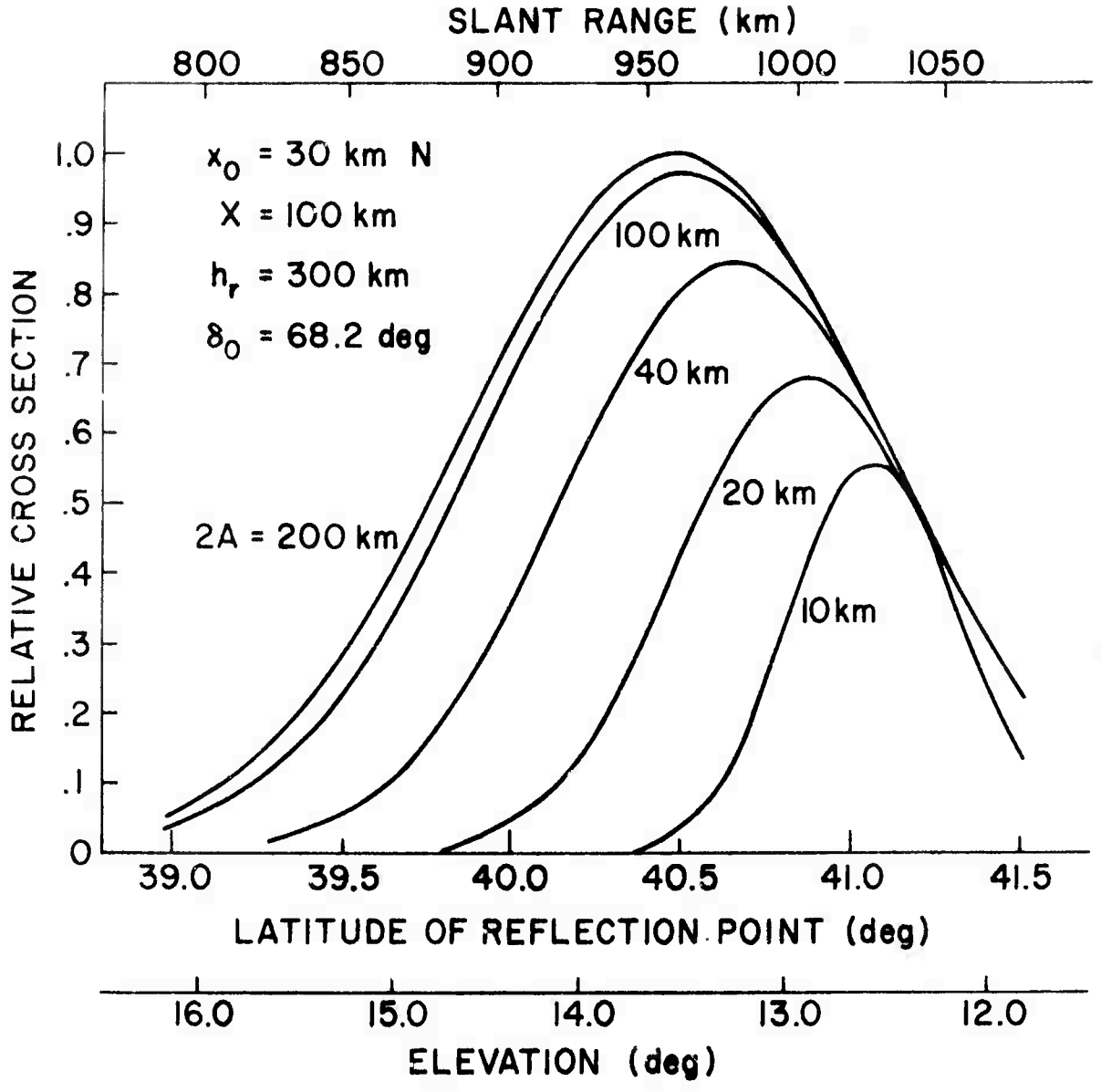

Figure 9.2

Relative cross section vs slant range and elevation for various values of 2A with X = 100 and h_r = 300 (U)

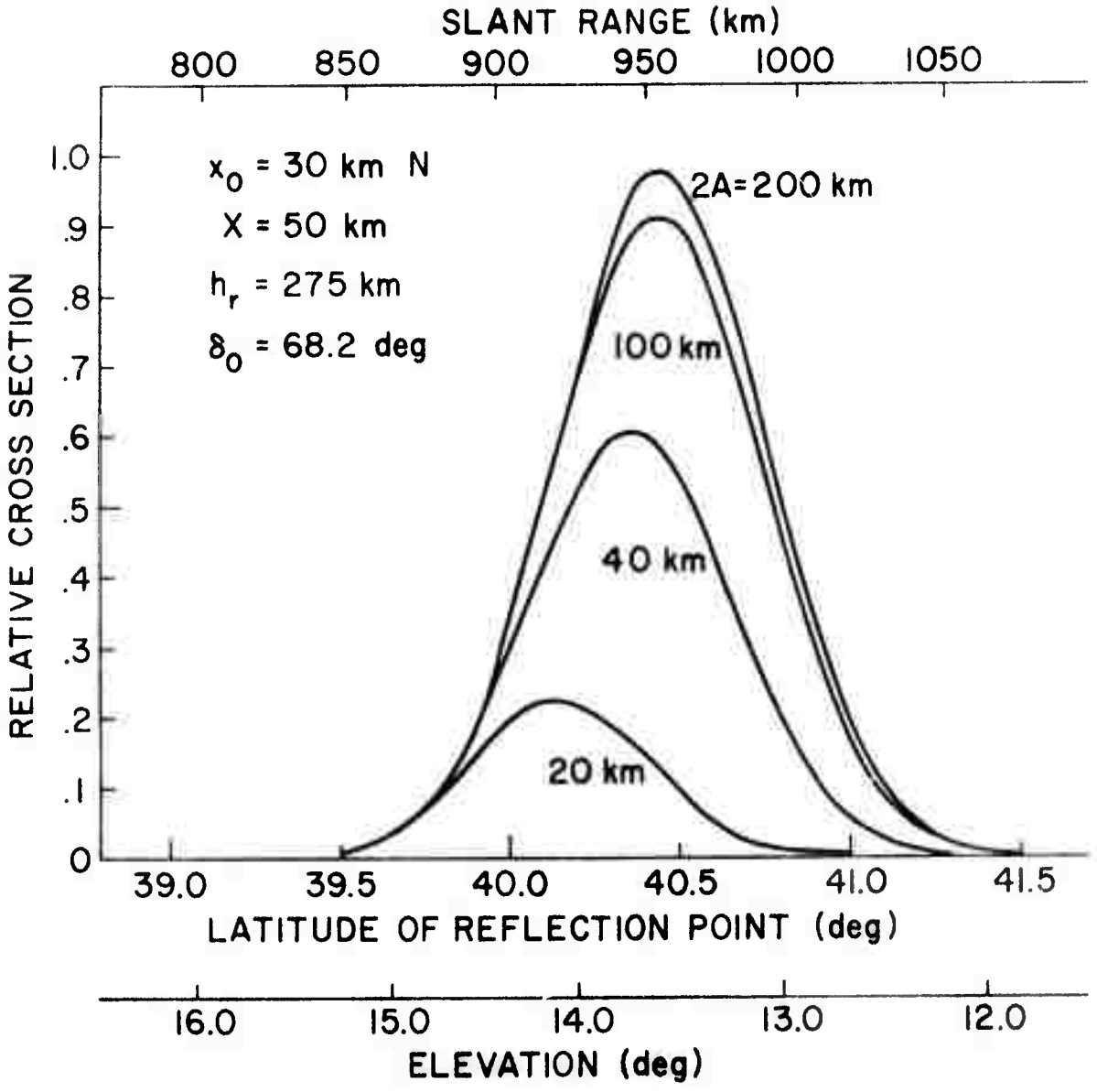

Figure 9.3

Relative cross section vs slant range and elevation for various values of 2A with X = 50 and h_r = 275 (U)

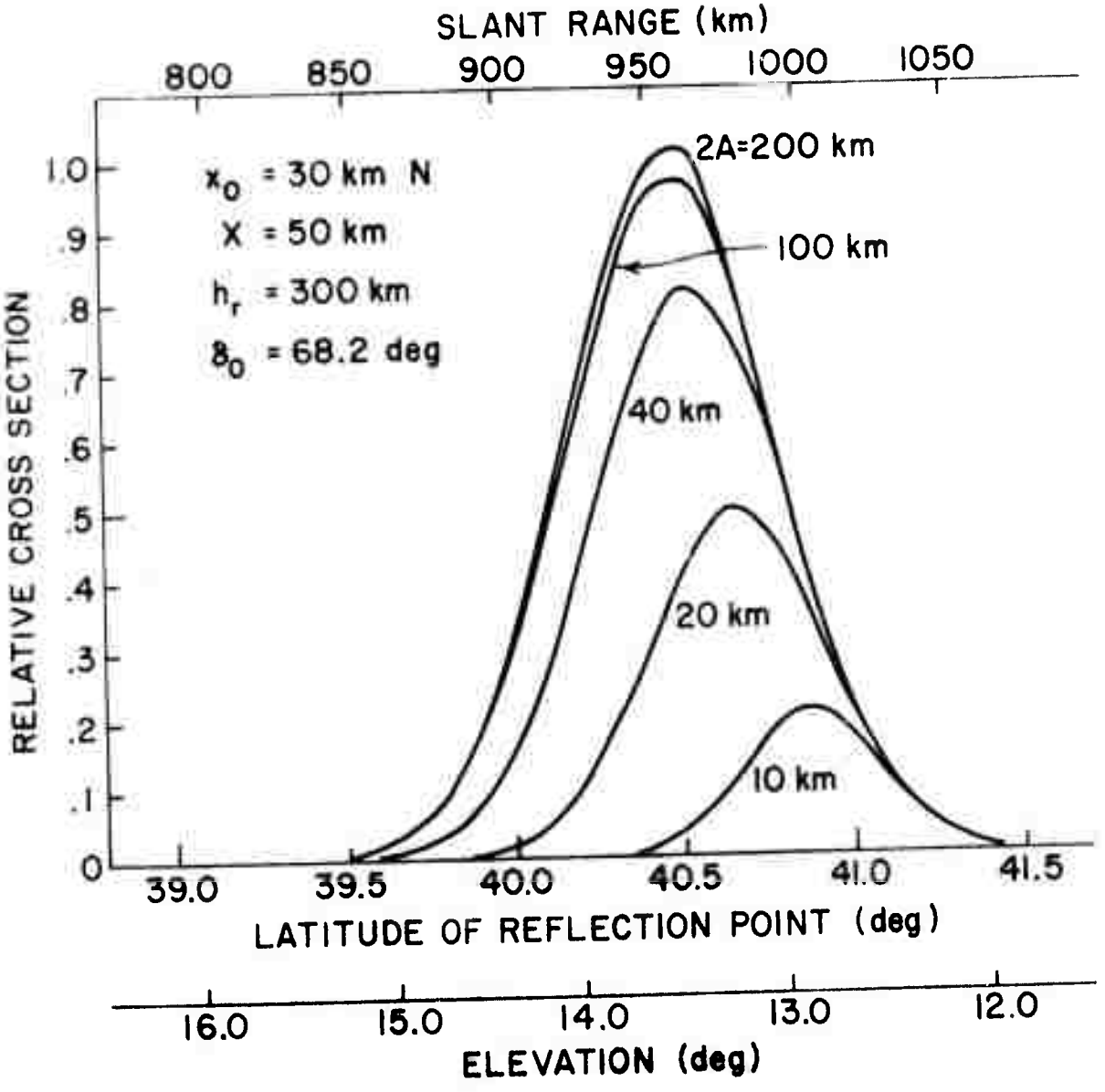

Figure 9.4

Relative cross section vs slant range and elevation for various values of 2A with X = 50 and h_r = 300 (U)

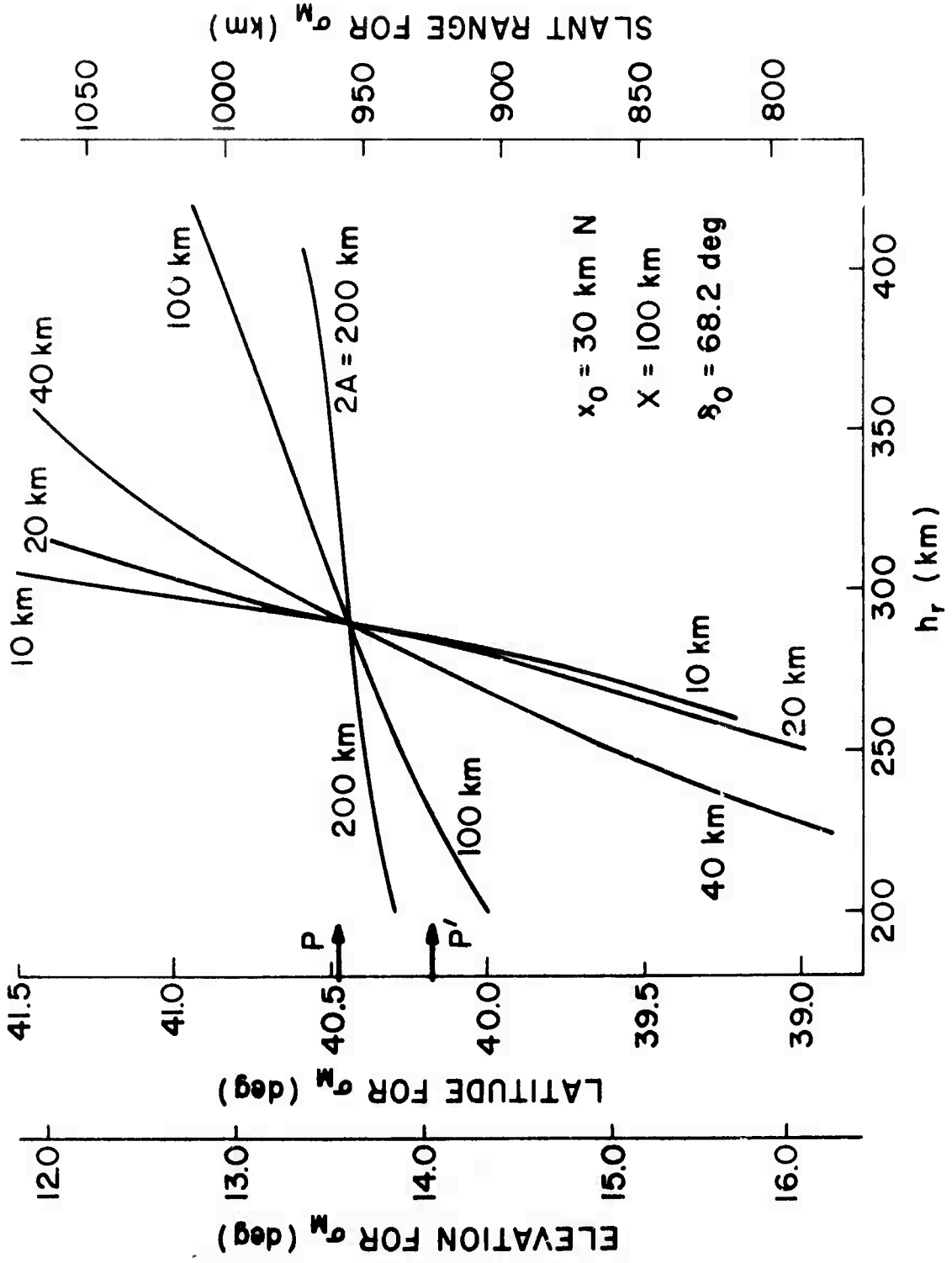

Figure 9.5

Changes in slant range and elevation for maximum cross section vs h_r for various values of 2A (U)

example, for 2A = 20 km, the h_r must lie between 260 and 310 km to avoid more than 20 dB loss relative to the optimum cross section. Varying the dip angle δ_0 changes the magnetic aspect, as does changing the northern offset x_0 of the most intense part of the heated region. These effects have been shown by additional horizontal axes for h_r corresponding to two values of δ_0 and x_0. A similar set of curves is shown in Figure 9.6 for 50 km radius; interestingly, only the thinner regions are affected.

(S) The slant ranges of the greatest cross section σ_m are shown on Figures 9.7 and 9.8. It is interesting to note that the thicker the region, the smaller the effect of heater reflection height on the range where the greatest cross section occurs. This is probably the most sensitive way to determine the value of A.

(S) The combined effects of magnetic-field geometry and heated-region offset can be represented by the following equation for the reflection height of the heating wave to give the greatest scattering cross section at White Sands:

$$h_r = 285.6 - 17.1(\delta_0 - 68.2) - .137\, x_0 \,. \qquad (9.14)$$

(S) The thickness of the heated region is probably sufficiently small that one may neglect the fact that its thin dimension is along the magnetic field axis rather than in the vertical direction. This is not the case, however, with the ASF treated in Section 11.

9.4 Additional Work Needed on this Model (U)

(S) The following procedure is suggested as a means of arriving at the ranges of values of the parameters δ_0, A, X and x_0. The reference dip δ_0 can be determined at VHF and UHF from the range-elevation diagram of the White Sands

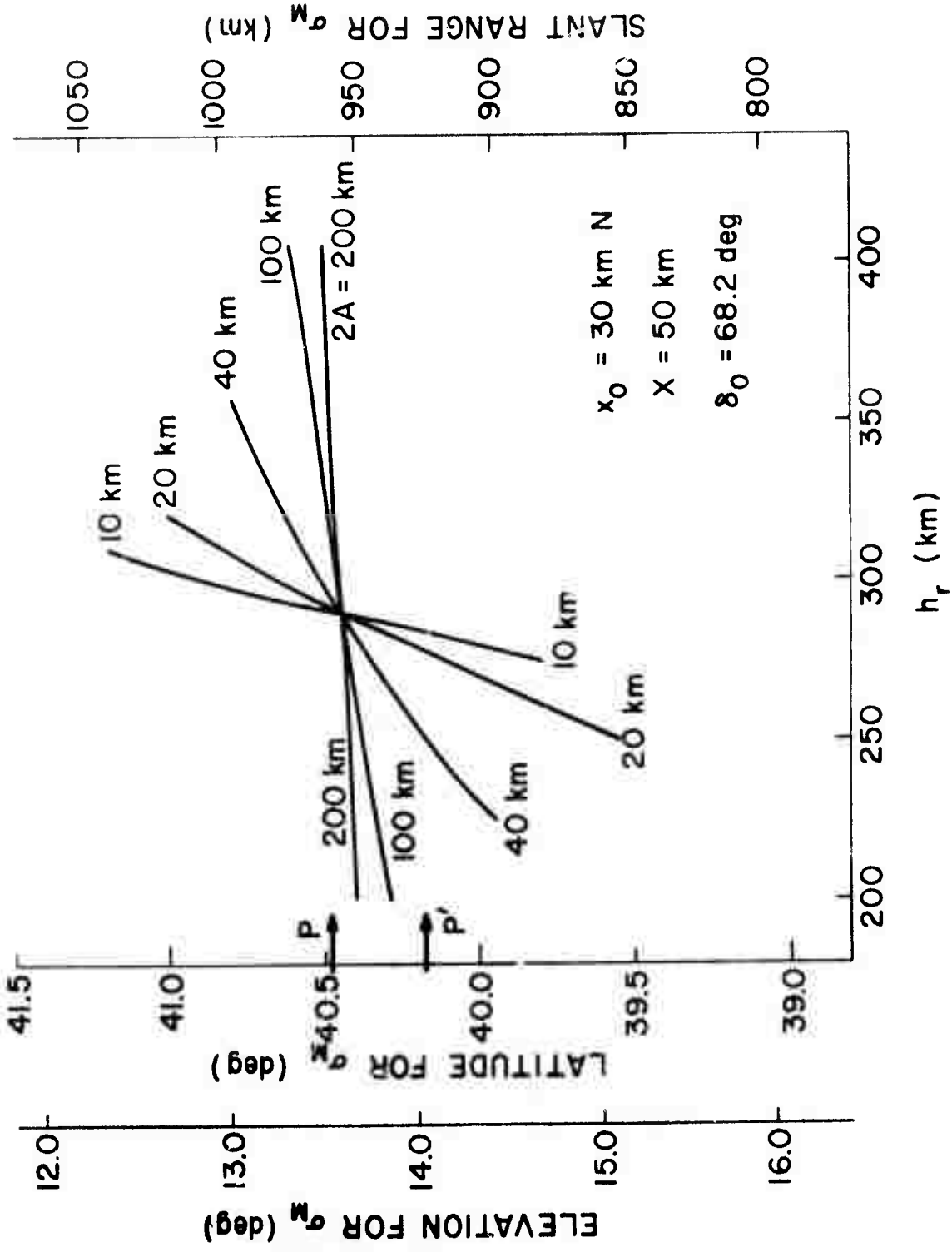

Figure 9.6

Changes in slant range and elevation for maximum cross section vs h_r for various values of 2A (U)

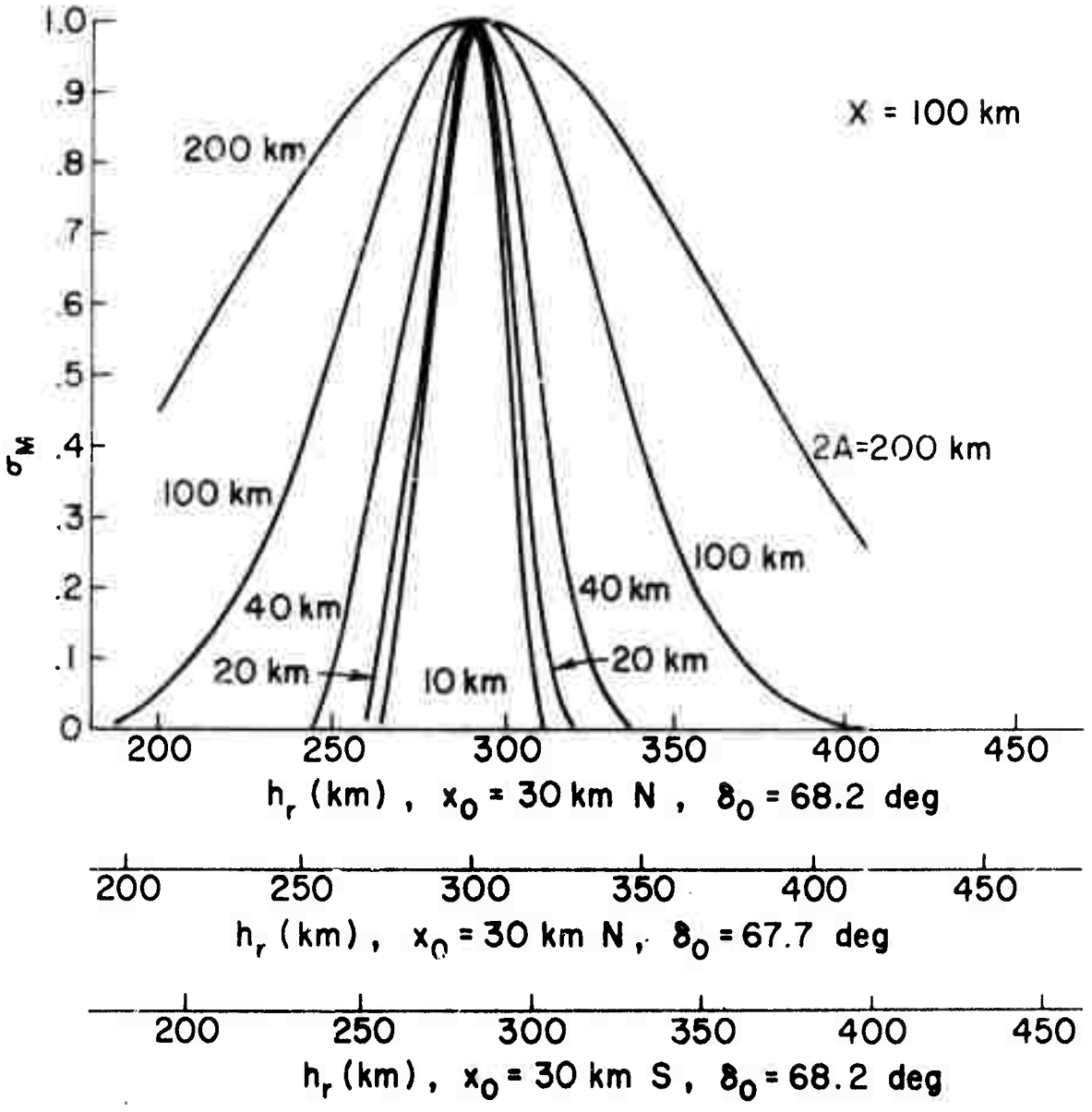

Figure 9.7

Relative value of the maximum cross section vs h_r for various values of X_0 and δ_0 with X = 100 (U)

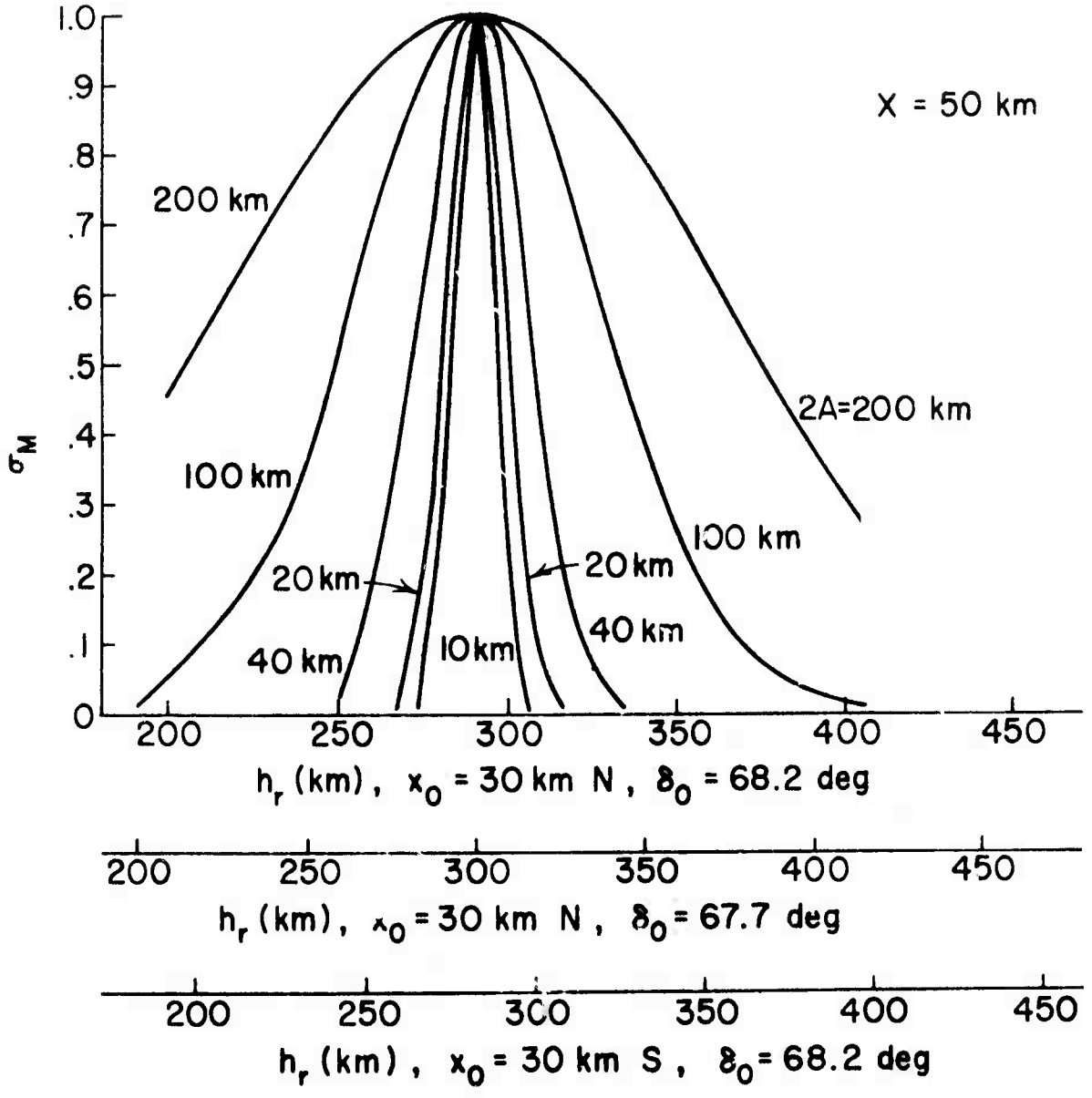

Figure 9.8

Relative value of the maximum cross section vs h_r for various values of X_0 and δ_0 with X = 50 (U)

radar. This capability is not available at frequencies lower than 150 MHz, fortunately, it may be assumed that exactly the same δ_0 applies at these frequencies. The range of δ_0 needs to be established as it is important to know, for application purposes, the extent to which aspect variability is attributable to natural causes such as magnetic field variations.

(S) The next problem is the determination of the semithickness A. If the height h_r of reflection is known, the easiest way to determine this is from plots such as Figures 9.5, 9.6, 9.7, and 9.8. However, the height of reflection h_r depends on the angle of incidence, and therefore should be determined by ray tracing for each individual profile if a precise h_r is to be known. This may present some difficulty as it is not clear that horizontal stratification can be assumed. The quantity X can also be determined in the course of this comparison.

(S) It seems that plasma-line observations, when available, might be a useful diagnostic for the variation of h_r with latitude and also for determining the north-south offset x_0. Some attempt has been made to use the published material on White Sands monostatic observations to compare with the predictions of the previous section. However, there is a dearth of accurately-calibrated A-scope or elevation scans. To make meaningful comparisons, these scans should be accompanied by values of h_r and by accurately calibrated ranges. Given a good selection of such scans (including times when only a very small return was seen) will enable the parameters of the model to be evaluated with confidence.

9.5 Bistatic Observations (U)

(S) Attention needs to be given to the question of evaluating the cross section for bistatic propagation between two sites at different azimuths from the

heated region. The straightforward Booker formula does not apply under these conditions. It is presumably a simple wavelength equivalence in that the spatial wavelength producing bistatic scatter is $\lambda/2 \cos(\phi/2)$, where ϕ is the azimuthal angle of the scatter around the magnetic-field axis. Therefore, the cross sections appropriate to such bistatic scatter would be appropriate from monostatic scatter at a frequency cos $(\phi/2)$ times the frequency used. The details of this relationship should be an integral part of the scattering model.

10. EVALUATION OF SMALL-STRUCTURE MODEL PARAMETERS (U)

(S) As an example of the type of analysis discussed in Section 9.4, the predictions of the simple model were compared with data provided by Dr. P. Fialer of SRI. Using a mean latitude of 34.4 deg for the SRI site, and assuming monostatic operation, the curves shown in Figures 10.1 through 10.4 were generated showing the relative cross section per unit area for heater reflection heights of 230, 235, 240, and 245 km. The optimum height of reflection is about 225 km for a magnetic field model with a dip of 68.2 deg over Platteville, and all the heights calculated are above that altitude. Therefore, the observed returns are towards the northward side of the heated region, resulting in a slant range for the greatest cross section that increases with altitude of heater reflection. Curves are shown for a range of values for the thickness 2A of the heated region.

(S) Two techniques were used to deduce the quantity A. In the first of these, the range extent of the VHF scattered signal for a given height of reflection was matched against the appropriate curve from Figures 10.1-10.4. Lacking quantitative data, the 10-dB points on the cross section curves were assumed to delimit the range extent of the observed echo. In fact, a detailed comparison with the A-scope curve would give much more meaningful results.

(S) One example presented by Dr. Fialer is as follows:

Time (GMT)	Range Spread	Relative Range of Peak Cross Seccion	Heater Reflection Height
0314 May 12	131 km	0	235 km
0338	104	20 km	246

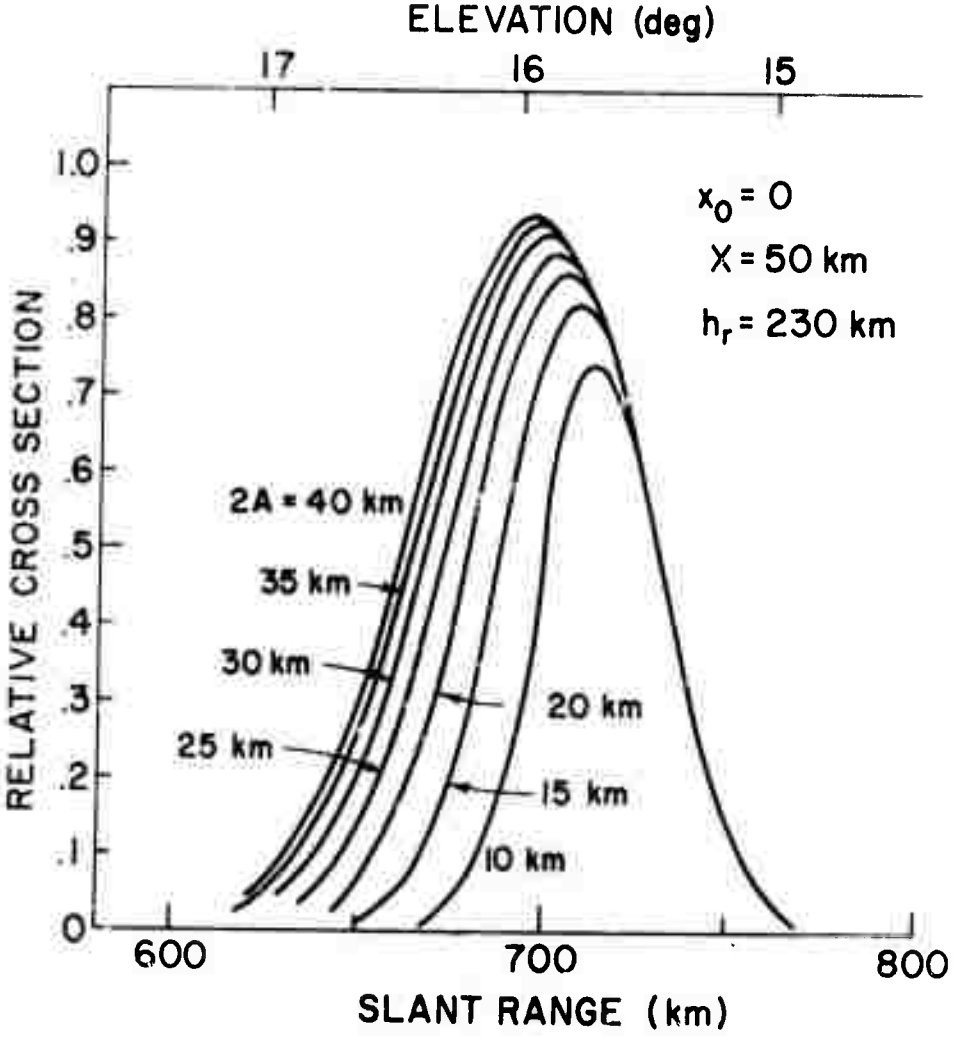

Figure 10.1

Relative cross section vs slant range or elevation showing the effect of 2A for h_r = 230 (U)

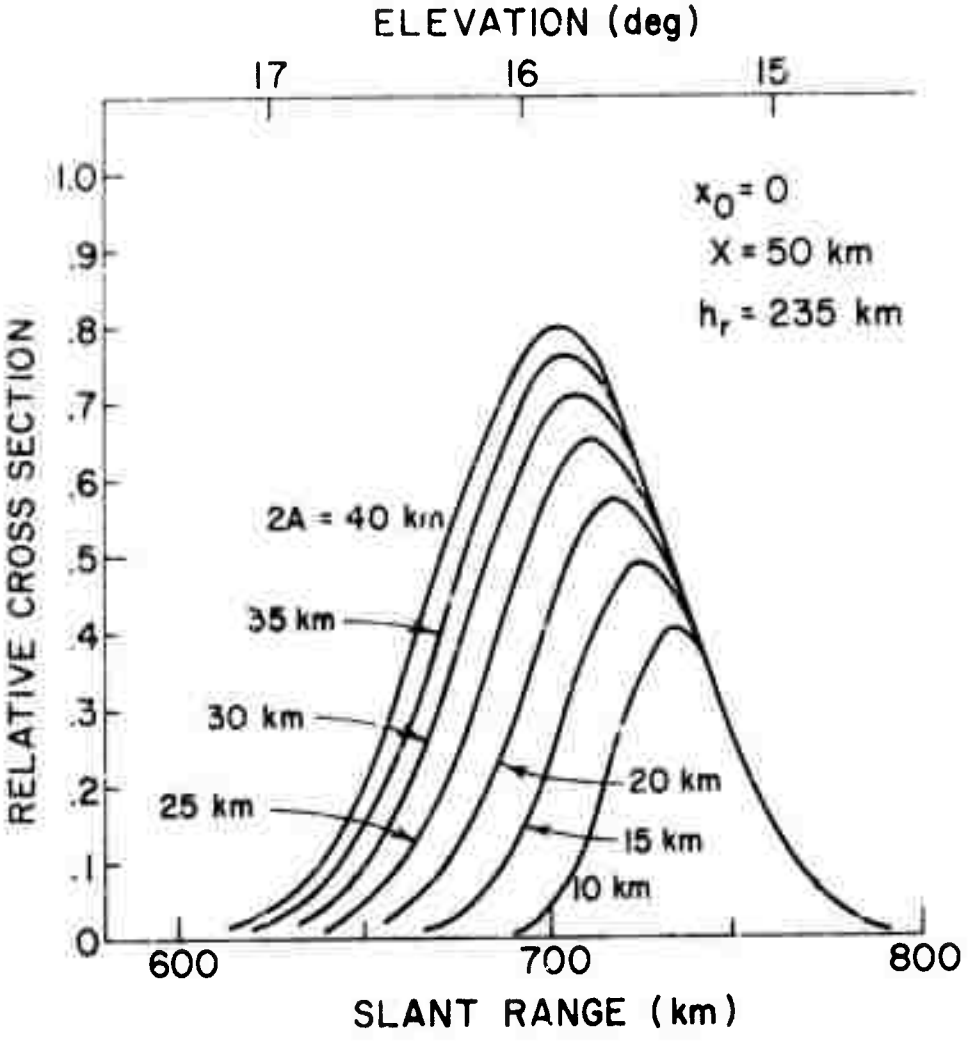

Figure 10.2

Relative cross section vs slant range or elevation showing the effect of 2A for h_r = 235 (U)

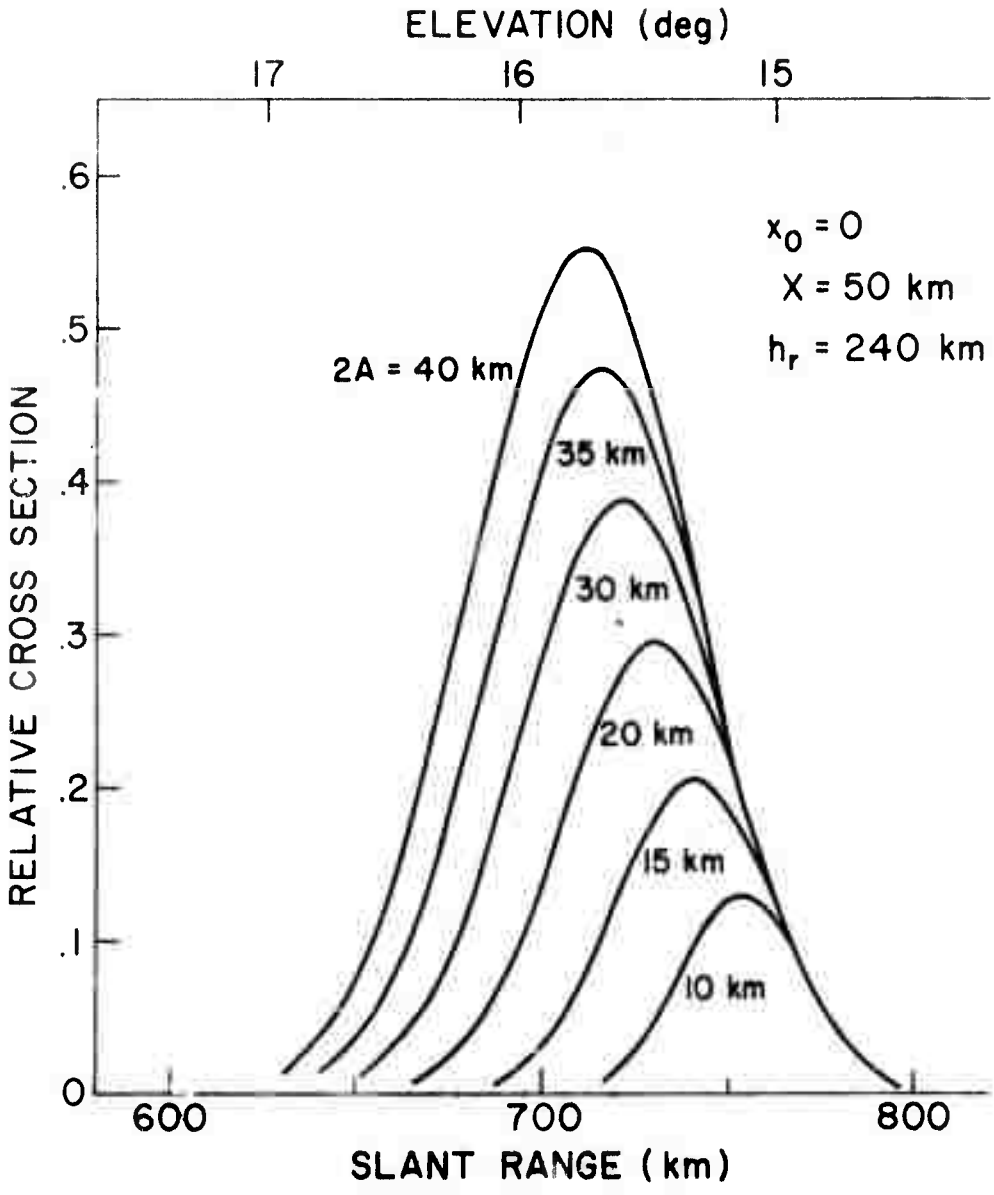

Figure 10.3

Relative cross section vs slant range or elevation showing the effect of 2A for h_r = 240 (U)

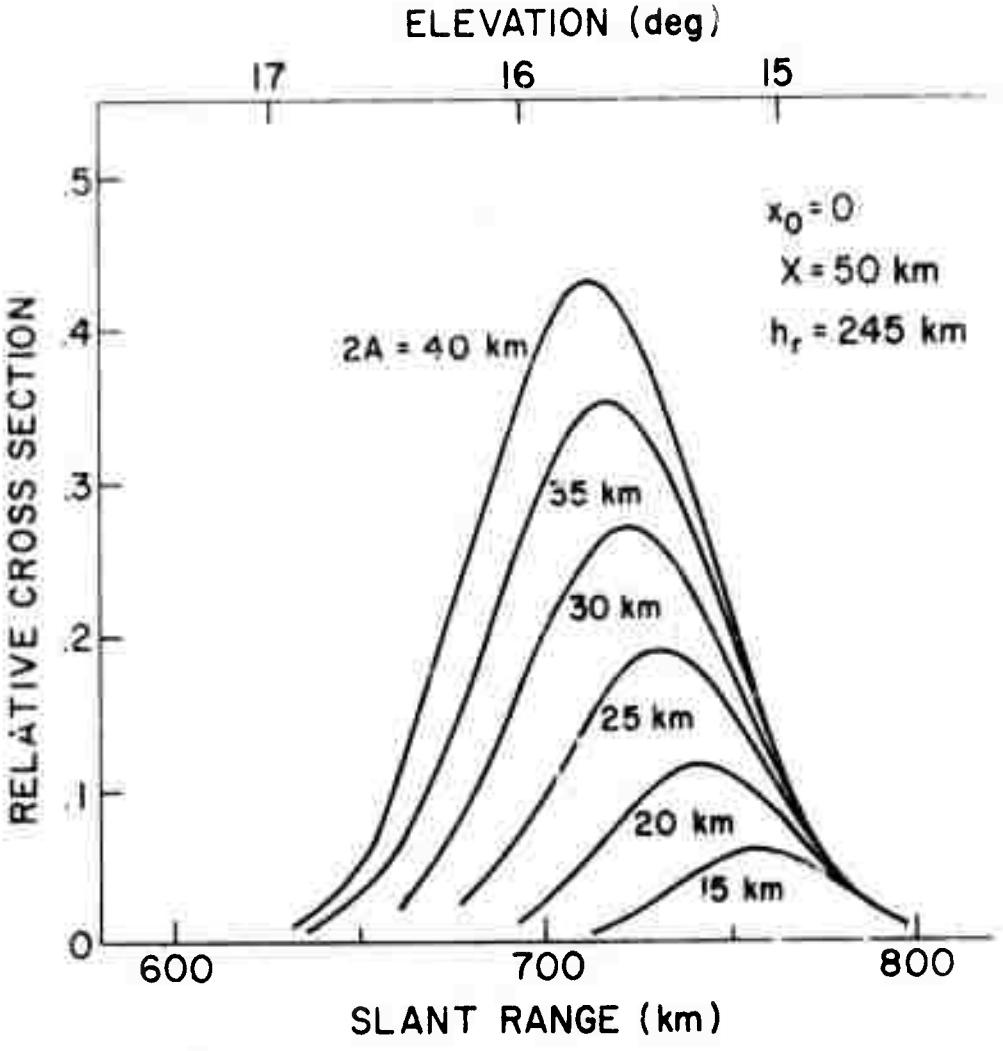

Figure 10.4

Relative cross section vs slant range or elevation showing the effect of 2A for h_r = 245 (U)

Using Figures 10.2 and 10.4, the range spreads for these two times correspond to values for 2A of 35 and 20 km, respectively.

(S) The parameter 2A was then redetermined from the change in range of the maximum cross section. Figure 10.5 shows how this range depends on heater reflection height h_r for $x_0 = 0$ (i.e., disturbed region centered over Platteville and with 50 km for X (the e-folding horizontal radius of the heated region). Interpolation from this curve shows that a 20-km increase in slant range would accompany an 11-km increase in heater reflection heights for a value of 26 km for 2A. It is felt that this result is in reasonable agreement with that deduced by the first method.

(S) A note of caution needs to be sounded concerning the assumptions made in this model. The rapidity with which the range of maximum cross section varies with heater reflection height depends on the slope of the heater antenna pattern (on its northern edge, in this case). This in turn depends on the assumed value for X. As an example, Figure 10.6 (for X = 100 km) shows substantially increased slopes from the corresponding curve of Figure 10.5. The assumption of a heater volume centered north of Platteville ($x_0 = 30$) is illustrated in Figure 10.7. Its principal effect is to displace the curves of Figure 10.5 to greater ranges and greater reflection heights without affecting their slopes.

(S) No doubt, a detailed comparison of these curves with experimental data will permit the evaluation of all three of the parameters A, X, x_0. However, present indications are that the scattering region at VHF may be only 20 km thick, implying critical geometry for any bistatic experiment.

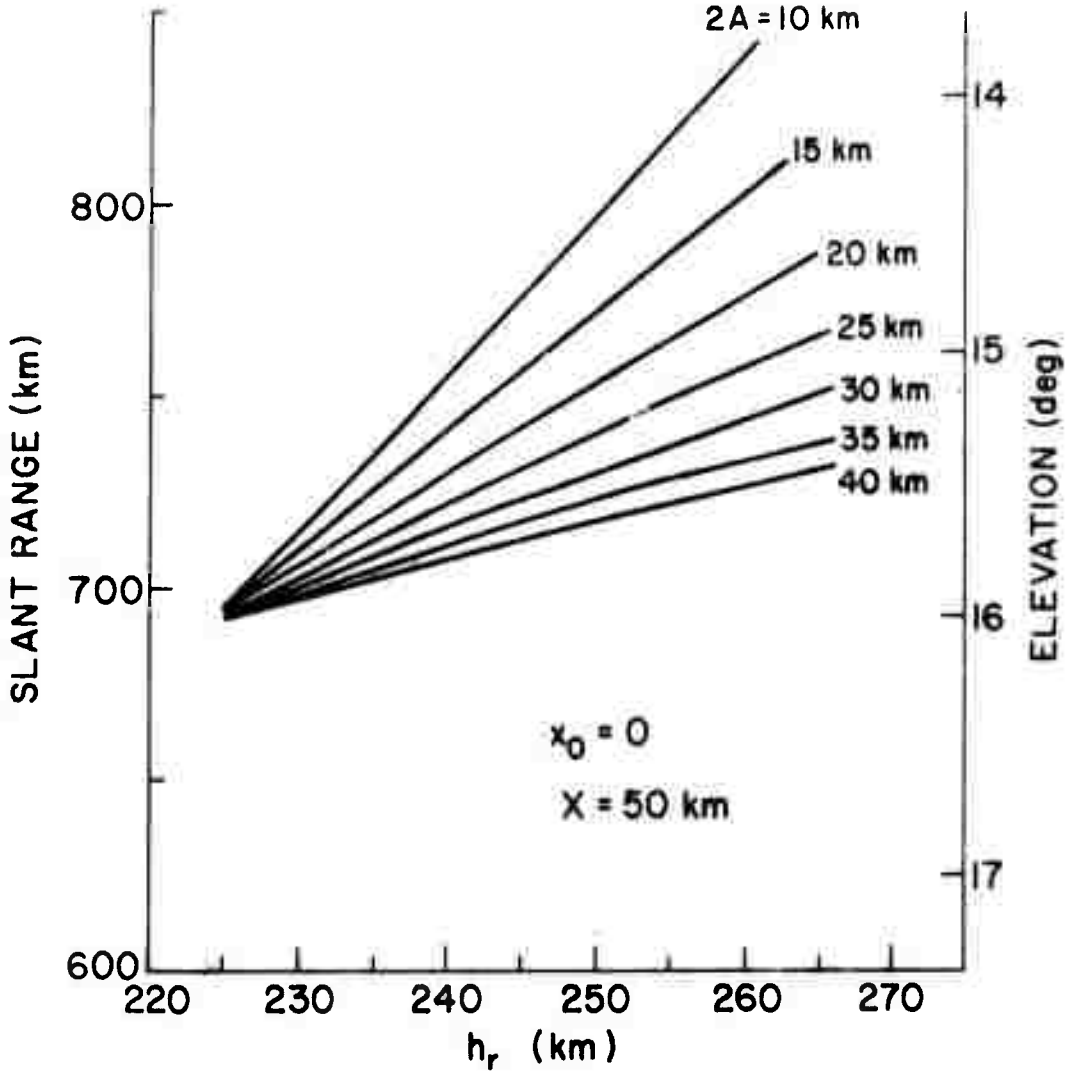

Figure 10.5

Slant range or elevation for maximum cross section vs h_r showing the effect of 2A for $x_0 = 0$ and X = 50 (U)

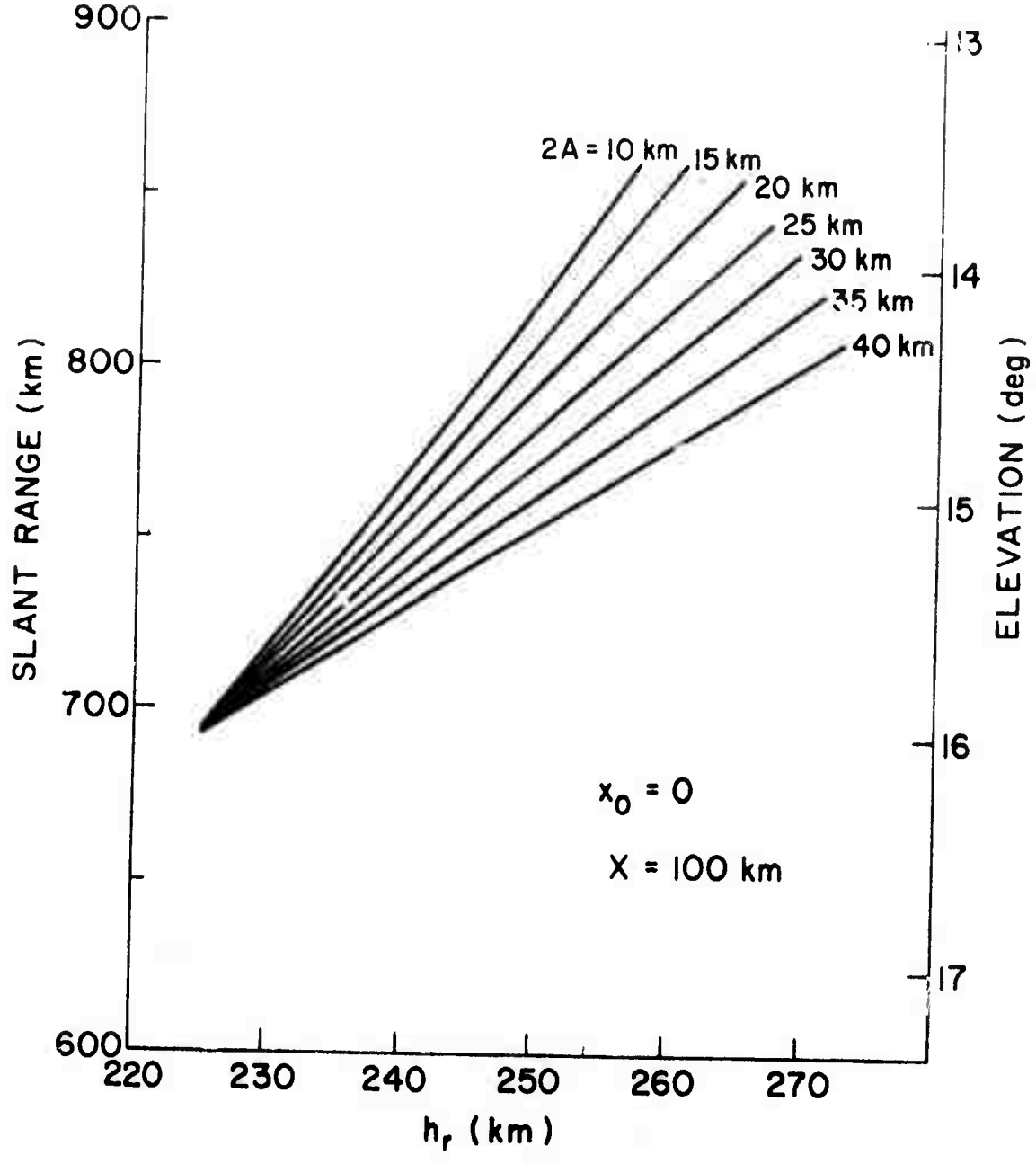

Figure 10.6

Slant range or elevation for maximum cross section vs h_r showing the effect of 2A for x_0 = 0 and X = 100 (U)

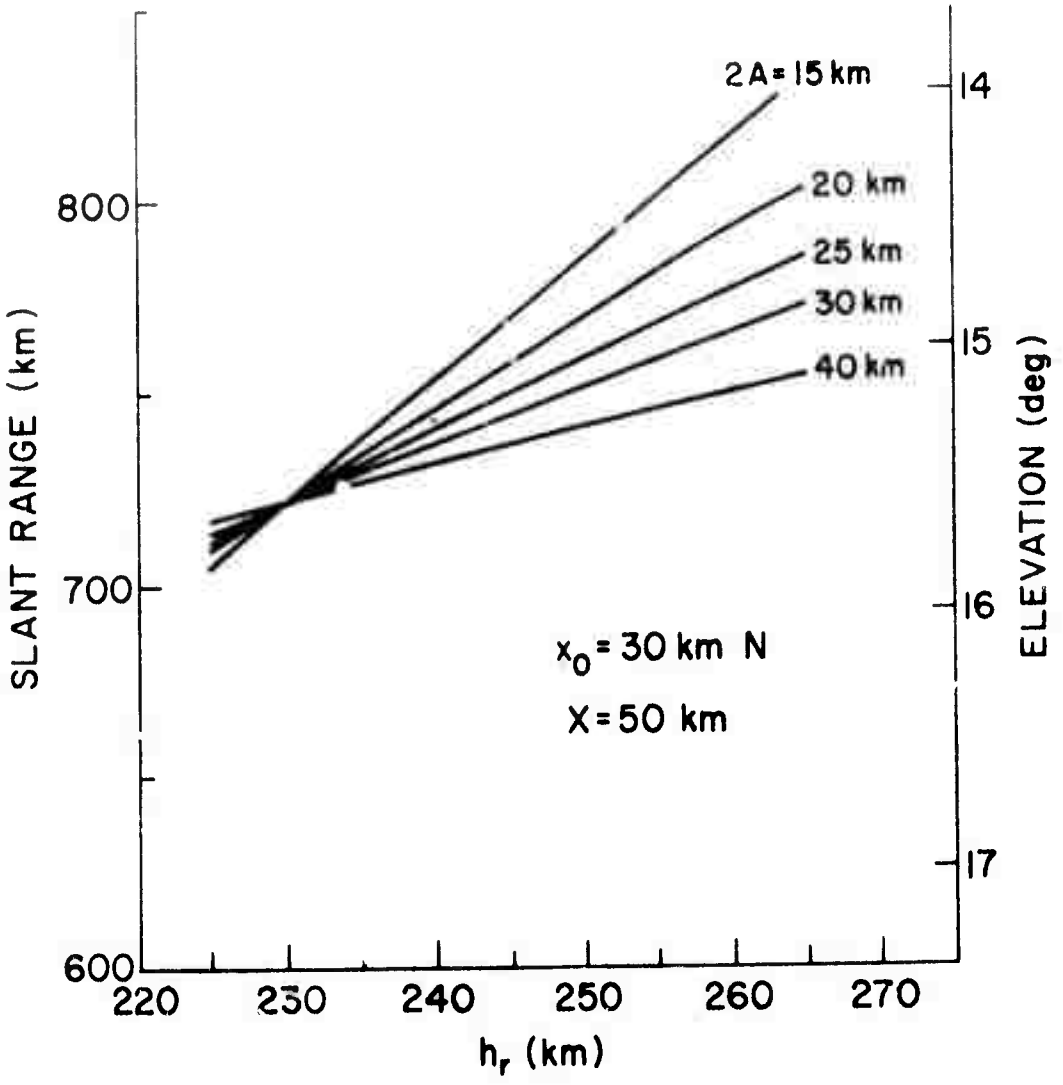

Figure 10.7

Slant range or elevation for maximum cross section vs h_r showing the effect of 2A for x_0 = 30 and X = 50 (U)

11. LARGER-STRUCTURE MODEL (U)

(S) The second part of this model involves the interpretation of satellite scintillation data which are affected by artificial spread F (ASF) at heights above 180 km. Because these irregularities appear to extend throughout the F region, the height extent of the irregularities is larger than the horizontal extent of the disturbed region. Therefore, the disturbed region must be considered as a cylinder tilted at an angle δ to the horizontal. At a given altitude, its latitude variability is as shown in Equation 9.13; however, its height variation seems most readily interpreted as being due to a constant percentage fluctuation in electron density at all altitudes. The rms phase fluctuation γ is given in Section 5 as

$$\gamma^2 = \frac{\pi^{5/2}}{\lambda^2} \left(\frac{foF2}{f}\right)^4 \left(\frac{\overline{\Delta N}}{N}\right)^2 D \sec i \operatorname{cosec} \psi \int (N/N_m)^2 \, dh \qquad (5.4)$$

on the assumption that the fractional rms electron-density fluctuation is independent of altitude. The rms amplitude fluctuation ε is given by

$$\varepsilon = \gamma/\sqrt{2} \quad . \qquad (5.5)$$

The rms fractional fluctuation in electron density was found in Section 5 to be about 6.9×10^{-3}.

(S) A detailed comparison of the rms amplitude fluctuation of Figure 5.5 through the satellite pass with the satellite orbital parameters suggests the form shown in Figure 11.1 for the intersection of the satellite line of sight with the e-folding contour of the fractional electron-density fluctuation. This corresponds to a cylinder of radius 50 km whose axis passes through

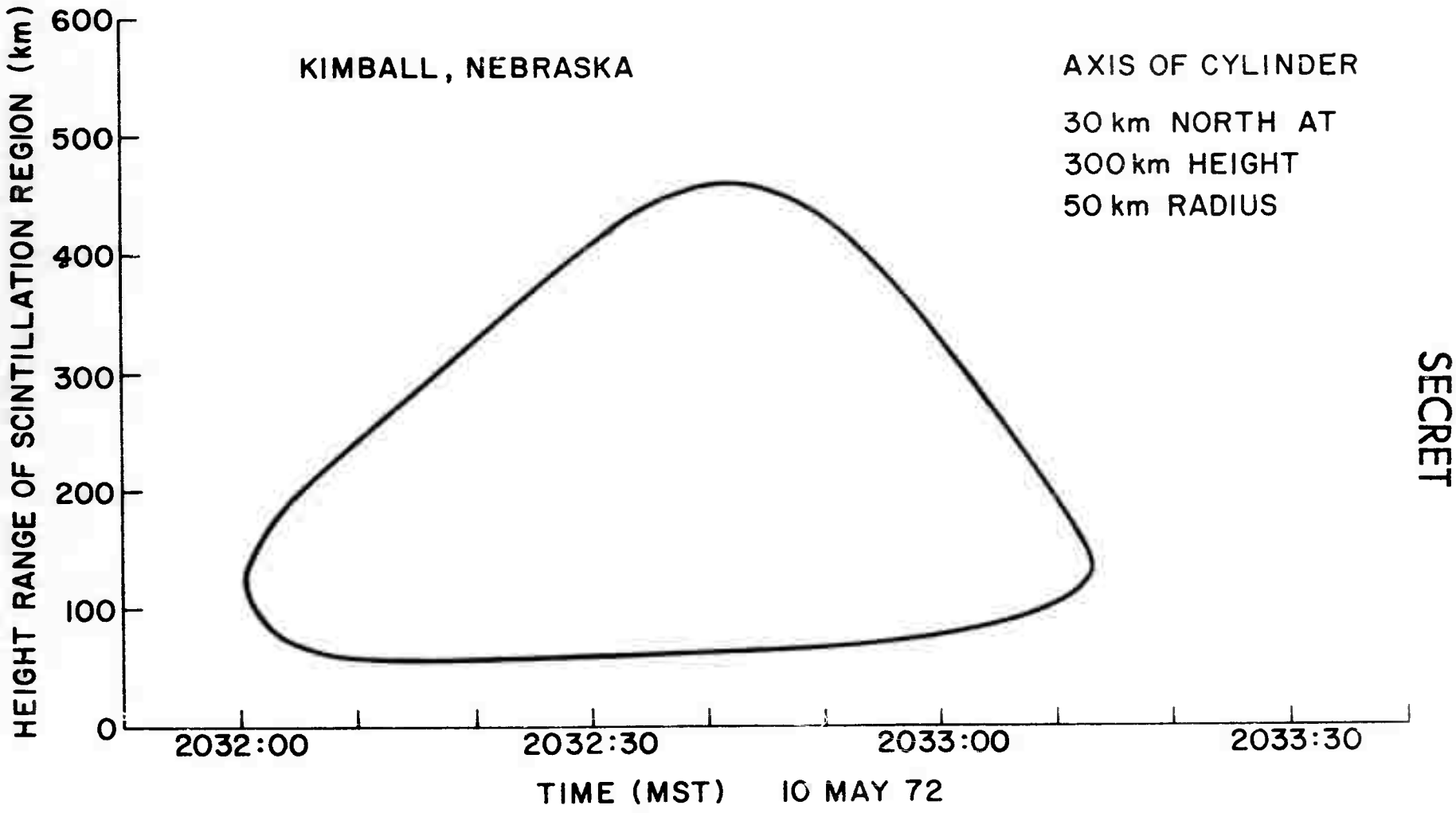

Figure 11.1

Range of heights within the region of interest for a satellite pass observed from Kimball, Nebraska during Prairie Smoke II (U)

the 300-km level at 30 km north of Platteville, and seems a useful nominal model.

(S) Accordingly, it is recommended that Equations (5.4) and (5.5) should be used to determine the amplitude fluctuation expected, using the following form for the fractional electron-density fluctuation:

$$\overline{(\Delta N/N)^2} = \overline{(\Delta N/N)_0^2} \exp \{[-(x-x_0)^2 - y^2]/X^2\} \qquad (11.1)$$

where x and y are distances measured in the northward and westward direction, respectively, from the magnetic field line passing above Platteville at 300-km altitude, and the parameters have the following values:

$$\overline{(\Delta N/N)_0^2} = 6.9 \times 10^{-6}$$

$$x_0 = 30 \text{ km}$$

$$X = 50 \text{ km}$$

(S) Fluctuations in angle of arrival of the transmitted wave may be expected to have a magnitude of about

$$\lambda\gamma/2\sqrt{2}\,\pi\,D \quad . \qquad (11.2)$$

12. GEOMETRY AND CROSS SECTIONS FOR BISTATIC SCATTER

12.1 The Bistatic-Geometry Problem

Consider a set of magnetic coordinates such that the latitude and longitude of P are λ_p and 0, respectively. Consider propagation from a point 1, on the earth's surface, to a point 0 at height h_0, and thence to a point 2 on the earth's surface. Let δ_0 be the magnetic dip at the point 0. Let the latitudes and longitudes at points 0, 1, and 2 be denoted by λ and ϕ with the appropriate suffix.

Consider now a set of Cartesian coordinates with the z axis at the N magnetic pole, and the (x, z) plane the meridian through P. The Cartesian coordinates of the points are:

$$x_1 = R_0 \cos \lambda_1 \cos \phi_1$$

$$y_1 = R_0 \cos \lambda_1 \sin \phi_1$$

$$z_1 = R_0 \sin \lambda_1$$

$$x_2 = R_0 \cos \lambda_2 \cos \phi_2$$

$$y_2 = R_0 \cos \lambda_2 \sin \phi_2$$

$$z_2 = R_0 \sin \lambda_2$$

$$x_0 = (R_0 + h_0) \cos \lambda_0 \cos \phi_0$$

$$y_0 = (R_0 + h_0) \cos \lambda_0 \sin \phi_0$$

$$z_0 = (R_0 + h_0) \sin \lambda_0$$

where R_0 is the radius of the earth.

The magnetic-field direction at the point 0 is defined by the unit vector

$$\hat{B} = [\sin(\delta_0 + \lambda_0),\ 0,\ -\cos(\delta_0 + \lambda_0)] .$$

The vector $\tilde{r}_{10}$ joining the points 1 and 0 has the value

$$\tilde{r}_{10} = [x_0 - x_1,\ y_0 - y_1,\ z_0 - z_1] .$$

Now if θ_1 is the angle between $\tilde{r}_{10}$ and $\hat{B}$ at the point 0,

$$R_1 \cos\theta_1 = \tilde{r}_{10} \cdot \hat{B}$$

$$= (x_0 - x_1)\sin(\delta_0 + \lambda_0) - (z_0 - z_1\cos(\delta_0 + \lambda_0))$$

where $R_1 = |\tilde{r}_{10}|$ = slant range of 0 from 1.

Similarly, the angle θ_2 between $\tilde{r}_{20}$ and $\hat{B}$ is

$$R_2 \cos\theta_2 = (x_0 - x_2\sin(\delta_0 + \lambda_0) - (z_0 - z_1)\cos(\delta_0 + \lambda_0) .$$

For specularity,

$$\theta_1 = 180° - \theta_2 \qquad\qquad \cos\theta_1 = -\cos\theta_2 .$$

Therefore,

$$\frac{x_0 - x_1}{R_1}\sin(\delta_0 + \lambda_0) - \frac{z_0 - z_1}{R_1}\cos(\delta_0 + \lambda_0)$$

$$+ \frac{x_0 - x_2}{R_2} \sin(\delta_0 + \lambda_0) - \frac{z_0 - z_2}{R_2} \cos(\delta_0 + \lambda_0) = 0 .$$

$$x_0 \sin(\delta_0 + \lambda_0) \left[\frac{1}{R_1} + \frac{1}{R_2}\right] - z_0 \cos(\delta_0 + \lambda_0) \left[\frac{1}{R_1} + \frac{1}{R_2}\right]$$

$$+ \sin(\delta_0 + \lambda_0) \left[-\frac{x_1}{R_1} - \frac{x_2}{R_2}\right] + \cos(\delta_0 + \lambda_0) \left[\frac{z_1}{R_1} + \frac{z_2}{R_2}\right] = 0.$$

Substituting for x_0 and z_0, the first line becomes

$$(R_0 + h_0) \left(\frac{1}{R_1} + \frac{1}{R_2}\right) \left[\cos \lambda_0 \cos \phi_0 \sin(\delta_0 + \lambda_0) - \sin \lambda_0 \cos(\delta_0 + \lambda_0)\right]$$

and since $\phi_0 < 1$ degree, $\cos \phi_0 \sim 1$ and this becomes

$$(R_0 + h_0) \left(\frac{1}{R_1} + \frac{1}{R_2}\right) \sin \delta_0 = \cos(\delta_0 + \lambda_0) \left(\frac{z_1}{R_1} + \frac{z_2}{R_2}\right)$$

$$- \sin(\delta_0 + \lambda_0) \left(\frac{x_1}{R_1} + \frac{x_2}{R_2}\right) ,$$

from which $(R_0 + h_0)$ may be found. The difficulty of not knowing R_1 and R_2 disappears, incidentally, if $R_1 = R_2$. Then the equation becomes:

$$2(R_0 + h_0) \sin \delta_0 = z_1 + z_2) \cos(\delta_0 + \lambda_0)$$

$$- (x_1 + x_2) \sin(\delta_0 + \lambda_0) .$$

The suggested procedure is as follows:

(1) Identify points 1 and 2.

(2) For a point 300 km over P, find R_1 and R_2.

(3) Solve the above equations for h_0 for P as point 0. If h_0 is not about 300 km, points 1 and 2 are wrongly located for successful bistatic propagation. Relocate them.

(4) Find h_0 for a given point 0; recalculate R_1 and R_2 and repeat.

(5) Choose three points 0 arranged around P, and fit an h_Q surface as outlined in the following section.

12.2 Suggested Procedure for Bistatic Calculation of h_Q (Orthogonality) Surface

Refer to Figure 12.1. Select three points, A, B, and C, at the corners of the equilateral triangle centered on Platteville (P) with its apex to the north, and with sides of 70 km. For each point, calculate h_Q using the formula (for point A):

$$1 + \frac{h_{A'}}{R_0} = \frac{R_2}{R_1 + R_2} \frac{\sin(\lambda_1 - \lambda_{A'} - \delta_{A'})}{\sin \delta_{A'}} + \frac{R_1}{R_1 + R_2} \frac{\sin(\lambda_2 - \lambda_{A'} - \delta_{A'})}{\sin \delta_{A'}}$$

where suffixes 1, 2, and A′ refer to the transmitting and receiving sites, and to the point on the h_Q surface above A, respectively; R_0 is the earth radius; R_1 and R_2 are the ranges from 1 and 2 to A′; $\delta_{A'}$ is the magnetic dip at A′; and λ is latitude in magnetic coordinates.

Fit a plane through the points A′, B′, and C′ and take this as defining the h_Q surface in the region of interest.

12.3 Bistatic-Cross-Section Calculation

Adopt the coordinate system shown in Figure 12.2.

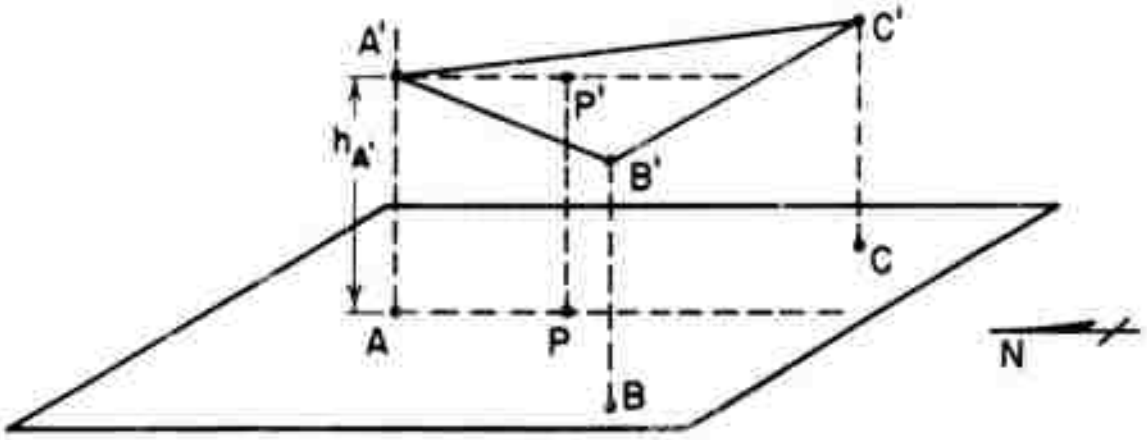

Figure 12.1

Orthogonality-surface geometry

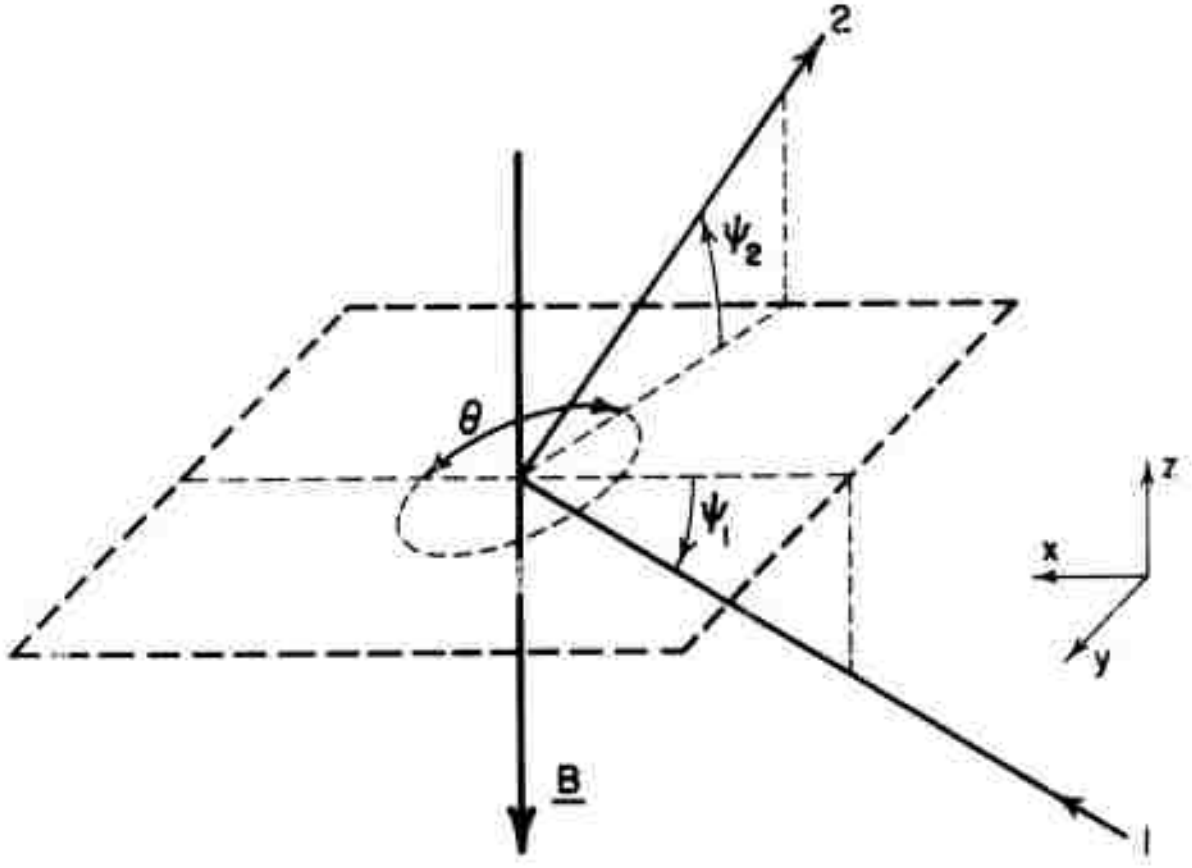

Figure 12.2

Bistatic geometry

Then the direction cosines (l_1, m_1, n_1) ard (l_2, m_2, n_2) for the two rays 1 and 2 are:

$$l_1 = \cos \Psi_1 \qquad l_2 = \cos \Psi_2 \cos \theta$$

$$m_1 = 0 \qquad m_2 = -\cos \Psi_2 \sin \theta$$

$$n_1 = \sin \Psi_1 \qquad n_2 = \sin \Psi_2 \ .$$

Let the correlation function be given by

$$P(x,y,z) = e^{-\frac{x^2}{2T^2} - \frac{y^2}{2T^2} - \frac{z^2}{2L^2}}$$

and the spatial spectrum by

$$P(l,m,n,) = (2\pi)^{3/2} T^2 L \, e^{-\frac{T^2 l^2}{2} - \frac{T^2 m^2}{2} - \frac{L^2 n^2}{2}} \ .$$

Booker gives the scattering cross section as

$$\sigma_v = \overline{\left(\frac{\Delta\epsilon}{\epsilon}\right)^2} \frac{\pi^2 \sin^2 \chi}{\lambda^4} P\{k(l_2 - l_1), k(m_2 - m_1), k(n_2 - n_1)\}$$

where χ is the angle between the electric vector of the incident wave and the direction of the scattered wave 2. Putting

$$\overline{\left(\frac{\Delta\epsilon}{\epsilon}\right)^2} = \left(\frac{\lambda}{\lambda_N}\right)^4 \overline{\left(\frac{\Delta N}{N}\right)^2} \ ,$$

the cross section is:

$$\sigma_v = \frac{(2\pi)^{3/2}\pi^2 \sin^2\chi}{\lambda_N^4} \overline{\left(\frac{\Delta N}{N}\right)^2} T^2 L \, e^{-(1/2)k^2T^2[(l_2-l_1)^2 + (m_2-m_1)^2] - (1/2)k^2L^2(n_2-n_1)^2}.$$

Let s be the distance measured along the magnetic field from the specular point. Then

$$n_1 = \sin\Psi + s\cos^2\Psi/R_1$$

$$n_2 = \sin\Psi - s\cos^2\Psi/R_2$$

where R_1 and R_2 are the slant ranges for rays 1 and 2, and Ψ is the specular angle between the wave normals and a plane normal to the field. Putting

$$n_2 - n_1 = s\cos^2\Psi(R_1^{-1} + R_2^{-1})$$

in the cross section and integrating with respect to s, the cross section per unit area normal to the field becomes:

$$\sigma_A = \int \sigma_v ds = \frac{(2\pi)^{3/2}\pi^2 \sin^2\chi}{\lambda_N^4} \overline{\left(\frac{\Delta N}{N}\right)^2} T^2 L \, e^{-(1/2)k^2T^2[(l_2-l_1)^2 + (m_2-m_1)^2]}$$

$$\int e^{-(1/2)k^2L^2s^2\cos^4\Psi(1^{-1} + R_2^{-1})^2} ds$$

$$\sigma_A = \frac{4\pi^4 \sin^2\chi \, T^2 \overline{\left(\frac{\Delta N}{N}\right)^2}}{\lambda_N^4 k \cos^2\Psi(R_1^{-1} + R_2^{-1})} e^{-2k^2T^2\cos^2\Psi\sin^2(\theta/2)}.$$

Finally, per unit area of horizontal area is given by:

$$\sigma_{AH} = \frac{4\pi^4 \sin^2 \chi \cos \delta}{\lambda_N^4 k \cos^2\psi (R_1^{-1} + R_2^{-1})} \overline{\left(\frac{\Delta N}{N}\right)^2} T^2 e^{-2K^2T^2 \cos^2 \psi \sin^2(\theta/2)} .$$

For a medium containing more than one scale T, the terms from

$$\overline{\left(\frac{\Delta N}{N}\right)^2}$$

onward are replaced by:

$$\overline{\left(\frac{\Delta N}{N}\right)^2}_1 T_1^2 e^{-2k^2T_1^2\cos^2\psi\sin^2(\theta/2)} + \left(\frac{\Delta N}{N}\right)^2_2 T_2^2 e^{-2k^2T_2^2\cos^2\psi\sin^2(\theta/2)}$$

where δ = magnetic dip.

12.4 Carrying Out the Integration

Consider a coordinate system (x,y,z) centered at Platteville. A suitable grid of points in the (x,y) plane is selected, and the geometrical specular height $z = h_Q$ is calculated. Then

$$\overline{\left(\frac{\Delta N}{N}\right)^2} = \left(\frac{\Delta N}{N}\right)^2_0 e^{-(x - x_0)^2/X^2 - y^2/X^2 - (z - h_Q)^2/A^2} .$$

δ = magnetic dip at (x,y,h_Q) from field model, and $R_1, R_2, \chi, \Psi, \theta$ are calculated at (x,y,h_Q). Illumination due to antenna polar diagrams is calculated. The product is integrated over the (x,y) plane.

13. CONCLUSIONS (U)

13.1 Large-Structure Model (U)

(S) Observations of signals from geostationary and orbiting satellites at frequencies from 30 to 400 MHz have established the general behavior of the large-scale field-aligned structure (ASF) that produces scintillations of those signals. Studies have been limited to full-power ordinary-mode heating, with the heater being directed overhead, at frequencies below the F2-layer critical. The conclusions are as follows:

(S) 1. The field-aligned structure gives strong VHF and UHF scintillations up to 400 MHz.

(S) 2. The scintillation index maximizes when the direction of propagation is close to the downfield direction. Therefore, for example, heating the ionosphere upfield from a radar will produce a "blind spot" of about 10 deg radius centered on the magnetic zenith at 150 MHz frequency.

(S) 3. The fading depth of the scintillation varies inversely with frequency, as would be expected from the integrated-phase-path theory of satellite scintillations.

(S) 4. The transverse scale of the large-scale structure has a half-correlation distance of about 100 m, and convects in an east-west direction with the velocity of the ambient plasma (about 20-50 m sec^{-1}).

(S) 5. The large-scale structure extends from 200 to 450 km altitude, and is usually confined within a cylinder of about 50 km radius, with its axis the magnetic field line passing through the reflection point directly over the heater.

(S) 6. Occasionally, unusual shapes for the irregular region are seen, probably arising from a doughnut-shaped disturbed region due to burn-through

of the central core of the ionosphere above the heater.

(S) The following additional studies of large-scale structure are important:

(S) 1. *Measurements of the height distribution of the electron-density fluctuation associated with the large-scale irregularities.* Heights inferred from orbital-satellite passes seem to point to field-aligned irregularities that are distributed throughout the bottomside and topside, with a statistically constant fractional fluctuation of electron density. However, this has not been experimentally verified. A relatively simple experiment to do this will be to observe the rise or set of an orbiting satellite behind the disturbed region, as observed from a site far to the south (e.g. Albuquerque). Since the line of sight to the satellite is nearly orthogonal to the magnetic field, the altitude intercepted within the disturbed cylinder is much more nearly constant than when looking at an orbital satellite from a location to the north of the disturbed region.

(S) 2. *Detailed studies of the spatial and temporal characteristics of the correlation function of the amplitude for an orbiting satellite.* Thus, it will be possible to determine whether finer-scale structure is present on the scintillations. Adequate signal-processing instrumentation is available to make these studies as time permits.

(S) 3. *Studies of the aspect dependence of the scintillating signal close to the downfield direction.* Scattering theory predicts the way the amplitude and phase fluctuation should vary with angle from the magnetic zenith; but because of the possible significance of radar applications, this aspect of the theory needs verification.

(S) 4. *The horizontal morphology.* The factors controlling the shape of the disturbed region are not wholly understood at this time, and additional

morphological studies, perhaps with other orbiting satellites, are appropriate.

(S) 5. *Yield studies.* Most studies up to now have concentrated on formulating a scattering model appropriate to full power ordinary polarization. Attention needs to be given to the effect of reducing the power, optimizing the heater frequency, steering the heater beam and trying other forms of heater-signal modulation.

(S) 6. *Scintillation experiments at other locations.* All results thus far have been restricted to the Platteville heater installation. No ASF has been demonstrated at other locations. Therefore, it seems necessary to try a satellite scintillation experiment at Arecibo (when that heater is in operation) to see if there is any constant difference in the large-scale structure between Arecibo and Platteville. In addition, if a mobile heater facility is set up elsewhere than these two locations, satellite scintillation seems to be the appropriate diagnostic to include.

13.2 Small-Structure Model (U)

(S) In Sections 8, 9 and 10 of this report, the concept has been developed that the small-scale structure responsible for VHF and UHF backscatter is governed by the geometry of the surface of orthogonality (the h_Q surface) appropriate to the location of the radar. The intersection of this (ideally infinitely thin) surface with the disturbed region gives the location of the backscattering irregularities for that particular radar. Using a simplified magnetic field model, it was shown that the h_Q surface slopes down toward the south, and that the thickness of the disturbed region can therefore be deduced from the range spread of a backscattered echo. An illustrative example was given to show that the region thickness was about 20 km. A methodology has been indicated for the calculation of the corresponding geometry and cross sections for bistatic scatter.

(S) The following important tasks remain with the small-scale scattering model:

(S) 1. *Disturbed region thickness calculation.* The same type of calculation as shown in Section 10 of this report needs to be carried out under a wide variety of conditions, to determine the limits on the disturbed region thickness. The assumption that the scattering region at a given range is infinitely thin needs to be verified by an interferometer or other similar experiment.

(S) 2. *Bistatic geometry.* The change in total cross section with scattering angle indicated in Section 12 needs to be verified by bistatic tests.

(S) 3. *Yield studies.* Variations of the small-scale structure cross section and morphology with frequency and reflection height and heater power need to be evaluated.

REFERENCES (U)

Booker, H. G. (1956), A theory of scattering by nonisotropic irregularities with application to radar reflections from the aurora, J. Atmosph. Terr. Phys., 8, 204-221. (Unclassified)

Bowhill, S. A. and E. E. Mendenhall (1972),"Transmission Experiments in Prairie Smoke I (U)", in Proceedings of Prairie Smoke I (U) (SECRET)

Briggs, G. H. and I. A. Parkin (1963), On the variation of radio star and satellite scintillations with zenith angle, J. Atmosph. Terr. Phys., 25, 339-365. (Unclassified)

Thome, G. D. (1972), "Geomagnetic perpendicularity calculations (U)" in Proceedings of Prairie Smoke I, RF Measurements Data Workshop, 25, 26, 27 Jan. 1972 (U), 61-70. (SECRET)

SECRET

Security Classification

DOCUMENT CONTROL DATA - R & D

(Security classification of title, body of abstract and indexing annotation must be entered when the overall report is classified)

1. ORIGINATING ACTIVITY (Corporate author)
Aeronomy Corporation
P. O. Box 2209, Station A
Champaign, Ill 61820

2a. REPORT SECURITY CLASSIFICATION
SECRET

2b.
XGDS 3

3. REPORT TITLE
Experiments and Models for Prairie Smoke (U)

4. DESCRIPTIVE NOTES (Type of report and inclusive dates)
Internal Technical Report - 1 Apr 72 to 1 Oct 72

5. AUTHOR(S) (First name, middle initial, last name)
S.A. Bowhill
E.E. Mendenhall

Classified by Proj Ivory Coral SCG Guide
EXEMPT FROM GENERAL DECLASSIFICATION SCHEDULE OF EXECUTIVE ORDER 11652
EXEMPTION CATEGORY # 3
DECLASSIFY ON 96

6. REPORT DATE
November 1972

7a. TOTAL NO. OF PAGES

7b. NO. OF REFS
31 Dec 1983

8a. CONTRACT OR GRANT NO.
F30602-72-C-0214

b. PROJECT NO.
ARPA 1423

c.

d.

9a. ORIGINATOR'S REPORT NUMBER(S)

9b. OTHER REPORT NO(S) (Any other numbers that may be assigned this report)
RADC-TR-73-94

10. DISTRIBUTION STATEMENT
None

11. SUPPLEMENTARY NOTES
Monitored by
Richard W. Carman (OCSE)
RADC, GAFB, NY 13441
AC 315 330-3144

12. SPONSORING MILITARY ACTIVITY
Advanced Research Projects Agency
1400 Wilson Blvd
Arlington, VA 22209

13. ABSTRACT

(S) This report describes satellite transmission experiments carried out in Prairie Smoke Ib and II to investigate the horizontal extent, altitude distribution, intensity and frequency dependence of field-aligned artificial spread F (ASF) irregularities. Using these data, a quantitative morphological model is described in which the irregularities are contained within a tilted cylinder, with axis parallel to the magnetic field direction, and a radius of 50 km, centered 30 km north of the heater at an altitude of 300 km. The fractional fluctuation of electron density was found to be about 0.1 percent at full power, and the correlation distance normal to the field was about 100 m. The irregularities were found to extend through the entire F region between 200 and 400 km altitude. The depth was found to vary inversely with frequency, in accordance with theory. Also presented in this report is a model for the small-scale structure, including an analytic technique to determine the thickness of the disturbed region from the change in echo return range with elevation of a monostatic radar; semi-thicknesses of about 25 km are found.

DD FORM 1 NOV 68 1473

SECRET

Security Classification

14 KEY WORDS	LINK A		LINK B		LINK C	
	ROLE	WT	ROLE	WT	ROLE	WT
Heated F layer						
Morphology of Artificial Spread F						